



**Politecnico
di Torino**

POLITECNICO DI TORINO

Master of Science in Energy and Nuclear Engineering

Master of Science Thesis

**Dynamic modelling of a
high-power electrolyser:
A study of green hydrogen
generation from an offshore wind
turbine and a wave energy
converter**

Supervisors

prof. Giuseppe GIORGI
prof. Giovanni BRACCO
prof. Markel Retes PEÑALBA

Candidato

Lorenzo GARIBALDI
student ID: 288056

ACADEMIC YEAR 2021-2022

This work is subject to the Creative Commons Licence CC BY-NC-ND

Summary

The energy transition is pushing towards a future powered by zero-emission energy systems, in which renewable energies can play a key role. Photovoltaic solar systems, wind power plants and wave energy converters are some of the protagonists involved in the energy revolution that humanity is experiencing. These systems are intermittent sources of energy due to the strict dependence on resource availability, such as solar radiation or wind. Electrolysers can help address the problem of intermittent energy production by making these systems more flexible and providing strength to electricity networks. Surplus renewable energy can be used to power electrolysers with the purpose of generating hydrogen, which can be stored as compressed gas, liquefied, or even absorbed/adsorbed, and then converted directly in electricity, by means of fuel cells. Moreover, hydrogen can be exploited in other sectors as well, including automotive, heavy-duty, chemical and hard to decarbonise industries, making its production even more interesting from a technological perspective. In this context, the aim of the thesis, developed in collaboration with Mondragon Unibertsitatea (Basque Country, Spain), is to implement a one-dimensional (1D) mathematical model of a proton exchange membrane (PEM) water electrolyser in the Simulink[®] environment and to test green hydrogen production from an offshore wind turbine and a wave energy converter. The model, composed of an electrochemical, thermal and mass transport submodels linked together, is able to predict the hydrogen production, heat flux generation, as well as water and energy consumption in dynamic conditions. In fact, in addition to model validation, a sensitivity analysis has been carried out, thus providing remarkable results on the electrolyser response to temperature and pressure gradients.

Contents

List of Tables	VII
List of Figures	VIII
1 Introduction	1
1.1 World energy outlook and climate change	2
1.2 Role of hydrogen and renewables	6
1.3 What is a PEM device	10
1.4 State of the art	13
2 Model description	16
2.1 Electrolyser model	16
2.1.1 Electrochemical submodel	18
2.1.1.1 Open-circuit voltage	18
2.1.1.2 Activation overvoltage	21
2.1.1.3 Ohmic overvoltage	22
2.1.1.4 Concentration overvoltage	23
2.1.2 Mass transport submodel	23
2.1.2.1 Anode molar flow rate analysis	24
2.1.2.2 Cathode molar flow rate analysis	25
2.1.2.3 Membrane molar flow rate analysis	26
2.1.3 Thermal submodel	31
2.1.3.1 Heat generation	32
2.1.3.2 Pump heat	34
2.1.3.3 Auxiliary cooling	34
2.1.3.4 Heat loss in the environment	38
2.1.3.5 Mass transport heat	38
2.2 Offshore renewable energy devices	39
2.2.1 Offshore wind turbines	39
2.2.2 Wave energy converters	42

3	Case study description	44
3.1	Electrolysis plant	44
3.2	Offshore wind turbine	46
3.3	Wave energy converter	48
4	Results	51
4.1	Model validation	51
4.2	Sensitivity analyses	54
4.2.1	Offshore wind turbine - Average power	55
4.2.1.1	Sensitivity analysis - Pressure	55
4.2.1.2	Sensitivity analysis - Temperature	58
4.2.2	Offshore wind turbine - Instantaneous power	63
4.2.2.1	Sensitivity analysis - Pressure	63
4.2.2.2	Sensitivity analysis - Temperature	67
4.2.3	Spar buoy - Instantaneous power	72
4.2.3.1	Sensitivity analysis - Pressure	72
4.2.3.2	Sensitivity analysis - Temperature	75
5	Conclusion	80
A	Simulink[®] figures	82
A.1	Simulink [®] model	83
A.2	Simulink [®] electrochemical submodel	84
A.3	Simulink [®] anode submodel	85
A.4	Simulink [®] cathode submodel	86
A.5	Simulink [®] membrane submodel	87
A.6	Simulink [®] heat exchanger submodel	88
A.7	Simulink [®] thermal submodel	89
	Bibliography	90

List of Tables

2.1	Saturated water vapour pressure coefficients [17]	20
2.2	Critical pressure, critical temperature and molar mass of hydrogen, oxygen and water [35]	30
2.3	MEA design parameters	31
2.4	Specific enthalpy (kJ/mol) empirical correlation coefficients [35] . .	39
3.1	Electrolysers' specifications	45
5.1	Qualitative summary of the results from the sensitivity analyses . .	80

List of Figures

1.1	Global median surface temperature rise over time in the WEO-2021 scenarios [1]	3
1.2	Global electricity consumption vs global primary energy consumption in 2019 [4]	6
1.3	Qualitative representation of the reactions running inside the electrolyser	11
1.4	CAD drawing and a photograph of a 50 cm ² single cell [9]	12
1.5	The Energiepark Mainz - 6 MW PEMWE plant [10]	14
2.1	Qualitative representation of the system	17
2.2	Molar flow exchanges - anode	24
2.3	Molar flow exchanges - cathode	25
2.4	Electro-osmotic drag coefficient dependency from membrane temperature	27
2.5	Qualitative representation of water concentration levels	28
2.6	Heat fluxes in the stack	32
2.7	Qualitative temperature trends along the heat exchanger	35
2.8	Qualitative representation of the heat exchanger	36
2.9	PID controller logic	36
2.10	Types of foundation for offshore wind turbines [37]	40
2.11	Schematic of spar, semisubmersible and tension leg platform floating wind turbines [38]	41
2.12	HyWind turbine installation by Saipem 7000 semi-submersible crane vessel [39]	41
2.13	Scheme showing working principles of MARMOK-A-5 [40]	42
2.14	MARMOK-A-5 in the Bay of Biscay, Spain [42]	43
3.1	HyLYZER [®] - 1000 by Hydrogenics - 5 MW nominal input power [48]	45
3.2	1.865 MW average power produced in 20 minutes	46
3.3	4.385 MW average power produced in 20 minutes	47
3.4	5.052 MW average power produced in 20 minutes	48
3.5	14.7 kW average power produced in 30 minutes	49
3.6	32.9 kW average power produced in 30 minutes	49
3.7	245.9 kW average power produced in 30 minutes	50

4.1	Polarization curve vs experimental evidence	52
4.2	PEM water electrolyser validation with PV real load. Continuous lines represent model simulation, dotted lines represent experimental measurements	53
4.3	PEM water electrolyser validation with PV real load @ Refrigerant: 50/50 water + glycol	54
4.4	Sensitivity analysis with respect to pressure - P_{av}^{wind}	56
4.5	Percentage weight of each term over the heat to be removed - P_{av}^{wind}	57
4.6	Sensitivity analysis with respect to outdoor temperature - P_{av}^{wind}	58
4.7	Heat and cooling flux temporal trend - P_{av}^{wind}	59
4.8	Sensitivity analysis with respect to PID temperature - P_{av}^{wind}	60
4.9	Focus on stacks temperature, cooling mass flow rate and cooling flux - P_{av}^{wind}	61
4.10	Sensitivity analysis with respect to refrigerant temperature - P_{av}^{wind}	62
4.11	Focus on stacks temperature, cooling mass flow rate and cooling flux - T_{refr}	62
4.12	Hydrogen production trends with respect to pressure - P_{inst}^{wind}	63
4.13	Energy consumption trends with respect to pressure - P_{inst}^{wind}	64
4.14	Temperature trends with respect to pressure - P_{inst}^{wind}	65
4.15	Heat flux trends with respect to pressure - P_{inst}^{wind}	65
4.16	Contribute of heat fluxes - P_{inst}^{wind}	66
4.17	Efficiency trends with respect to pressure P_{inst}^{wind}	66
4.18	Hydrogen production trends with respect to outdoor temperature - P_{inst}^{wind}	67
4.19	Energy consumption & heat flux trends with respect to outdoor temperature - P_{inst}^{wind}	68
4.20	Hydrogen production trends with respect to PID temperature - P_{inst}^{wind}	69
4.21	Energy consumption & heat flux trends with respect to PID temperature - P_{inst}^{wind}	70
4.22	Hydrogen production trends with respect to refrigerant temperature - P_{inst}^{wind}	71
4.23	Energy consumption & heat flux trends with respect to refrigerant temperature - P_{inst}^{wind}	71
4.24	Hydrogen production trends with respect to pressure - P_{inst}^{wave}	72
4.25	Energy consumption trends with respect to pressure - P_{inst}^{wave}	73
4.26	Temperature trends with respect to pressure - P_{inst}^{wave}	74
4.27	Contribute of heat fluxes - P_{inst}^{wave}	74
4.28	Efficiency trends with respect to pressure - P_{inst}^{wave}	75
4.29	Hydrogen production trends with respect to outdoor temperature - P_{inst}^{wave}	76
4.30	Energy consumption & heat flux trends with respect to outdoor temperature - P_{inst}^{wave}	76

4.31	Hydrogen production trends with respect to PID temperature - P_{inst}^{wave}	77
4.32	Energy consumption & heat flux trends with respect to PID temperature - P_{inst}^{wave}	78
4.33	Hydrogen production trends with respect to refrigerant temperature - P_{inst}^{wave}	79
4.34	Energy consumption & heat flux trends with respect to refrigerant temperature - P_{inst}^{wave}	79
A.1	Simulink [®] model	83
A.2	Simulink [®] electrochemical submodel	84
A.3	Simulink [®] anode submodel	85
A.4	Simulink [®] cathode submodel	86
A.5	Simulink [®] membrane submodel	87
A.6	Simulink [®] heat exchanger submodel	88
A.7	Simulink [®] thermal submodel	89

Chapter 1

Introduction

The present Thesis is developed in the following structure. **Chapter 1** is focused on the world energy outlook and the challenges to contrast climate change. The current resources employed to generate electricity, the share of energy from renewable systems and future trends are analysed in detail according to the International Energy Agency (IEA) and Intergovernmental Panel on Climate Change (IPCC) reports. The role of hydrogen in the nearly future, such as its contribute in the hard-to-abate sectors and to renewable energy systems facing low flexibility issues, is thoroughly reported. Then, information about PEM technology follow with a focus on functioning and state of the art, fundamental concepts for the understanding of successive sections.

The scientific literature is rich in examples and researches related to the modeling of PEM fuel cells, but still scarce as regards thorough PEM electrolyser models. Currently, open-source models, able to simulate the real operation of a PEM electrolyser, are not available, although several implementations have already been presented in different scientific papers. However, information is often fragmented and discordant, leaving the door open to doubts and misunderstandings. The aim of the present Thesis is to gather all the information and discoveries about the phenomena that characterise the functioning of PEM electrolysers and to create a reliable model, of fast execution and totally flexible. In addition, the research of a tool, able to model the entire chain of energy conversion directly from an offshore wind turbine model or a wave energy converters (WEC) model, to study the complete dynamics including the interactions between the components, was the main driver. The developed 1D PEM electrolyser model, described in **Chapter 2**, is able to simulate transient operating conditions thanks to the interface between the various submodels: electrochemical, mass transport and thermal. Then, a detailed description of the case study is presented in **Chapter 3**, reporting the strategy and the parameters needed to match the electrolyser with a power source of wind and marine origin. Finally, in **Chapter 4**, the model is validated with experimental evidence, showing the polarization curve and voltage/temperature dynamic trends

with respect to real measurements. In addition, the system, described in the former chapter, is tested under pressure and temperature gradients varying in a wide range, powered by wind turbine and wave energy converter simulations. In the end, some concluding remarks and possible future model developments are reported in **Chapter 5**.

1.1 World energy outlook and climate change

Global warming is the result of anthropogenic actions, particularly, the energy sector is responsible for almost three quarters of emissions into the atmosphere, that have pushed the global average temperature over $1.1\text{ }^{\circ}\text{C}$ since pre-industrial age [1]. The higher the temperature, the greater the risk of severe natural events, such as floods, hurricanes, excessive droughts or extreme heat. The increase of this phenomena (frequency) is already evident, as well as the rise of their intensity. Besides human losses, extreme events could destabilise several sectors, starting from the energy one, putting in an extremely fragile condition several world's areas. In addition, the recurrence of extreme natural events accelerate the already started loss of biodiversity in terrestrial, freshwater, marine and coastal ecosystems, which affect human food security and long-term public health as well. Limiting the increase of temperature to $1.5\text{ }^{\circ}\text{C}$ from the pre-industrial age would substantially reduce expected losses and damage in the ecosystems [2].

However, imposing by force a reduction in energy consumption is not possible, both considering developed countries and developing ones, which will demand, in the following years, more and more energy to build their infrastructures and develop their own country's economy. A shift to a new system is necessary, able to satisfy the human needs (e.g. eradicate energy poverty) and the aspirations of everyone, considering a global population that is expected to grow by 2 billion in 2050. Currently, the employed energy systems are not ready to embrace these needs without pushing even further the global average temperature, but the time to curb global warming and avoid an escalation is coming to an end: a revolution towards low-emission systems is long overdue. The commitment of companies, associations, groups or even individuals can help, but only the policies of nations can shake the system and set the tracks for a revolution. For this reason, it is necessary that everyone begins to form their own sensitivity and awareness towards environmental issues.

The World Energy Outlook (WEO) 2021, published by the International Energy Agency (IEA) [1], identify some key measures of fundamental relevance that can help to close the gap between the current intentions declared by individual countries and the objective to reach net zero emission target in 2050. Three are the identified main scenarios: the Announced Pledges Scenario (**APS**), Stated Policies Scenario

(**STEPS**) and the Net Zero Emissions (**NZE**) Scenario. Each of them produces different results with respect to the rise of the global median surface temperature (Figure 1.1).

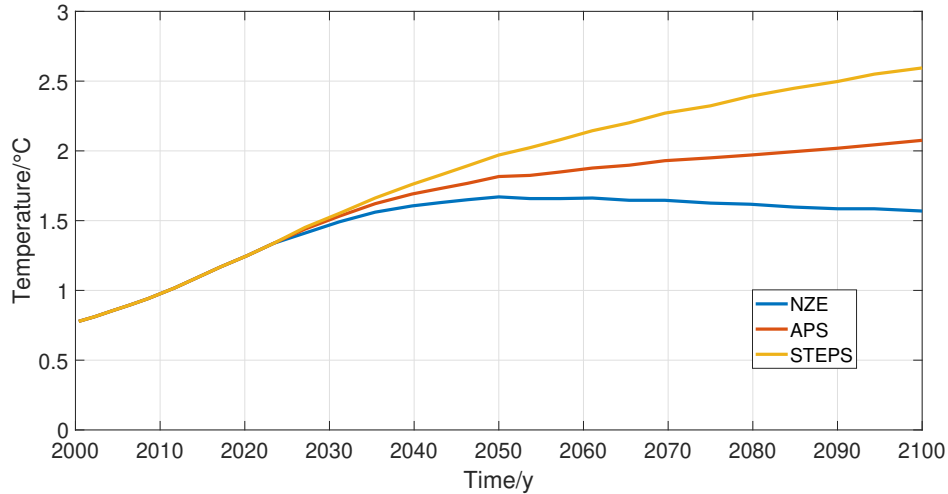


Figure 1.1. Global median surface temperature rise over time in the WEO-2021 scenarios [1]

The first one represents the announced contributions to reduce the emission and introduce structural changes to reach the climate goals. More than 50 countries have declared their intentions to respect their pledges, including the European Union. In the APS scenario, the increase of the installed power generation system is mainly composed of low-emission systems, particularly, it is declared an annual addition of 500 GW of wind and solar photovoltaic (PV) by 2030. This action will lead to a fall of 40% of energy related CO₂ emissions over the period to 2050. This effort will not stop the rise of the global average temperature, that will arrive to an increase of 2.1 °C by 2100 (Figure 1.1), losing the zero emissions target and leading to a temperature trend still not stabilized.

The STEPS scenario is composed of all the real actions currently carried out by countries, as the initiatives of specific policies. It is obviously the worst scenario that involves an increase of 2.6 °C above pre-industrial age by 2100. It sees a continuous increase of emissions from industry, like the one of production of cement and steel, or heavy duty transport. In the STEPS, almost all of the net growth in energy demand in 2050 is met by low emission sources, leaving, by the way, annual emissions approximately at current levels.

The last scenario is the Net Zero Emissions, that, as the name suggests, aims to reach zero emissions into the atmosphere by 2050, therefore most of the energy

sector powered by low-emission systems.

Four are the identified main pillars for a zero greenhouse gases (GHG) emission future and 40% of the required actions are already cost effective.

1. A massive push to clean electrification which includes the deployment of solar PV and wind installations, as well as other forms of low-emission systems, among the others, the nuclear power where feasible. In fact the nuclear energy, together with wind and solar PV, is so far one of the safest form of energy, with the pro of having a really high energy density, followed by low CO₂ emissions. The implementation of renewable energy systems need to be followed by huge investments in the electricity infrastructure to accommodate the intermittent energy production and to accompany the development of other technologies, such as transport (electric mobility) or heating. Energy storage systems need to be implemented to accommodate the energy production from renewable resources, making the electricity infrastructure sufficiently flexible.
2. A relentless focus on energy efficiency, that is of fundamental importance in tackling climate change. In fact, the main objectives to chase are being able to produce the same amount of energy, or even increase it to satisfy the energy demand (that is destined to increase), avoiding waste and losses.
3. Cut methane emission from fossil fuel operations. Methane (CH₄) is principally emitted during the production and transport of coal, oil and natural gas, although the emissions come also from the processing and storage. A large amount of methane is produced also by livestock and agricultural sectors, as well as land use and by the decay of organic waste in municipal solid waste landfills.

The global warming potential (GWP) expresses the contribution of a gas to the greenhouse effect in relation to the impacts caused by CO₂ (GWP = 1). The GWP of methane, measured over a 20-year period, is around 85 times the one of carbon dioxide. Considering an even longer time scale of 100-year, the GWP would still be 28-34 times higher [3]. For this reason, the methane emissions must be controlled and reduced. As an example, it has been estimated that, during 2020, the gas flaring¹ caused the emission of 500 Mt of CO₂, equivalent to more than the annual emission of carbon dioxide from all cars in the European Union [1].

4. All the technologies needed to reach the goals set by 2030 are already available, but aiming to avoid going further the 1.5 °C increase, the nations needs to

¹Gas flaring is a practice that consists in burning the natural gas in excess, extracted together with oil, through flares posed at the top of oil towers.

invest more in all those technologies that are currently at prototype or still under development stage (R&D). Hydrogen and low-carbon fuels measures fall short in the current pledges, as well as the carbon capture utilisation and storage (CCUS) systems.

Currently, looking at the energy mix and particularly at the consumption by source in 2021, the majority of the produced energy comes from fossil fuels, i.e. oil (51,170 TWh), coal (44,473 TWh) and natural gas (40,375 TWh) respectively. They account for more than 80% of global primary energy consumption² (176,431 TWh), followed by hydropower, nuclear, wind, solar energy, modern biofuels and other renewables [4]. Of interest is their projections according to the three scenarios described above, knowing that, even in the NZE scenario, less than 50% of total final energy consumption³ accounts for electricity, so liquid, gaseous and solid fuels will still be part of the energy mix in 2050.

In the WEO 2021, the **oil** demand experiences a decline in all the scenarios. Analyzing the STEPS, a slightly decline by 2050 is observable, while in the APS, oil demand decreases sharply until 77 mb/d⁴, that is still a great amount if compared with the NZE scenario in which oil demand falls to 72 mb/d in 2030 and to 24 mb/d by 2050.

Regarding the **natural gas**, the demand increases in all scenarios over the next 5 years. In the STEPS, an increase of 15% and 30% with respect to 2020 is predicted in 2030 and 2050, respectively. Different is the APS scenario, which experiences a small decrease of 1.6% by 2050, in great contrast with the 55% by 2050 of NZE. It is important to note that in the last scenario, by 2050, more than 50% of consumed natural gas is used to produce low-carbon hydrogen.

Fortunately, as in the case of oil, also the **coal** demand sees a reduction in all scenarios. The STEPS and APS are quite similar, even if the APS experiences a slightly greater reduction, due to the fact that coal is principally consumed by those countries that do not intend to reduce it, or at least not immediately. In fact, the coal global demand by 2050, in the APS, is around half the one in 2020. The phase-out of coal is particularly challenging in those developing countries, like China, in which the growth of emerging markets requires high energy density at low cost. In fact, China results to consume the 60% of the global unabated coal in

²Primary energy consumption refers to direct use of energy at its crude stage, therefore it includes, beyond the energy consumption at the final user (energy sector or end user), the produced losses during the processes and distribution.

³Total final energy consumption accounts for the sum of all consumption from end user sectors.

⁴Thousand barrels per day.

the electricity sector by 2030 in the APS, followed by India (15%) and South-East Asia (10%). Things are completely different in the NZE scenario that involves a 55% of reduction by 2030 and a 90% by 2050. Being the coal the most polluting fossil fuel, its consumption must be reduced as soon as possible.

In the next section, the role of hydrogen in the energy transition and the renewable future scenarios will be discussed.

1.2 Role of hydrogen and renewables

In 2019, approximately the 11% of global primary energy came from renewable technologies, 15.7% considering the nuclear power component. By analysing only the electricity contribution, therefore leaving aside from the global primary energy mix the transport and heating, more than one third comes from low-carbon sources (26.3% from renewables, 10.4% from nuclear power plants) [4].

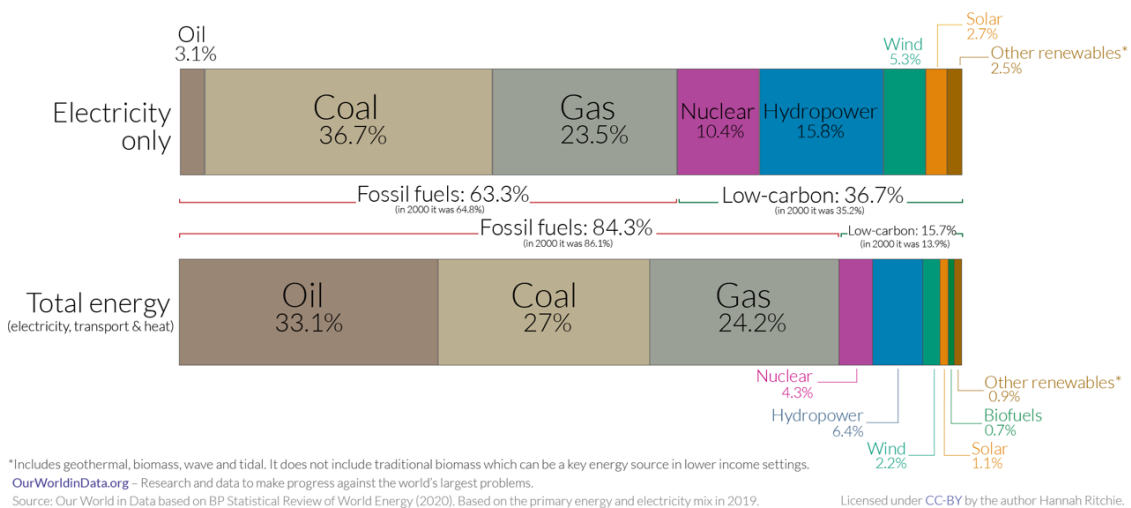


Figure 1.2. Global electricity consumption vs global primary energy consumption in 2019 [4]

However, as expressed in the previous section, the clean energy component in the energy mix has to increase to remain in the already mentioned 1.5 °C of global average temperature increase. All the previously cited scenarios (APS, STEPS and NZE) include an increase of renewable power, that are considered as the future foundation of electrical systems around the world [1].

Solar PV and wind energy production are, being the cheapest source of electricity in most market, destined to grow, in particular their share of electricity generation

is expected to rise, according to the announced pledges, from a starting point of 10% in 2020 to 30% in 2030. Other forms of renewable also show an increase of their share in the electricity mix, like hydropower, geothermal and bioenergy, while concentrating solar power and marine power gain more stability. In the APS scenario, the nuclear power experiences an increase of 10% in its power capacity in 25 countries by the end of 2030, even more in the NZE where the new installed capacity, together with the life extension of existing reactors, increase by 25% by 2030.

Regarding the goal to close the gap between the APS and STEPS scenario, the renewables play a fundamental role. The rate of energy production from renewables increases from 8%/year in the APS to reach 12%/year in the NZE. As an example, during 2020 the new installed capacity was 248 GW, a record level, but the one expected in the APS in 2030 is almost double (470 GW), and in the NZE is even more, exceeding 1,000 GW. This increase should be supported by the markets and IEA estimates that the 60% of solar PV and wind new installed capacity in the NZE taking as a reference the APS (in 2030) would be cost-effective, thanks to the low-cost of technology and financing markets. Policy-makers play a key role in creating environments and opportunities that foster the energy transition.

The recent outbreak of the Russia-Ukraine war has added another layer of complexity to the already fragile scenario that humanity is living, i.e. the restart of economic activity after COVID-19 pandemic, surging inflation, etc. Europe has been destabilized and many countries, like Italy, are facing the energy security topic, being strongly dependent by Russian natural gas. Future trends are still pretty faded, but there are reasons to believe that this could push even faster towards the deployment of renewable energy technologies, and on the accelerated phase-out of fossil fuels [5, 6]. On the other hand, the possibility of experiencing an increase of energy prices in order to cope with investments could divert the path, thus slowing down the energy transition. In any case, in order to reach the goal of curbing climate change and reversing the increasing trend of global average temperature, the future needs to be powered, especially the electricity sector, by renewable and nuclear resources. In this framework, hydrogen could play a fundamental role.

Hydrogen can help to face the problem of intermittent power production of renewable energy systems, more specifically by making them more flexible and smoothing the power generation curve. In fact, renewable resources are aleatory, therefore the energy production (frequency and intensity) it is not predictable. They depend strictly on weather conditions, especially solar and wind, which is why the implementation in the electricity grid of a nation is not trivial. In fact, the solar PV systems often show peaks of production around noon, to drop swirling into the evening hours, to be zero at night. The wind, in its own way, can also blow at night, but it is still aleatory and very geographically distributed. Solutions need to be

investigated to store energy produced in surplus to supply it when most requested. Hydrogen, in this perspective, can provide a support, in fact, it is properly an energy carrier, or, in other terms, a link between two forms of energy (which can also coincide, as in the case of the *power-to-power* applications). At production peaks, through the use of electrolyzers, it is possible to separate the water molecule into its components: oxygen and hydrogen. Oxygen can be exploited in the chemical industry, as well as hydrogen (e.g. ammonia production, currently produced from fossil fuels, synthetic liquids or gas).

Once produced, hydrogen can be used to generate energy through the well-known fuel cells, creating in this way a system where energy can be stored (if in surplus) and then released when most needed, thus making renewable devices more flexible and reliable. Obviously, in terms of energy, there are losses in the conversion from one form to another (electricity \rightarrow chemical energy \rightarrow electricity again), but it is something not avoidable that can only be reduced or minimised. Considering that offshore wind capacity will be increased in the next years due to its higher power productivity compared to onshore wind systems and that the more interesting offshore areas are far from shore, from where transporting energy via electrical cables is unfeasible, hydrogen could become an interesting alternative to enable the extraction of those energy sources. Then, considering the possibility of exploiting hydrogen also in other sectors, its role becomes even more interesting. In fact, fuel cells can be installed on heavy duty vehicles, thus making them powered by hydrogen, with water as the waste product. Obviously it is important that hydrogen is of renewable origin (green hydrogen) or nuclear (purple hydrogen), otherwise it would lose importance in a decarbonisation perspective.

Nowadays, roughly 85% of the hydrogen is produced from methane (gray hydrogen), in particular through the natural gas reforming process. It would be different if the CO₂ produced by the process was captured through CCUS systems, thus generating the so called blue hydrogen. Other sectors that could benefit from hydrogen are heavy industry, such as steel or cement, defined as "hard-to-abate" (which processes need high temperatures), but also domestic heating.

Observing the NZE scenario in 2030, around half of low-carbon hydrogen production comes from water electrolysis and half from coal and natural gas equipped with CCUS [1]. Hydrogen supply rise to 17 EJ in 2030 (11 EJ was the one produced in 2020), with a third employed in the power sector, 25% in industry, 15% converted into other fuels and the rest used in the transport and building sector. This will involve around 15 million fuel cell vehicles by 2030, in particular heavy trucks. By 2050 the production rises till 60 EJ, with around 25% converted into hydrogen based fuels and another quarter employed for transport. This is the only scenario that experience an increase in the production of synthetic methane to be employed in those regions in which it is not cost effective to shift to electricity, biomethane,

or hydrogen. The amount of syn-CH₄ produced in 2050 is 3% or methane supplied in the 2020, around 4 EJ.

In the STEPS scenario, the hydrogen produced from low-carbon sources in 2050 is 15% of the 2020 total demand in industrial feedstock and oil refining, with the 80% produced from electrolysis.

Lastly, in the APS, total low-carbon hydrogen production rises to 20 EJ in 2050 (a little more of the production in 2030 of NZE), playing a major role in the transport, as substitute of oil, and power sector, displacing coal and methane.

Analysing more specifically the European Union framework, several indicators show the closeness to a tipping point. Specifically, in *A hydrogen strategy for a climate-neutral Europe* document, published by the European Commission [7] in 2020, the aim of developing clean hydrogen production systems at large scale is well declared, thus to achieve the climate ambition to reduce GHG emission by a minimum of 50% compared with 1990 levels by 2030, in accordance with the objectives of the European Green Deal [8]. The investments in renewable hydrogen could bring to a cumulative of 180-470 billion of euros by 2050 and 3-18 billion for low-carbon fossil-based hydrogen, with an employment of 1 million people [7]. A road map, structured in the following way, is reported in the document:

1. 2020 - 2024

Install at least 6 GW of electrolyzers (to be powered by renewable energy) in the European Union reaching 1 millions tonnes of renewable hydrogen produced, with the aim to decarbonise the existing hydrogen production chain supplied by almost fossil fuels. Currently the estimated costs for renewable hydrogen are in the range of 2.5 - 5.5 EUR/kg, higher compared to fossil based (1.5 EUR/kg) or low-carbon like fossil based equipped with CCS (2 EUR/kg), but they are going down quickly and they are expected to halve in 2030 due to economy of scale [7]. Therefore, in this phase, electrolyzers need to be scaled up (up to 100 MW) and the European Clean Hydrogen Alliance will support the deployment of these technologies. Next Generation EU (a temporary recovery instrument employed to repair, in part, the economic and social damage brought by the COVID-19 pandemic), including the Strategic European investment Window of the InvestEU programme and the ETS Innovation Fund, will enhance the funding support.

2. 2025 - 2030

Install at least 40 GW in Europe, and 40 GW in Europe's neighbourhood with export to the EU, of electrolyzers (to be powered by renewable energy) by 2030 with the objective to produce 10 million tonnes of renewable hydrogen. In this phase, hydrogen starts to play a key role in the electricity system by

supporting renewable energy production. Hydrogen is expected to become more cost-competitive and the necessity to build infrastructure (pipelines and large storages) becomes a critical point. In fact, hydrogen must be transported from the areas of production to where more needed, considering also other Members States.

3. 2030 - 2050

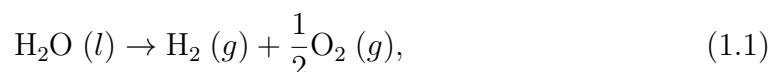
As in the IEA projections, also in this case the large increase of renewable energy must be matched with hydrogen production, that is expected to consume a quarter of total renewable electricity by 2050. In this phase renewable hydrogen technologies should reach maturity and be ready to meet all the hard-to-abate sectors.

In the next section, a study of the operation of PEM electrolyzers is presented.

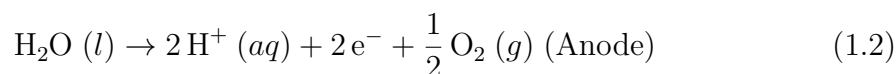
1.3 What is a PEM device

In the previous sections it has been discussed the role of hydrogen in the near future, and in particular the term "electrolysis" and "electrolyser" has been mentioned several times, pointing out as water can be split into its components, namely oxygen and hydrogen, by the use of electricity. In this section, an overview of what an electrolyser is, of which parts it is made up and how it works is reported.

An electrolyser is a device capable of carrying out the hydrolysis reaction, or water splitting reaction, namely:



which can be split in two, relative to anode and cathode, i.e.



and



In fact, the electrolyser can be divided into different parts: the anode, the cathode and the electrolyte. Both the anode and the cathode are electrodes, with the difference that the first one drives an **oxidation** reaction, i.e. the molecule in contact with it can release a certain number of electrons and cations (ions with positive sign) that depends by the type of reaction, while the cathode drives a **reduction** reaction, i.e. a molecule in contact with it can absorb electrons and release anions (ions of negative sign).

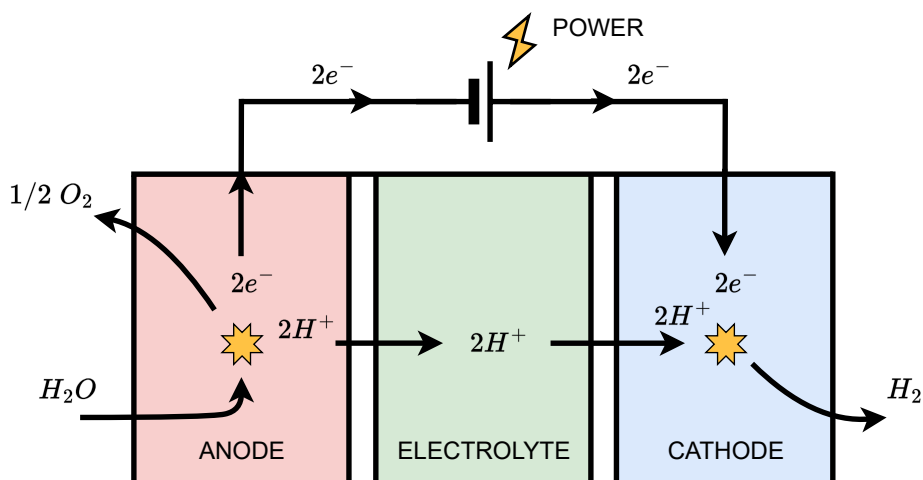


Figure 1.3. Qualitative representation of the reactions running inside the electrolyser

In this case, water, in contact with the anode, releases two protons H^+ (cations) and two electrons e^- , producing one oxygen molecule in the process (Equation 1.2). The cations cross the electrolyte reaching the electrons at the cathode, that have been pushed by a voltage applied to the edges of the electrodes, recombining with the H^+ protons and thus forming two hydrogen atoms (Equation 1.3). The electrolyte is a layer able to separate the electrons from the ions so that they do not immediately recombine after have been split. Obviously the process in Equation 1.1 does not happen spontaneously, but requires the application of a voltage, and therefore of energy, to move electrons from one electrode to another.

In principle, it would be possible also to inject water into the cathode, which would be split into O^{2-} , two electrons e^- and two hydrogen atoms; then the anions would pass to the anode through the electrolyte. Once at the anode, an oxidation reaction would take place and the electrons released, under the action of a voltage, would return to the cathode to resume the operation of water reduction. In the end, hydrogen and oxygen would still be the products, but the reason why it will be considered the first case explained (Figure 1.3), that sees H^+ passing across the electrolyte and not O^{2-} , it is because the device here analysed is a proton exchange membrane (or polymeric exchange membrane, i.e. **PEM**) water electrolyser (PEMWE). In fact, what characterises the device is precisely the electrolyte that can be composed of a liquid or a solid (as in our case). The advantage of using a membrane, and so a solid material, lies in the performance of the device itself. In our specific case the most commonly used material is Nafion, that is a polymer (Teflon, i.e perfluoroether chains) with sulfonic acid groups randomly distributed, attached to its backbones. The HSO_3 sulphur ionic side has a weak bond O-H,

so a good ionic H^+ mobility, fundamental property for a PEM. One of the cons of these materials is that they are good conductors only if well hydrated, because the mechanism by which the H^+ moves is the **hopping mechanism** (or Grotthuss mechanism): to move it is not the single ion but a molecule composed by a cation linked with water molecules, such as H_3O^+ , $H_5O_2^+$, $H_7O_3^+$, etc. For this reason, in a PEM electrolyser the management of water is crucial, as well as the temperature one, in fact, it cannot go over $100\text{ }^\circ\text{C}$ without making water boiling inside the device. For this reason, the electrodes, generally composed of carbon-based material (graphite), needs to be coated with a layer of catalyst (Pt-Ir or Pt-IrO₂), in order to accelerate the reaction kinetics, not favored by low temperatures. Graphite is used as a constituent material because the electrodes need to be porous, so that molecules, such as water, can spread to the catalyst (reaction site), but also good electrical and ionic conductors. Therefore, to have a good electrode, there must be a good distribution of these three characteristics identified as the **three phase boundary** (TPB). The electrodes, plus the membrane, constitute the **membrane electrode assembly** (MEA).

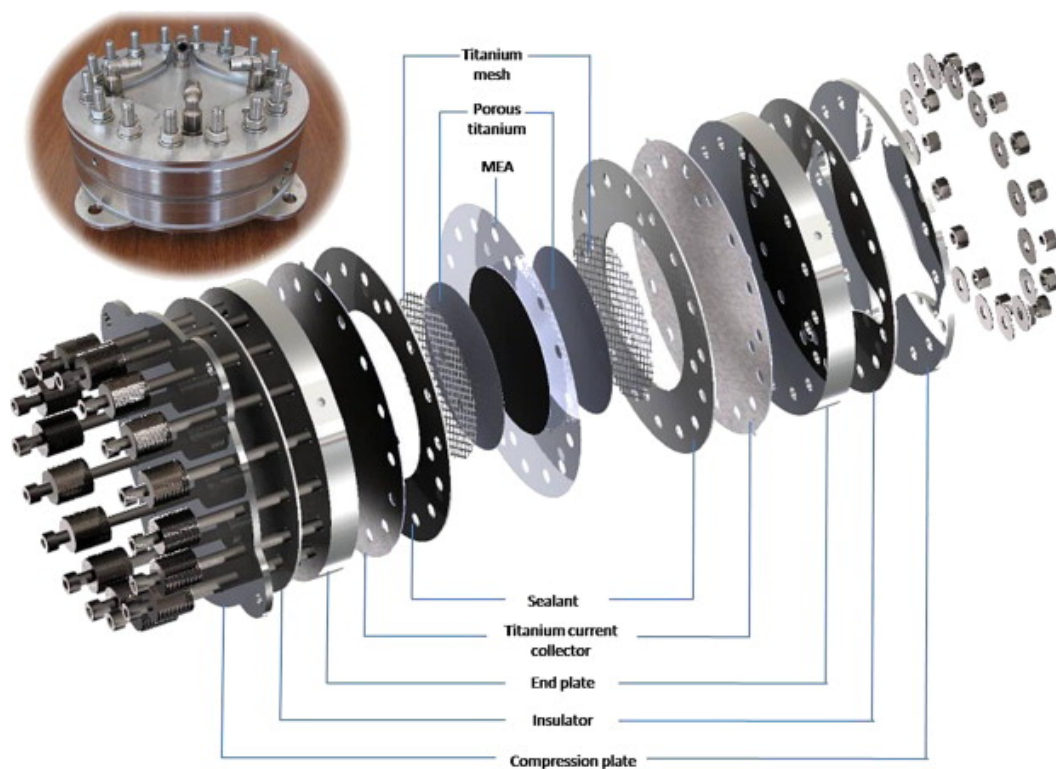


Figure 1.4. CAD drawing and a photograph of a 50 cm^2 single cell [9]

What has been described until now is a single PEM cell, however, in an electrolyser, multiple cells are electrically connected in series to increase the production

of hydrogen. Each cell is connected to the next one by a metal plate, called interconnector that, as the name suggests, connects the cathode of one cell to the anode of the next. The interconnector needs to be a good electronic conductor material, dense enough to prevent the reaction products (oxygen and hydrogen) from escaping or recombining with each other (thus leading to an explosion) and easy to work; generally titanium is employed. The role of the interconnector is to provide, in addition to a good electronic conduction, also channels where reaction products can exit, as well as others in which coolant can flow. The presence of the last is of great importance in the thermal management of the device. The channel shaping requires thorough design to provide the least pressure loss and maximum homogeneity. Liquid and gas flows inside the cell can be modeled through computational fluid dynamics (CFD) techniques.

Clearly, PEM electrolyzers are not the only existing electrolyzers on the market, but there are many others, such as alkaline (AEC), or direct methanol (DMEC) ones. There are also electrolyzers able to work at higher temperatures, between 600 and 900 °C such as solid oxides (SOEC) or molten carbonates (MCEC) ones, which, however, although more efficient, are not the best option if coupled with renewable energy systems. In fact, among the great pros of PEM electrolyzers there is a quick start-up that is fundamental considering the high variability of renewable power.

1.4 State of the art

In the last years it has been experienced a scale-up of PEM technology, moving from kW to MW plants (Figure 1.5), already available on the market. In fact, small systems (< 10 kW) are currently employed in sectors like meteorology, hydrogen welding, gas chromatography or in small laboratories, but also bigger application can be found in the metallurgical field, pharmaceutical and chemical industry, as well as in the glass and electronic one. Hydrogen has experienced a re-birth due to the necessity to abate all those heavy pollutant sectors and to remain in the already mentioned 1.5 °C of global average temperature increase, becoming particularly interesting in the renewable and nuclear energy applications. For this reason, there is a general effort to increase the productivity of these systems, moving towards the creation of tens-MW plants able to produce huge amounts of hydrogen.

Several companies are currently producing MW-PEM electrolyzer like ITM Power, Siemens, Hydrogenics, ArevaH2Gen, Giner and several others. To date, the record for the most powerful electrolyzer ever built is held by Air Liquide, that is able, with its 20 MW PEMWE equipped with Cummins technology (acquired in the 2019 by Hydrogenics), to produce 8.2 tonnes of hydrogen per day from renewable energy systems (hydropower dams), avoiding the emission of around 27,000 tonnes of CO₂ per year (equivalent to 10,000 car emissions per year) [11].



Figure 1.5. The Energiewerk Mainz - 6 MW PEMWE plant [10]

The research is focusing on two aspects: increase the productivity and the operational pressure. Even if the increase of pressure could bring to a reduction of productivity, it has been demonstrated to be effective as regards energy consumption in the hydrogen compression, as well as in reducing the vapour content in hydrogen. In fact, one of the most energy demanding processes is the first pressurisation up to 30 - 50 bar. There are many researchers that are trying to go above the roof of 200 - 300 bar, so that hydrogen can be directly stored for, e.g., mobility applications [12]; however, there exist certain safety limitations that are making it challenging. Being the oxygen produced often released into the atmosphere as a waste product, solutions like the pressurisation of only one electrode are being studied.

In order to increase the productivity, besides building larger systems, so with more active areas and more cells connected in series, a trend is to operate at higher temperature going further the 100 °C, up to 120 - 130 °C, with the adoption of new electrolytic membranes (polybenzimidazole-based membranes, in particular).

In future applications, artificial intelligence methods, neural networks, as well genetic optimization systems will be developed to create more and more efficient designs. In particular, the common trend is to create networks in which the sub-systems can communicate and self-regulate to follow the power curve and optimize the hydrogen production.

To decrease the CapEx (Capital Expenditure) of PEM electrolyzers, the employment of cheaper materials is a goal to be pursued, regarding especially the catalysts coating on the electrodes. In order to reduce the costs related to the coatings, also called PGM (Platinum Group Materials), the PGMs loading can be reduced or

directly substituted with other materials. In fact, several non-PGM materials are being studied, like MoS_x species, porphyrins on graphite paste and phthalocyanine that have shown good results in the hydrogen evolution reaction (HER), as well as Co, Ni and Fe clathrochelates [12]. However, credible solutions adopting non-PGMs are currently not available.

Chapter 2

Model description

In the model description, several aspects will be analysed, starting from the electrolyser model (Section 2.1), divided in the electrochemical, mass transport and thermal submodels, moving then to the characterisation of the offshore renewable energy devices (Section 2.2). The electrolyser model will be described in detail, explaining the physics associated to the main phenomena and reporting all the meaningful empirical correlations, together with all the parameters that characterise the system. As the main concern of the Thesis is the PEM electrolyser, the modelling of the offshore renewable energy devices will be simply mentioned.

2.1 Electrolyser model

The system implemented in the Matlab/Simulink[®] environment is composed by several sub-systems that interact with one other sharing information. Among the most important: the anode, the membrane, the cathode, the thermal and the electrochemical submodel.

Physics is based on a plant composed, firstly, of a stack, which aims to produce hydrogen and oxygen through the water splitting reaction (Equation 1.1), consuming simultaneously energy from renewable sources. A certain amount of water participates in the reaction, while the remaining is transferred from anode to cathode due to two physical phenomena: **electro-osmotic drag** and **concentration diffusion**. The amount of water exiting the cathode is recirculated through a loop, in which water is continuously injected in order to compensate the consumption (see Figure 2.1). The produced hydrogen and oxygen are stored in tanks, after having passed through gas separators, in which vapour, if present, condenses and turns back to the loop. Water recirculation is ensured by a pump which participates, due to friction losses, to the amount of heat supplied to water. A second loop is present, whose aim is to cool the device through a heat exchanger.

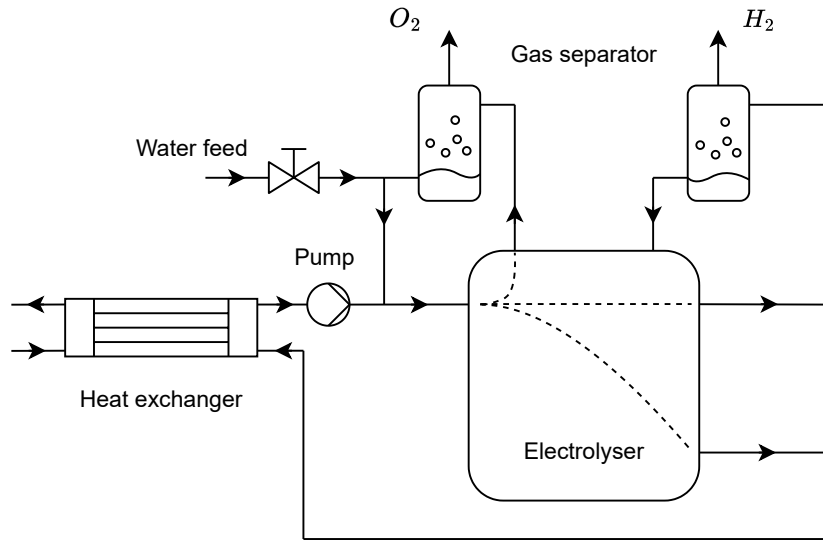


Figure 2.1. Qualitative representation of the system

The amount of refrigerant flowing in the circuit is determined by a Proportional–Integral–Derivative (PID) controller, that, based on the temperature measurement in the first loop, regulates the opening of an electro-valve at the inlet of the heat exchanger (second loop side). Each section of the system will be further discussed later in the document.

Several assumptions were made, both depending on the gas physics and technical aspects regarding the system itself. Though a part of these will be discussed in the relative sections, some of them can already be mentioned.

Hypotheses

1. One-dimensional model (1D);
2. Steady-state and semi-empirical electrochemical and mass transport submodel coupled with thermal and power load dynamic submodel;
3. H_2 , O_2 , water vapour assumed to be as ideal gasses;
4. Negligible membrane diffusivity and solubility in water of H_2 and O_2 ;
5. Negligible membrane water transport due to pressure difference between anode and cathode;
6. Uniform temperatures across the stack, implying negligible temperature gradients within the control volume;

7. The membrane is considered to be completely saturated with water, therefore its conductivity is a function of temperature only;
8. Current density supplied up to 3 A/cm² to neglect concentration overvoltage.

2.1.1 Electrochemical submodel

The theory behind the electrochemical phenomenon is well known. The voltage of an electrolyser is influenced by several factors, called overvoltages, which are, in all respects, losses. The electrolyser voltage can be evaluated as the sum of the open-circuit voltage E and three overvoltages, namely the activation η_{act} , ohmic η_{ohm} and concentration η_{conc} overvoltage [19]:

$$V_{cell} = E + \sum_{k=1}^3 \eta_k = E + \eta_{act} + \eta_{ohm} + \eta_{conc}. \quad (2.1)$$

Considering N cells connected in series, it follows that

$$V_{stack} = N V_{cell}. \quad (2.2)$$

However, it is necessary to introduce some basic concepts to explain in more detail the physics behind these definitions.

2.1.1.1 Open-circuit voltage

The theoretical voltage, also known as open-circuit voltage, can be calculated starting from the **Faraday's law** (Equation 2.3) and the laws of thermodynamics:

$$\dot{N} = \frac{N I}{z_i F}, \quad (2.3)$$

where \dot{N} is the molar flow, measured in mol/s, of a chemical species i participating to the reaction, I the current measured in A, z_i the **charge number** or number of electrons delivered in the oxidation or recombined in the reduction reaction referred to the chemical species i and F the Faraday's constant equal to 96485 C/mol.

Considering the case of a cell driving a chemical reaction with $\Delta\bar{g}_{reaction} > 0$ (**endergonic reaction**) in J/mol, therefore with $W_{el} < 0$ (power consumption in W) and $\Phi > 0$ (heat consumption in W), the first law of thermodynamics becomes

$$|\Phi| + |W_{el}| = \left(\sum_{i=1}^N \dot{N}_i \bar{h}_i \right)_{products} - \left(\sum_{i=1}^N \dot{N}_i \bar{h}_i \right)_{reactants}. \quad (2.4)$$

while the second law can be written as

$$\frac{|\Phi|}{T} = \left(\sum_{i=1}^N \dot{N}_i \bar{s}_i \right)_{products} - \left(\sum_{i=1}^N \dot{N}_i \bar{s}_i \right)_{reactants}. \quad (2.5)$$

By normalizing with respect to the molar flow of the fuel \dot{N}_F , it is possible to obtain the following definitions:

$$\frac{\Phi}{\dot{N}_F} = \bar{q} \quad \frac{W_{el}}{\dot{N}_F} = \bar{l} \quad \frac{\dot{N}_i}{\dot{N}_F} = \nu_i. \quad (2.6)$$

Given the above definitions, the first and second law can be rewritten as:

$$|\bar{q}| + |\bar{l}| = \left(\sum_{i=1}^N \nu_i \bar{h}_i \right)_{products} - \left(\sum_{i=1}^N \nu_i \bar{h}_i \right)_{reactants} = \Delta \bar{h}_{reaction} \quad (2.7)$$

and

$$\frac{|\bar{q}|}{T} = \left(\sum_{i=1}^N \nu_i \bar{s}_i \right)_{products} - \left(\sum_{i=1}^N \nu_i \bar{s}_i \right)_{reactants} = \Delta \bar{s}_{reaction}, \quad (2.8)$$

from which:

$$|\bar{l}| = \Delta \bar{h}_{reaction} - T \Delta \bar{s}_{reaction} = \Delta \bar{g}_{reaction}. \quad (2.9)$$

At the same time, by applying the Faraday's law (Equation 2.3) to $|\bar{l}|$ definition

$$|\bar{l}| = \left| \frac{W_{el}}{\dot{N}_F} \right| = \frac{E I}{z_F F} = z_F F E \quad (2.10)$$

and combining it with Equation 2.9, the **Nernst's equation** can be derived:

$$E = \frac{\Delta \bar{g}_{reaction}}{z_F F}. \quad (2.11)$$

The Nernst voltage E (also called theoretical or open-circuit voltage) is function only of $\Delta \bar{g}_{reaction}$, as it is evident from Equation 2.11. As a consequence, it depends on:

1. type of reaction (water splitting in this case);
2. thermodynamics: $T, p_i \rightarrow \bar{g}_i(T, p_i)$.

The dependence on thermodynamics can be expressed according to the following form, in which the specific Gibbs free energy of reaction $\Delta \bar{g}_{reaction}$ depends on temperature and a reference pressure, i.e. $p_0 = 1.01325$ bar:

$$E = \frac{\Delta \bar{g}_{reaction}(T, p_0)}{z_F F} - \frac{RT}{z_F F} \ln \left[\frac{\prod_{i=1}^{n^{of R}} a_i^{\nu_i}}{\prod_{i=1}^{n^{of P}} a_i^{\nu_i}} \right] \quad (2.12)$$

where R is the gas constant, a_i the activity and ν_i stands for the stoichiometric coefficient of the chemical species.

Now, by assuming that ideal and water vapour saturated gases are formed, wet gases are present in the channels of the electrolyser, therefore hydrogen and oxygen saturated [13, 14, 15, 16]. It follows that, the hydrogen, oxygen and water vapour activity, thanks to the hypothesis of **ideal gas**, can be written as:

$$a_i = p_i/p_0 \quad (2.13)$$

with p_i the partial pressure measured in bar and p_0 the reference pressure of 1.01325 bar.

The water vapour pressure is temperature dependent and can be expressed through the following empirical correlation [17]:

$$p_w^{sat} = a \exp\left(\frac{bT}{T+c}\right) \quad (2.14)$$

with T measured in °C and the empirical coefficients reported in Table 2.1.

p_w^{sat} (bar)	a	b	c
	6.1121	10 ⁻³	17.123
			234.95

Table 2.1. Saturated water vapour pressure coefficients [17]

By substituting the activity definition in Equation 2.13 in 2.12, it follows that:

$$E = \underbrace{\frac{\Delta\bar{g}_{reaction}(T_{cell}, p_0)}{z_F F}}_{u_{rev}(T)} - \frac{RT_{cell}}{z_F F} \ln\left(\frac{p_w^{sat}/p_0}{p_{H_2}/p_0 (p_{O_2}/p_0)^{1/2}}\right) \quad (2.15)$$

with p_{H_2} and p_{O_2} , respectively, the partial pressure of hydrogen and oxygen calculated assuming to have, at each time interval, liquid water at its thermodynamic equilibrium with water vapour. In particular, according to **Dalton's law**, a mixture of ideal gas can be written according to the following expressions:

$$p_{O_2} = P_{an} - p_w^{sat} \quad \text{and} \quad p_{H_2} = P_{cat} - p_w^{sat}. \quad (2.16)$$

The reversible voltage u_{rev} can be calculated directly with empirical equations related to the molar enthalpy and molar entropy, or directly with the following equation [18]:

$$u_{rev} = u_{std} - 0.0009 (T - T_{std}) \quad (2.17)$$

where u_{std} is equal to 1.229 V and T_{std} to 298.15 K.

2.1.1.2 Activation overvoltage

The first form of loss is the one related to the charge transfer, mainly due to the electrochemical kinetic reaction at the electrodes. It is possible to calculate the current density at the electrode/membrane interface through the Butler - Volmer [19] equation (2.18):

$$i = i_0 \left[\exp\left(\frac{\alpha_{an} z F}{RT} \eta_{act}\right) - \exp\left(\frac{\alpha_{cat} z F}{RT} \eta_{act}\right) \right] \quad (2.18)$$

where

1. i_0 exchange current density measured in A/cm²;
2. α_{an} anodic charge transfer coefficient (-);
3. α_{cat} cathodic charge transfer coefficient (-);
4. η_{act} activation overvoltage measured in V.

Assuming $\alpha_a = \alpha_c$ and being $y(x) = \frac{e^x - e^{-x}}{2} = \sinh(x)$, it follows that:

$$\eta_{act,anode} = \frac{RT}{\alpha_{an} F} \sinh^{-1}\left(\frac{i}{2i_{0,an}}\right) \quad (2.19)$$

and

$$\eta_{act,cathode} = \frac{RT}{\alpha_{cat} F} \sinh^{-1}\left(\frac{i}{2i_{0,cat}}\right) \quad (2.20)$$

Considering $\eta_{act} = \eta_{act,anode} + \eta_{act,cathode}$:

$$\eta_{act} = \frac{RT}{\alpha_{an} F} \sinh^{-1}\left(\frac{i}{2i_{0,an}}\right) + \frac{RT}{\alpha_{cat} F} \sinh^{-1}\left(\frac{i}{2i_{0,cat}}\right). \quad (2.21)$$

However, the kinetic regarding the hydrogen evolution at the cathode is way faster than the oxygen one taking place at the cathode. For this reason, the overvoltage related to the cathodic reaction can be neglected.

In order to calculate the activation overvoltage it is necessary to define the anodic charge transfer coefficient α_{an} and the anodic exchange current density $i_{0,an}$. The charge transfer coefficient is defined between 0 and 1 ($0 \leq \alpha \leq 1$) and a value of $\alpha_{an} = 0.7353$ has been used in accordance with Espinosa-López et al. [18]. The anodic exchange current density $i_{0,an}$ can be defined through an Arrhenius expression [20] as follows:

$$i_{0,an} = i_{0,an,std} \exp\left[-\frac{E_{exc}}{R} \left(\frac{1}{T} - \frac{1}{T_{std}}\right)\right] \quad (2.22)$$

where E_{exc} is the activation energy required for the electron transport in the anode electrode, while $i_{0,an,std}$ is the exchange current density at standard pressure p_{std} and temperature $T_{std} = 298.15$ K. According to Espinosa-López et al. [18] $i_{0,an,std} = 1.08 \cdot 10^{-8}$ A/cm² and $E_{exc} = 52994$ J/mol.

2.1.1.3 Ohmic overvoltage

The second type of loss is the ohmic overvoltage, the only one having a linear trend. As the name suggests, this source of loss depends on the electric resistivity encountered by migrating charges: electrons and ions.

From **Ohm's law**:

$$\eta_{ohm} = (R_{el} + R_{memb}) I \quad (2.23)$$

where R_{el} takes into account the electrical resistance through the electrodes, external circuit and bipolar plates (electron e^- paths), also called interconnectors, while R_{memb} the one related to the polymeric electrolyte (proton H^+ paths). Developing Equation 2.23, it follows that

$$\eta_{ohm} = \left[\left(\sigma^{-1} \frac{\delta}{S} \right)_{e^-} + \left(\sigma^{-1} \frac{\delta}{S} \right)_{ions} \right] i S = (ASR_{e^-} + ASR_{ions}) i \quad (2.24)$$

where ASR , measured in $\Omega \text{ cm}^2$, is the **area of specific resistance** and depends on:

1. $\sigma = \sigma(\text{material}, \text{thermodynamics})$ conductivity of the material with $[\sigma] = \text{S}$;
2. δ thickness of the material¹ with $[\delta] = \text{cm}$.

The electronic conductivity σ_{e^-} is usually way higher than the protonic conductivity σ_{ions} , making the electronic resistance negligible [20].

The membrane protonic conductivity depends on the water content of the membrane itself. Nafion membrane works well only if sufficiently hydrated, thus imposing several constraints. In fact, at ambient pressure, the system cannot exceed 100 °C to prevent water from boiling and, as a consequence of the temperature constraint, the kinetics of the reaction will be slow. To speed it up, a layer of Pt-Ir (or Pt-IrO₂) is deposited on the electrodes to act as a catalyst, bringing up the costs.

It has been demonstrated to be effective to calculate the membrane protonic conductivity through an Arrhenius expression [20] as follows:

$$\sigma_{mem} = \sigma_{mem, std} \exp \left[-\frac{E_{pro}}{R} \left(\frac{1}{T} - \frac{1}{T_{std}} \right) \right] \quad (2.25)$$

where E_{pro} is the activation energy required for the proton transport in the electrolyte and $\sigma_{mem, std}$ is the membrane protonic conductivity at standard pressure p_{std} and temperature $T_{std} = 298.15 \text{ K}$. According to Espinosa-López et al. [18] $\sigma_{memb, std} = 0.1031 \text{ S/cm}$ and $E_{pro} = 10536 \text{ J/mol}$.

¹The objective is to make it small enough to reduce the losses, but, at the same time, avoid short-circuiting the cell.

2.1.1.4 Concentration overvoltage

The last loss contribution is the one due to mass transport phenomena, non-linear as the activation overvoltage 2.1.1.2. At high current densities, products cannot be removed as fast as they are produced, thus leading to a decrease of the electrolyser efficiency. Since the reaction is taking place at the membrane-electrode interface, the molecules flowing inside the electrodes will encounter limitations due to the porous structure of the electrodes themselves. While increasing the mass flow, resistances increase, bringing to losses that must be overcome paying a price in terms of voltage applied at the electrodes, which can be translated as more power consumption.

The diffusion overvoltage can be estimated through the Nernst equation:

$$\eta_{conc} = V_1 - V_0 = (u_{rev} - \frac{RT}{zF} \ln C_1) - (u_{rev} - \frac{RT}{zF} \ln C_0) = \frac{RT}{zF} \ln \frac{C_1}{C_0} \quad (2.26)$$

where the "0" condition is the one taken as reference. By applying Equation 2.26 to the anode and cathode, it follows that:

$$\eta_{conc,an} = \frac{RT_{an}}{4F} \ln \frac{C_{O_2}^{mem}}{C_{O_2,0}^{mem}} \quad (2.27)$$

and

$$\eta_{conc,cat} = \frac{RT_{cat}}{2F} \ln \frac{C_{H_2}^{mem}}{C_{H_2,0}^{mem}}, \quad (2.28)$$

with $C_{O_2}^{mem}$ and $C_{H_2}^{mem}$ the oxygen and hydrogen concentration at the membrane-electrode interface.

However, this phenomenon is difficult to observe at a current density typical of commercial PEM electrolysers. For example, the work conducted by a team consisting of Giner, Inc. (Giner), Virginia Polytechnic Institute & University (VT), and domnick hunter group, a subsidiary of Parker Hannifin (Parker) [21], did not report concentration overvoltage with the electrolyser operating between 3 A/cm⁻² and 5 A/cm⁻². In this model, the validation will be conducted on a similar electrolyser and, based on their results, the current density will not go over 3 A/cm⁻² as previously mentioned in the Hypotheses (Section 2.1). For this reason, the concentration overvoltage has been neglected.

Figure A.2 presented in the Appendix reports the electrochemical submodel implemented in the Simulink[®] environment.

2.1.2 Mass transport submodel

The investigation of the molar flow rates inside the electrolyser is a fundamental step to design a realistic model on the Simulink[®] environment, especially water

exchanges through the electrolytic membrane. To do this, a thorough analysis of the mass flow contributions, considering each part of the cell that are anode, cathode and membrane, will be conducted.

2.1.2.1 Anode molar flow rate analysis

In order to better understand the flow rates interested in the anode ancillary, Figure 2.2 is proposed below.

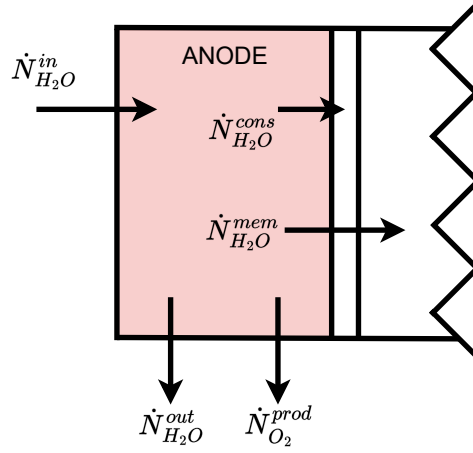


Figure 2.2. Molar flow exchanges - anode

The following mass balances are considered [22] according to the law of conservation of mass:

$$\frac{dN_{H_2O}}{dt} = \dot{N}_{H_2O}^{in} - \dot{N}_{H_2O}^{out} - \dot{N}_{H_2O}^{mem} - \dot{N}_{H_2O}^{cons} \quad (2.29)$$

and

$$\frac{dN_{O_2}}{dt} = \dot{N}_{O_2}^{in} - \dot{N}_{O_2}^{out} + \dot{N}_{O_2}^{prod}. \quad (2.30)$$

However, obviously, the term $\dot{N}_{O_2}^{in}$ is zero, because no oxygen is injected, while the oxygen produced $\dot{N}_{O_2}^{prod}$ is exactly the one exiting from the anode, in accordance with the hypotheses of steady-state ($dN_{O_2}/dt = 0$) and of diffusion of H_2 and O_2 through the membrane, as well as their solubility in water, negligible. As a consequence, by applying the Faraday's law (Equation 2.3):

$$\dot{N}_{O_2} = \dot{N}_{O_2}^{out} = \dot{N}_{O_2}^{prod} = \frac{N I}{4F}. \quad (2.31)$$

The same reasoning can be applied to the water mass balance, that results in $dN_{H_2O}/dt = 0$. The net molar flux of water passing through the anode is

$$\dot{N}_{H_2O}^{an} = \dot{N}_{H_2O}^{in} - \dot{N}_{H_2O}^{out} = \dot{N}_{H_2O}^{mem} + \dot{N}_{H_2O}^{cons} \quad (2.32)$$

and it is exactly Equation 2.32 that will be implemented in Simulink[®] (as regards the anode ancillary). The anode will have $\dot{N}_{\text{H}_2\text{O}}^{an}$ as an input, reason why the two terms $\dot{N}_{\text{H}_2\text{O}}^{mem}$ and $\dot{N}_{\text{H}_2\text{O}}^{cons}$ need to be evaluated. The calculation regarding the consumed water is pretty trivial, in fact, thanks to the Faraday's law (Equation 2.3), it can be easily derived:

$$\dot{N}_{\text{H}_2\text{O}}^{cons} = \frac{N I}{2F}. \quad (2.33)$$

Before moving on with the analysis of the membrane water transport $\dot{N}_{\text{H}_2\text{O}}^{mem}$, it is necessary to deepen the mass transport regarding the cathode.

Figure A.3 presented in the Appendix reports the anode submodel implemented in the Simulink[®] environment.

2.1.2.2 Cathode molar flow rate analysis

In order to better understand the flow rates interested, Figure 2.3 is proposed below. Again, as previously seen in the anode molar flow rate analysis, the following

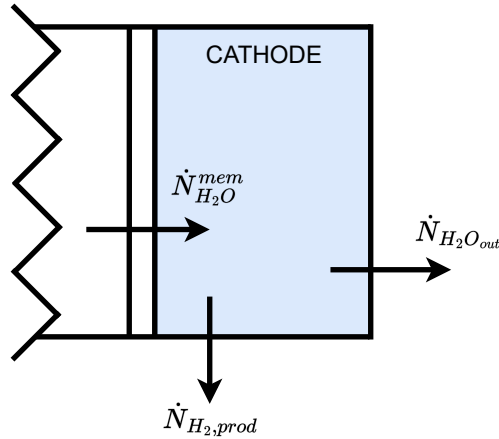


Figure 2.3. Molar flow exchanges - cathode

equations can be derived from the law of conservation of mass:

$$\frac{dN_{\text{H}_2\text{O}}}{dt} = \dot{N}_{\text{H}_2\text{O}}^{in} - \dot{N}_{\text{H}_2\text{O}}^{out} - \dot{N}_{\text{H}_2\text{O}}^{mem} \quad (2.34)$$

and

$$\frac{dN_{\text{H}_2}}{dt} = \dot{N}_{\text{H}_2}^{in} - \dot{N}_{\text{H}_2}^{out} + \dot{N}_{\text{H}_2}^{prod}. \quad (2.35)$$

Considering the steady-state condition, the net water flux at the cathode results to be:

$$\dot{N}_{\text{H}_2\text{O}}^{cat} = \dot{N}_{\text{H}_2\text{O}}^{in} - \dot{N}_{\text{H}_2\text{O}}^{out} = \dot{N}_{\text{H}_2\text{O}}^{mem}. \quad (2.36)$$

As regards the hydrogen, $\dot{N}_{\text{H}_2}^{in}$ is zero, because there is any H_2 introduction from outside the stack, as well as $dN_{\text{H}_2}/dt = 0$, therefore it follows that:

$$\dot{N}_{\text{H}_2} = \dot{N}_{\text{H}_2}^{out} = \dot{N}_{\text{H}_2}^{prod} = \frac{N I}{2F}. \quad (2.37)$$

To evaluate the water mass flow rate in the cathode, it is necessary to evaluate the water transported across the membrane $\dot{N}_{\text{H}_2\text{O}}^{mem}$, as Equation 2.36 reports.

Figure A.4 presented in the Appendix reports the cathode submodel implemented in the Simulink® environment.

2.1.2.3 Membrane molar flow rate analysis

The water flux flowing through the membrane $\dot{N}_{\text{H}_2\text{O}}^{mem}$ consists of two terms, both depending on two separate phenomena, the electro-osmotic drag $\dot{N}_{\text{H}_2\text{O}}^{eod}$ and the concentration diffusion $\dot{N}_{\text{H}_2\text{O}}^{dd}$. The water transport due to the possible difference in terms of pressure between anode and cathode has been neglected, in accordance to the initial hypotheses (Section 2.1). Although some authors have taken this into account, as Abdin et al. [22] and Marangio et al. [23], other simulations [24] have shown how this term is effectively negligible, therefore it follows that:

$$\dot{N}_{\text{H}_2\text{O}}^{mem} = \dot{N}_{\text{H}_2\text{O}}^{eod} + \dot{N}_{\text{H}_2\text{O}}^{dd}. \quad (2.38)$$

The electro-osmotic drag is an electrical phenomenon that arises when the proton H^+ , passing through the membrane, brings with themselves water molecules. The term accounting for the amount of water molecules transported is the electro-osmotic drag coefficient n_d ($\text{mol}_{\text{H}_2\text{O}}/\text{mol}_{\text{H}^+}$). The water molar flux can be estimated with the following formula [25]:

$$\dot{N}_{\text{H}_2\text{O}}^{eod} = n_d \frac{N I}{F}. \quad (2.39)$$

As regards n_d , there are several ways to calculate it. Some authors suggest a temperature dependency, like Onda et al. [27], Ge et al. [28] or Yigit et al. [30], others a water content dependency (in fact, the more the membrane is hydrated, the better it will conduct protons), like Gorgun et al. [31]. There are also authors that decided to take it as constant, like Marangio et al. [23] or Xie et al. [29]. In this analysis it has been decided to choose an electro-osmotic drag coefficient temperature dependent, and in order to select which correlation adopt, looking at the scientific literature and noting that the values for n_d varies between 2.5 [29] and 7 [23], the correlation of Onda et al. [27] has been used, that is the following:

$$n_d = 0.0134 T + 0.03. \quad (2.40)$$

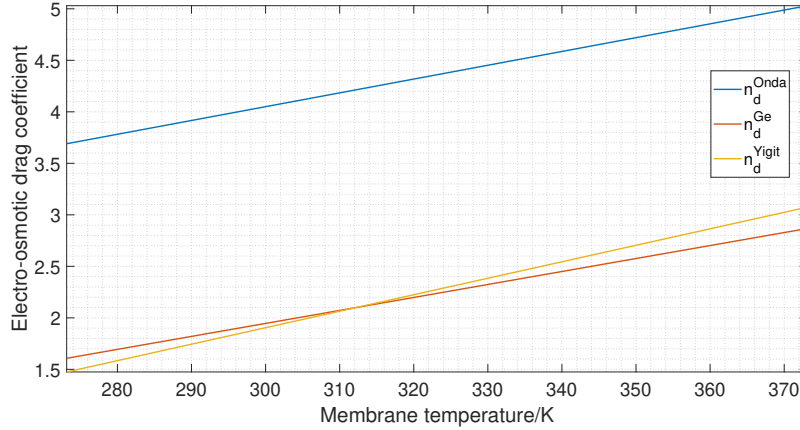


Figure 2.4. Electro-osmotic drag coefficient dependency from membrane temperature

A comparison between Onda et al. [27], Ge et al. [28] and Yigit et al. [30] electro-osmotic drag coefficient is reported in Figure 2.4.

As regards the water transport due to the concentration diffusion, its definition is more complicated. The phenomenon arises due to the fact that there is a water concentration gradient across the polymeric membrane, generating a flow mainly from the anode to the cathode (see Figure 2.5). The phenomenon can be described through the **Fick's first law** [25]:

$$\vec{J} = -D\nabla\varphi \quad (2.41)$$

where

1. J is the diffusion flux vector (mol/cm²/s);
2. D is the diffusion coefficient or diffusivity (cm²/s);
3. φ is the concentration (mol/cm³).

By developing the above equation, assuming a linear water concentration gradient, by integrating between the two membrane interfaces and considering the one-dimensionality of the problem, the following relation follows

$$\dot{N}_{H_2O}^{dd} = -N \frac{AD_w}{\delta_m} (C_{H_2O,cat}^{mem} - C_{H_2O,an}^{mem}), \quad (2.42)$$

with A (cm²) the active area of MEA (membrane electrodes assembly), D_w (cm²/s) the diffusivity, δ_m (cm) the membrane thickness, $C_{H_2O,cat}^{mem}$ (mol/cm³) the water concentration at the membrane-cathode interface and $C_{H_2O,an}^{mem}$ (mol/cm³) the water concentration at the anode-membrane interface.

Water concentrations at the electrode-membrane interface can be expressed in terms of concentration in the electrode channels $C_{\text{H}_2\text{O}}^{\text{ch}}$. Particularly, the conventions between $C_{\text{H}_2\text{O}}^{\text{mem}}$ and $C_{\text{H}_2\text{O}}^{\text{ch}}$, as Figure 2.5 reports, can be considered.

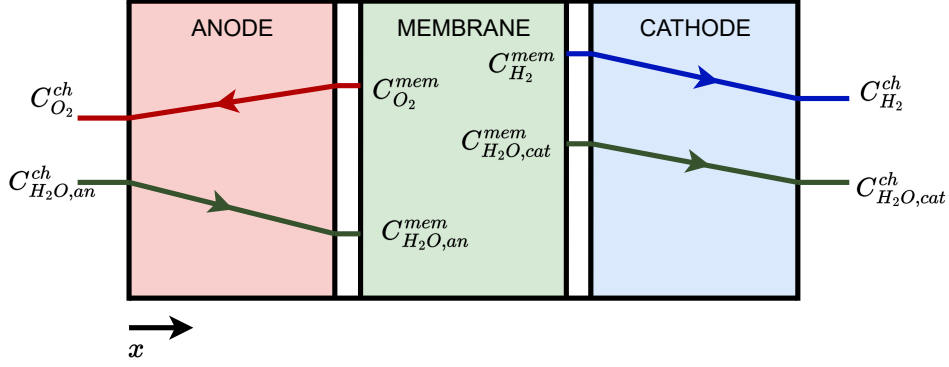


Figure 2.5. Qualitative representation of water concentration levels

Equation 2.42 is written with the x-axis pointing towards right as a reference, but it is random, it could be the opposite; the mechanism would work in the same way and the molar flow rate would have only a minus in front. The fact that, in Figure 2.5, the $C_{\text{H}_2\text{O},\text{cat}}^{\text{mem}}$ is greater than $C_{\text{H}_2\text{O},\text{an}}^{\text{mem}}$, derives from an empirical observation by running the model, but they could change according to the boundary conditions. Once the formula is written in the correct way, i.e. respecting the chosen reference system, it will work for each situation.

According to **Fick's first law** (Equation 2.41):

$$\dot{N}_{\text{H}_2\text{O}}^{\text{an}} = N \frac{AD_{\text{eff}}^{\text{an}}}{\delta_{\text{an}}} (C_{\text{H}_2\text{O},\text{an}}^{\text{ch}} - C_{\text{H}_2\text{O}}^{\text{mem}}) \quad (2.43)$$

and

$$\dot{N}_{\text{H}_2\text{O}}^{\text{cat}} = N \frac{AD_{\text{eff}}^{\text{cat}}}{\delta_{\text{cat}}} (C_{\text{H}_2\text{O},\text{cat}}^{\text{mem}} - C_{\text{H}_2\text{O},\text{cat}}^{\text{ch}}). \quad (2.44)$$

Therefore,

$$C_{\text{H}_2\text{O},\text{an}}^{\text{mem}} = C_{\text{H}_2\text{O},\text{an}}^{\text{ch}} - \frac{\dot{N}_{\text{H}_2\text{O}}^{\text{an}} \delta_{\text{an}}}{NAD_{\text{eff}}^{\text{an}}} \quad (2.45)$$

and

$$C_{\text{H}_2\text{O},\text{cat}}^{\text{mem}} = C_{\text{H}_2\text{O},\text{cat}}^{\text{ch}} + \frac{\dot{N}_{\text{H}_2\text{O}}^{\text{cat}} \delta_{\text{cat}}}{NAD_{\text{eff}}^{\text{cat}}}. \quad (2.46)$$

By substituting Equation 2.32 and 2.36 in Equation 2.45 and 2.46, it follows that:

$$C_{\text{H}_2\text{O},an}^{mem} = C_{\text{H}_2\text{O},an}^{ch} - \frac{(\dot{N}_{\text{H}_2\text{O}}^{mem} + \dot{N}_{\text{H}_2\text{O}}^{cons}) \delta_{an}}{NAD_{eff}^{an}} \quad (2.47)$$

and

$$C_{\text{H}_2\text{O},cat}^{mem} = C_{\text{H}_2\text{O},cat}^{ch} + \frac{\dot{N}_{\text{H}_2\text{O}}^{mem} \delta_{cat}}{NAD_{eff}^{cat}}. \quad (2.48)$$

Considering that water is present in liquid form in the channels:

$$C_{\text{H}_2\text{O},an}^{ch} = \frac{\rho_{\text{H}_2\text{O}}(T_{an})}{M_{m,\text{H}_2\text{O}}} \quad \text{and} \quad C_{\text{H}_2\text{O},cat}^{ch} = \frac{\rho_{\text{H}_2\text{O}}(T_{cat})}{M_{m,\text{H}_2\text{O}}}, \quad (2.49)$$

with $\rho_{\text{H}_2\text{O}}$ the liquid water density kept as constant, i.e. $\rho_{\text{H}_2\text{O}} = 1 \text{ g/cm}^3$, being its variation (in the operating temperature range of our device) small, and $M_{m,\text{H}_2\text{O}}$ (g/mol) the molar mass of water.

Analysing the second term of Equation 2.45 and 2.46, the unknowns are: D_{eff}^{an} , D_{eff}^{cat} , $\dot{N}_{\text{H}_2\text{O}}^{an}$ and $\dot{N}_{\text{H}_2\text{O}}^{cat}$. Regarding the first two unknowns, they are, respectively, the $\text{O}_2/\text{H}_2\text{O}$ and $\text{H}_2/\text{H}_2\text{O}$ effective binary diffusivity and they can be calculated applying the porosity correction to the formula used to estimate the diffusion coefficients for binary systems. The following equation for estimating the diffusion coefficient, at low pressures, has been developed from a combination of kinetic theory and corresponding-states arguments [25]:

$$P D_{AB} = a \left(\frac{T}{\sqrt{T_A^c T_B^c}} \right)^b (p_A^c p_B^c)^{1/3} (T_A^c T_B^c)^{5/12} \left(\frac{1}{M_A} + \frac{1}{M_B} \right)^{1/2} \quad (2.50)$$

where

1. P is the pressure, measured in atm, at the inlet of the electrode channels and it is known, being a design parameter;
2. D_{AB} is the diffusivity of the chemical species pair AB in cm^2/s ;
3. T_A^c , T_B^c , p_A^c , p_B^c are respectively the critical temperature in K and pressure in atm of chemical species A and B (Table 2.2);
4. a and b are dimensionless empirical coefficients, taken as $3.64 \cdot 10^{-4}$ and 2.334 [34] respectively, valid for pairs of H_2O and a non-polar gas.

Finally, by applying the porosity correction mentioned before and suggested by Tomadakis et al. [26], valid for random fibrous porous media representing the diffusion layer of the electrode, it follows that:

$$D_{eff,AB} = D_{AB} \epsilon \left(\frac{\epsilon - \epsilon_p}{1 - \epsilon_p} \right)^\alpha, \quad (2.51)$$

	H ₂	O ₂	H ₂ O
p_c (atm)	12.8	49.7	218.3
T_c (K)	33.3	154.4	647.3
M_m (g/mol)	2	32	18

Table 2.2. Critical pressure, critical temperature and molar mass of hydrogen, oxygen and water [35]

where ϵ is the porosity of the electrodes, ϵ_p is the percolation threshold and α is an empirical coefficient. Those values are taken, respectively, like 0.3 [32] that is a value widely use in literature, 0.11 valid for two-dimensional, long and overlapping random fiber layers and 0.785 valid in case of cross-plane diffusion [33].

Now, starting from Equation 2.38 and by substituting both Equation 2.39 and 2.42, it follows that:

$$\dot{N}_{\text{H}_2\text{O}}^{\text{mem}} = \dot{N}_{\text{H}_2\text{O}}^{\text{eod}} + \dot{N}_{\text{H}_2\text{O}}^{\text{dd}} = n_d \frac{N I}{F} - N \frac{A D_w}{\delta_m} (C_{\text{H}_2\text{O},\text{cat}}^{\text{mem}} - C_{\text{H}_2\text{O},\text{an}}^{\text{mem}}). \quad (2.52)$$

By substituting in the above equation the relative expressions for $C_{\text{H}_2\text{O},\text{cat}}^{\text{mem}}$ and $C_{\text{H}_2\text{O},\text{an}}^{\text{mem}}$, that are Equation 2.47 and 2.48, the expression for $\dot{N}_{\text{H}_2\text{O}}^{\text{mem}}$ can be derived:

$$\dot{N}_{\text{H}_2\text{O}}^{\text{mem}} = N \frac{\frac{I}{F} \left(n_d - \frac{1}{2} \frac{D_w}{D_{\text{eff}}^{\text{an}}} \frac{\delta_{\text{an}}}{\delta_m} \right) - A \frac{D_w}{\delta_m} (C_{\text{H}_2\text{O},\text{cat}}^{\text{ch}} - C_{\text{H}_2\text{O},\text{an}}^{\text{ch}})}{\left[1 + \frac{D_w}{\delta_m} \left(\frac{\delta_{\text{cat}}}{D_{\text{eff}}^{\text{cat}}} + \frac{\delta_{\text{an}}}{D_{\text{eff}}^{\text{an}}} \right) \right]}. \quad (2.53)$$

It is possible to expand even more the expression by substituting Equation 2.49, valid for the water concentrations in the channels. The result is

$$\dot{N}_{\text{H}_2\text{O}}^{\text{mem}} = N \frac{\frac{I}{F} \left(n_d - \frac{1}{2} \frac{D_w}{D_{\text{eff}}^{\text{an}}} \frac{\delta_{\text{an}}}{\delta_m} \right) - A \frac{D_w}{\delta_m} \left(\frac{\rho_{\text{H}_2\text{O}}(T_{\text{cat}}) - \rho_{\text{H}_2\text{O}}(T_{\text{an}})}{M_{m,\text{H}_2\text{O}}} \right)}{\left[1 + \frac{D_w}{\delta_m} \left(\frac{\delta_{\text{cat}}}{D_{\text{eff}}^{\text{cat}}} + \frac{\delta_{\text{an}}}{D_{\text{eff}}^{\text{an}}} \right) \right]}, \quad (2.54)$$

but having assumed a low water density dependency on temperature, and so having imposed $\rho_{\text{H}_2\text{O}}$ as a constant, as well as a temperature uniformity along the stack, it follows that:

$$\dot{N}_{\text{H}_2\text{O}}^{\text{mem}} = N \frac{\frac{I}{F} \left(n_d - \frac{1}{2} \frac{D_w}{D_{\text{eff}}^{\text{an}}} \frac{\delta_{\text{an}}}{\delta_m} \right)}{\left[1 + \frac{D_w}{\delta_m} \left(\frac{\delta_{\text{cat}}}{D_{\text{eff}}^{\text{cat}}} + \frac{\delta_{\text{an}}}{D_{\text{eff}}^{\text{an}}} \right) \right]}. \quad (2.55)$$

Finally, the net molar flows at the anode $\dot{N}_{\text{O}_2}^{an}$ and at the cathode $\dot{N}_{\text{H}_2}^{cat}$ (Equation 2.32 and 2.36) can be evaluated, as well as the molar flow of water that crosses the polymeric membrane $\dot{N}_{\text{H}_2\text{O}}^{mem}$. Table 2.3 summarises the MEA design variables. However, in order to calculate the molar flows, it is necessary to know the tem-

Design variable	Value	Unit of measure
D_w	$1.28 \cdot 10^{-6}$ [34]	cm^2/s
δ_m	0.0178	cm
δ_{an}	0.0215	cm
δ_{cat}	0.0215	cm

Table 2.3. MEA design parameters

perature. In the following section the thermal submodel implementation will be discussed.

Figure A.5 presented in the Appendix reports the membrane submodel implemented in the Simulink[®] environment.

2.1.3 Thermal submodel

The design of a thermal submodel is fundamental to compute a successful electrolyser model, in fact the temperature of the device affects several variables, like the pressures, the stack voltage, the species concentration, etc.

The idea is to consider two different circuits, i.e. two loops, in which water flows. The first one goes from anode to cathode, in particular water is injected in excess in the anode so that the water splitting reaction can take place, the hydration of the membrane is ensured, and heat can be removed. The way heat is removed is through a heat exchanger connected to a second water loop, external to the electrolyser. The first loop has been considered as the control volume and the physics associated is zero-dimensional (0D), as a consequence of uniform temperatures across the stack assumption (see Hypotheses in Section 2.1). Hence, the temperature gradients along the circuit are neglected, leading to the following equation (energy balance) [44]:

$$C_{th} \frac{dT}{dt} = \sum_{j=1}^M \Phi_j - \sum_{i=1}^N \dot{N}_i \Delta h_i \quad (2.56)$$

where C_{th} (J/K) is the overall lumped thermal capacity that could be assumed equal to the thermal capacity of water, but in this project it is equal to 162116 J/K as reported by Espinosa-López et al. [18], T (K) the temperature, t (s) the time and Φ_j (W) the j -th heat flux exchanged between the first loop and the system,

including the electrolyser heat generation, the heat produced by the water pump, the heat losses to the environment and the heat exchanger (cooling flux), therefore the second loop. In particular:

$$\sum_{j=1}^M \Phi_j = \Phi_{PEMWE} + \Phi_{pump} - \Phi_{cooling} - \Phi_{loss}. \quad (2.57)$$

Usually, in thermodynamic applications, $\Phi > 0$ stands for heat flux absorbed by the first loop, so the one considered as the control volume, while $\Phi < 0$ means the opposite, therefore heat flux rejected.

In the following sections, each term of Equation 2.57, starting from the heat generation, hence Φ_{PEMWE} , will be analysed.

2.1.3.1 Heat generation

In a stack driving a **nonspontaneous reaction**, i.e. $\Delta\bar{g}_{reaction} > 0$, and so consuming electrical power (as in the case of an electrolyser), two sources of heat can be identified:

1. Heat absorbed by the endothermic reaction, i.e. $\bar{q}_{react} = N T \Delta\bar{s}_{reaction} > 0$ (heat sink) in J/mol.

The heat of reaction can be defined in terms of heat flux (W) as follows:

$$\Phi_{react} = N \bar{q}_{react} \dot{N}_F = N T \Delta\bar{s}_{reaction} \frac{I}{zF}. \quad (2.58)$$

2. Heat produced by relative irreversibilities of transport processes, i.e. Φ_{irr} (W), always exothermic. It is connected to the overpotentials, in particular:

$$\Phi_{irr} = N I \sum_{k=1}^3 \eta_k. \quad (2.59)$$

As a convention, Φ_{react} enters the stack, while Φ_{irr} exit the stack, being exothermic.



Figure 2.6. Heat fluxes in the stack

By applying a heat flux balance to the control volume depicted in Figure 2.6, it follows that:

$$\Phi_{stack} = \Phi_{react} - \Phi_{irr} = N I \left(\frac{T \Delta \bar{s}_{reaction}}{zF} - \sum_{k=1}^3 \eta_k \right). \quad (2.60)$$

In accordance with the definition of **Gibb's free energy** $\rightarrow T \Delta \bar{s}_{reaction} = \Delta \bar{h}_{reaction} - \Delta \bar{g}_{reaction}$, from which:

$$\Phi_{stack} = N I \left[\frac{\Delta \bar{h}_{reaction}}{zF} - \underbrace{\left(\frac{\Delta \bar{g}_{reaction}}{zF} + \sum_{k=1}^3 \eta_k \right)}_{V_{cell}} \right]. \quad (2.61)$$

From the equation above, it is noticeable that, when $V_{cell} = \frac{\Delta \bar{h}_{reaction}}{zF}$, then $\Phi_{stack} = 0$. This condition is known as **thermoneutral point**, from which the thermal neutral voltage is defined as follows:

$$V_{tn} = \frac{\Delta \bar{h}_{reaction}}{zF}. \quad (2.62)$$

Combining Equation 2.61 with Equation 2.62, it follows that

$$\Phi_{stack} = N I (V_{tn} - V_{cell}), \quad (2.63)$$

but being the control volume of our interest the first water loop:

$$\Phi_{PEMWE} = -\Phi_{stack} = N I (V_{cell} - V_{tn}). \quad (2.64)$$

The thermal neutral voltage V_{tn} is equal to 1.48 V at standard condition ($p_{std} = 1$ atm, $T_{std} = 298.15$ K) and it can be assumed as constant due to its slightly dependence from temperature [43]. It is evident from Equation 2.64 that, when the cell voltage goes below the thermal neutral one, the heat becomes negative, so the stack starts to absorb energy. In that condition, the heat flux produced by irreversibilities cannot withstand the heat demand of the endothermic reaction. On the contrary, when the difference of voltage in Equation 2.64 becomes positive, the heat produced is in excess compared to the one needed to run the reaction. When V_{cell} is equal to V_{tn} (thermoneutral point), an equilibrium point is reached, in which the demand of heat is completely satisfied by the irreversibilities. Usually, the electrolysers work at a voltage bigger than the thermoneutral one, thus needing to be cooled.

2.1.3.2 Pump heat

The heat flux transferred by the water pump, due to friction losses, can be computed firstly considering the theoretical power that needs to be supplied $P_{pump,th}$ to run the primary circuit (see Figure 2.1). In fact

$$P_{pump,th} = \frac{\dot{N}_{H_2O}^{an}}{M_{D,H_2O}} \Delta P_{pump} = \dot{V} \Delta P_{pump}, \quad (2.65)$$

where \dot{V} is the volumetric flow rate in m^3/s , that can be computed starting from the anode net water $\dot{N}_{H_2O}^{an}$ (Equation 2.32) and the water molar density M_{D,H_2O} of $54604 \text{ mol}/m^3$ ($p = 1 \text{ atm}$, $T = 333.15 \text{ K}$), while ΔP_{pump} is the pump total head assumed equal to 2 bar.

Assuming a motor efficiency η_{motor} of 75% (electricity to shaft) and a pump efficiency η_{pump} of 75% (shaft to fluid), the real amount of power that must be supplied to pump the water in the first loop is:

$$P_{pump,real} = \frac{P_{pump,th}}{\eta_{motor} \eta_{pump}}. \quad (2.66)$$

Applying the difference between the real power consumed and the theoretical one, the power dissipated as heat results to be:

$$\Phi_{pump} = P_{pump,real} - P_{pump,th} = P_{pump,th} \left(\frac{1}{\eta_{motor} \eta_{pump}} - 1 \right). \quad (2.67)$$

2.1.3.3 Auxiliary cooling

The temperature control inside the electrolyser is strictly dependent on $\Phi_{cooling}$, that is the heat exchanged between the first and second water loop, assuming a coaxial tube heat exchanger in parallel flow, for sake of simplicity.

It is well-known, from the heat exchanger theory [44], that both the water and the refrigerant temperature change along the heat exchanger (see Figure 2.7), therefore it is not possible to evaluate the heat flux through the classic equation valid for heat transfer, but it should be used the corrected one, i.e. the logarithmic mean temperature difference (LMTD) method, that is

$$\Phi_{cooling} = U A_{ex} \Delta T_{lm} = U A_{ex} \frac{\Delta T_1 - \Delta T_2}{\ln(\Delta T_1/\Delta T_2)}, \quad (2.68)$$

where:

$$\Delta T_1 = T_h^{in} - T_c^{in} \quad \text{and} \quad \Delta T_2 = T_h^{out} - T_c^{out}, \quad (2.69)$$

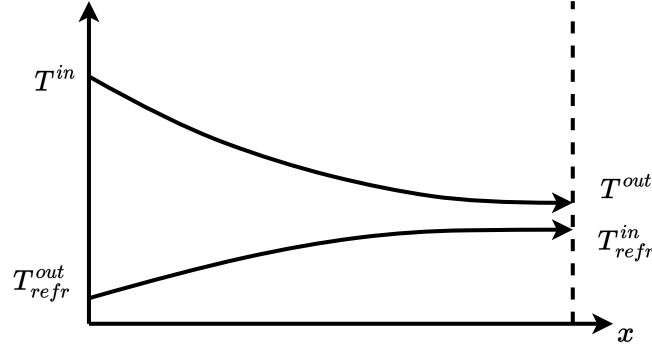


Figure 2.7. Qualitative temperature trends along the heat exchanger

with T_h that stands for the temperature of the hot fluid, while T_c for the cold one. The apex *in* and *out* are used to indicate "inlet" and "outlet" of the heat exchanger. U is the overall heat transfer coefficient, measured in $\text{W}/\text{m}^2/\text{K}$, and A_{ex} the heat exchange surface, evaluated in m^2 .

Unfortunately, this method requires to know four temperatures: the inlet ones are usually known and the outlet temperatures could be specified or readily determined from the energy balance expressions. However, if they are not, and so if only the inlet temperatures are known as in this case, the usage of this method could become non-trivial due to the necessity to implement several iterative cycles. Therefore, it is preferable to employ an alternative approach named the **ϵ -NTU method**. It requires the knowledge of both the inlet temperatures T_{refr}^{in} and T^{in} , plus the corresponding mass flow rates \dot{m}_{refr} and \dot{m} , both measured in kg/s . The last one can be simply calculated knowing that the water circulating in the first loop corresponds to the sum between the water injected (equal to the water consumed at the anode $\dot{N}_{\text{H}_2\text{O}}^{cons}$) and the water flowing through the membrane $\dot{N}_{\text{H}_2\text{O}}^{mem}$, therefore the net water at the anode $\dot{N}_{\text{H}_2\text{O}}^{an}$ (Equation 2.32):

$$\dot{m} = \frac{\dot{N}_{\text{H}_2\text{O}}^{cons} + \dot{N}_{\text{H}_2\text{O}}^{mem}}{M_{m,\text{H}_2\text{O}} 0.001} = \frac{\dot{N}_{\text{H}_2\text{O}}^{an}}{M_{m,\text{H}_2\text{O}} 0.001}. \quad (2.70)$$

Regarding the refrigerant mass flow rate \dot{m}_{refr} , a control system able to regulate the opening of a proportional electro-valve at the inlet of the heat exchanger (second loop), changing accordingly the amount of incoming refrigerant (Figure 2.8), has been imagined. The way the system decides how much refrigerant inject, and so how much open the valve, is by measuring the temperature difference between the stack temperature T and a reference one (T_{PID}).

What regulates the heat flux exchanged is the mass flow rate \dot{m}_{refr} . The valve is regulated by a PID (Proportional-Integral-Derivative) controller. This solution is largely adopted in automatic control systems and its working principle is based on

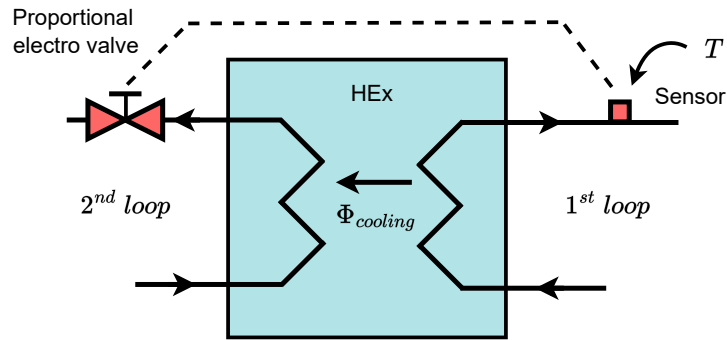


Figure 2.8. Qualitative representation of the heat exchanger

comparing an input value with a reference one, previously imposed. The difference, the so-called error signal, is then used to determine the value of the output variable of the controller. In this case the input value is the temperature T and the reference one, i.e. the T_{PID} , hence the operational temperature imposed for the electrolyser. The output of the controller (Figure 2.9) is the mass flow rate \dot{m}_{refr} which regulates the amount of heat that must be extracted from the device in order to maintain the PEMWE at the set temperature, therefore T_{PID} .

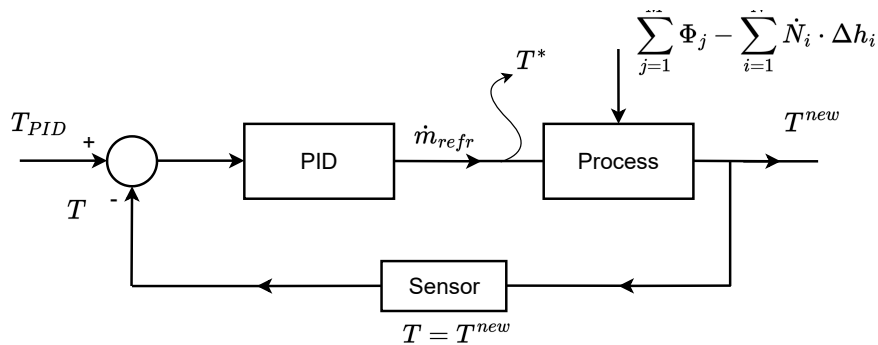


Figure 2.9. PID controller logic

If the temperature is below T_{PID} , that will be usually set at around 340 K, the mass flow rate injected is zero, in fact the heat exchanger will be activated only if the temperature rises over the set one.

The PID adopted in this model is actually a proportional controller, being the tuning of the PID itself very time-consuming and actually unnecessary. The PID controller provided by Simulink[®] was set with the proportional term P equal to 0.1 while the filter coefficient N to 100.

After these clarifications, the implementation of the ϵ -NTU method can proceed starting from some definitions, in particular regarding r_c , ϵ and NTU .

The **heat capacity ratio** r_c is function of the heat capacity rates, C_h and C_c , measured in W/K, in the following way:

$$r_c = \frac{C_{min}}{C_{max}}, \quad (2.71)$$

where

$$\begin{aligned} C_{min} &= \min(C_h, C_c), & C_h &= \dot{m} c_{H_2O}, \\ C_{max} &= \max(C_h, C_c) \quad \text{and} & C_c &= \dot{m}_{refr} c_{refr}. \end{aligned} \quad (2.72)$$

The **effectiveness** ϵ is defined as the ratio between the heat flux and maximum heat flux available in the following way:

$$\epsilon = \frac{\Phi_{cooling}}{\Phi_{cooling}^{max}}, \quad (2.73)$$

with

$$\Phi_{cooling}^{max} = C_{min} \Delta T_1 = C_{min} (T^{in} - T_{refr}^{in}). \quad (2.74)$$

The **number of transfer units** NTU is defined as:

$$NTU = \frac{U A_{ex}}{C_{min}}. \quad (2.75)$$

By applying the heat exchanger theory regarding the LMTD method [44] with the definitions just seen, it follows that:

$$\epsilon = \frac{1 - \exp[-NTU(1 + r_c)]}{1 + r_c}, \quad (2.76)$$

from which the evaluation of the auxiliary cooling is pretty trivial, in fact $\Phi_{cooling} = \epsilon \Phi_{cooling}^{max}$. The overall heat transfer coefficient U is assumed as constant and equal to 2000 W/m²/K, that is a reasonable value considering a heat transfer between two fluids, both assumed as water. The heat exchange area A_{ex} has been fixed, in the absence of data, to 15 m², in order to avoid a coolant flow rate too large compared to the one flowing in the first loop (\dot{m}).

Figure A.6 presented in the Appendix reports the heat exchanger submodel implemented in the Simulink[®] environment.

2.1.3.4 Heat loss in the environment

Part of the heat is dispersed in the environment Φ_{loss} and its amount is calculated using the electrical analogy, where the temperatures stand like a voltage, heat flux as a current, and the heat transfer physics (conduction, convection and radiation) is expressed through a thermal resistance R_{th} . It follows that

$$\Phi_{loss} = \frac{T - T_{amb}}{R_{th}}, \quad (2.77)$$

where T_{amb} the outdoor temperature, while the thermal resistance R_{th} has been evaluated by Espinosa-López et al. [18] experimentally from heating curves on a real demonstration plant, the 46 kW PEMWE installed on the MYRTE platform. In this project, a thermal insulation similar to the one studied by Espinosa-López et al. [18] has been assumed, i.e. $R_{th} = 0.0668$ K/W.

2.1.3.5 Mass transport heat

Finally, the last term of Equation 2.57, that represents the heat flux leaving the device through the chemical species O_2 and H_2 , and entering through H_2O^{inj} , can be described. It can be expressed according to the **first law of thermodynamics for open systems** [44]. The molar flow exiting the control volume has a positive sign, the one entering a negative one. It follows that:

$$\sum_{i=1}^N \dot{N}_i \Delta h_i = \dot{N}_{O_2} h_{O_2}(T) + \dot{N}_{H_2} h_{H_2}(T) - \dot{N}_{H_2O}^{inj} h_{H_2O}(T_{amb}). \quad (2.78)$$

In Equation 2.78, the amount of water injected is equal to the one that is consumed each time.

The values of the specific enthalpy of the oxygen, hydrogen and liquid water (kJ/mol/K) can be calculated through empirical correlation [35], which coefficients are summarised in Table 2.4, in the following way:

$$h - h_{298.15\text{ K}} = At + \frac{Bt^2}{2} + \frac{Ct^3}{3} + \frac{Dt^4}{4} - \frac{E}{t} + F - H, \quad (2.79)$$

with $t = T/1000$ (K).

Note that the water specific enthalpy is valid in the range 298 - 500 K, the hydrogen 298 - 1000 K, and oxygen 100 - 700 K.

The model regarding the electrolyser is definitely complete, what remains is a brief explanation on how the power signals, that will be employed in the next sections, have been generated.

Figure A.7 presented in the Appendix reports the thermal submodel implemented in the Simulink® environment.

	A	B	C	D	E	F	H
H ₂ (g)	33.066178	-11.363417	11.432816	-2.772874	-0.158558	-9.980797	0.0
O ₂ (g)	31.32234	-20.23531	57.86644	-36.50624	-0.007374	-8.903471	0.0
H ₂ O(l)	-203.6060	1523.290	-3196.413	2474.455	3.855326	-256.5478	-285.8304

Table 2.4. Specific enthalpy (kJ/mol) empirical correlation coefficients [35]

2.2 Offshore renewable energy devices

Offshore renewable energy devices, like wind turbines or wave energy converters, are expected to play a fundamental role in the climate change challenges. Large amount of zero-emission energy could be harvested by simply exploiting natural phenomena such as waves and wind. In the following subsections, a brief introduction of these devices will be made, explaining then how the power signals have been simulated.

2.2.1 Offshore wind turbines

In the last years, offshore wind farms have purchased popularity due to the higher power productivity compared to onshore wind ones. Far from the shore, the wind blows with larger intensity and constancy, and it is free from natural or artificial obstacles (such as buildings). In addition, larger farms can be created per square kilometers, as well as taller wind turbine allowing a greater energy harvesting. In fact, the wind power P_{wind} depends directly on average wind velocity v and rotor diameter in the following way:

$$P_{wind} = \frac{1}{2}\dot{m}_w v^2 = \frac{1}{2}\rho A v^3. \quad (2.80)$$

However, since downstream of the rotor the wind speed cannot be zero because it would violate the continuity equation (inlet mass flow rate \neq outlet mass flow rate), the maximum extractable power becomes

$$P_{th}^{max} = C_L P_{wind} = C_L \frac{1}{2}\rho A v^3, \quad (2.81)$$

where C_L is the **Betz limit** equal to $16/27 \approx 0.59$ [36].

It is possible to identify two types of offshore wind turbine: **bottom fixed** (Figure 2.10) and **floating** (Figure 2.11). The first one is already largely employed, specifically in northern Europe like Denmark, Germany, Netherlands, that are, respectively, the first, the second and the fourth country in the world for the wind electricity generation per capita [4]. These countries, including Norway, benefit of the strong winds blowing all over the year on the North Sea, as well as Sweden

and Finland that are able to harvest huge quantities of energy due to their closeness to the Baltic Sea. These are particularly interesting spots due to favourable bathymetry and capacity factors, in fact, being the bottom fixed technology based on underwater foundation, it is not economically feasible to install wind turbines for water depths exceeding 50 meters.

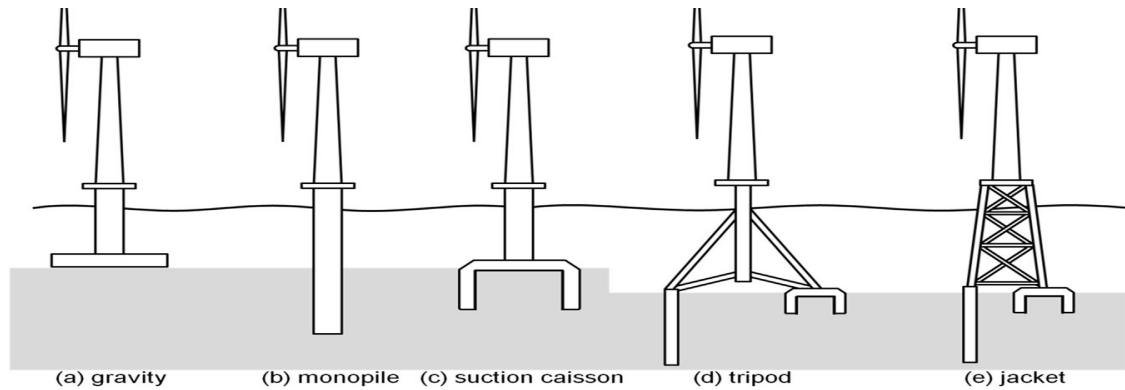


Figure 2.10. Types of foundation for offshore wind turbines [37]

Floating offshore has the goal to exceed this limit in order to install wind farms in deeper water and harvest even more energy in locations where, right now, it is not convenient. Moreover, other countries like France, Spain, Portugal, Ireland could exploit offshore winds coming from the Atlantic Ocean, as well as the ones in southern Europe, like Italy, could benefit from strong offshore winds blowing in the Mediterranean Sea (Channel of Sicily or south-west Sardinia, where the sea depth goes from 60 up to more than 500 m). Floating offshore wind turbine (FOWT) can be divided into three main categories: spar (ballast stabilized), semi-submersible (buoyancy stabilized) and tension leg platform (mooring stabilized), as depicted in Figure 2.11. Each of these has different pros and cons, moving from the good stability, simple design of spar types to low vessel requirement and onshore assembly of semi-submersible, while common cons are complex fabrication and bulky structures. These systems can rely on the decades of experience of the oil and gas (O&G) industry (Figure 2.12), that has already demonstrated the feasibility and survivability of offshore floating structures. The technology implemented, like mooring systems, tanks, and ballast options are already well developed. However, these designs must be re-analysed and designed in order to fit wind turbines need, like the different loads to which they are subjected, an aspect that makes costs rise, making the development of cost-effective offshore floating wind turbine challenging. In fact, if compared to bottom fixed offshore wind turbine, the modelling of these systems becomes more difficult due to the added complexity of simulate waves contribution, sea currents, as well as offshore wind force. Open-source softwares, like

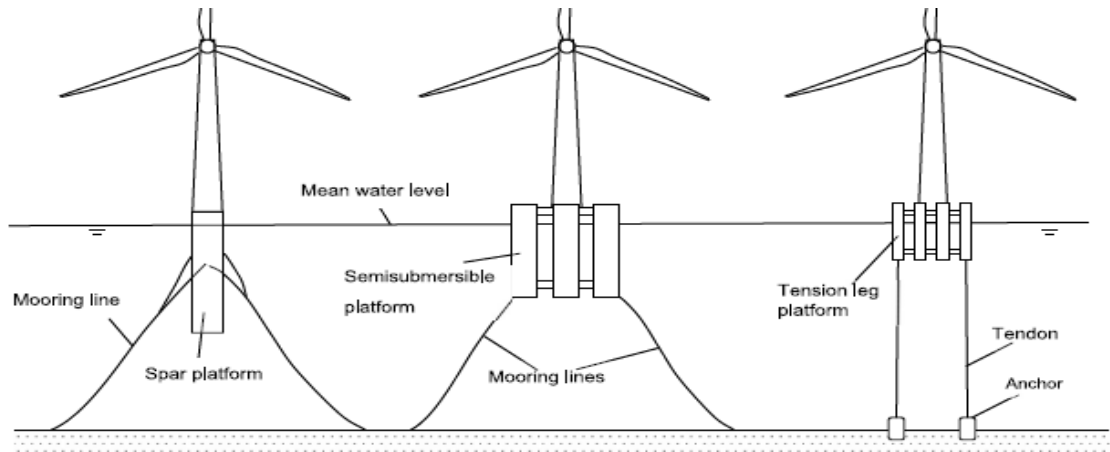


Figure 2.11. Schematic of spar, semisubmersible and tension leg platform floating wind turbines [38]

OpenFAST, permits to assess aerodynamics, hydrodynamics, control and electrical system (servo) dynamics, and structural dynamics to enable coupled nonlinear aero-hydro-servo-elastic simulation in the time domain.

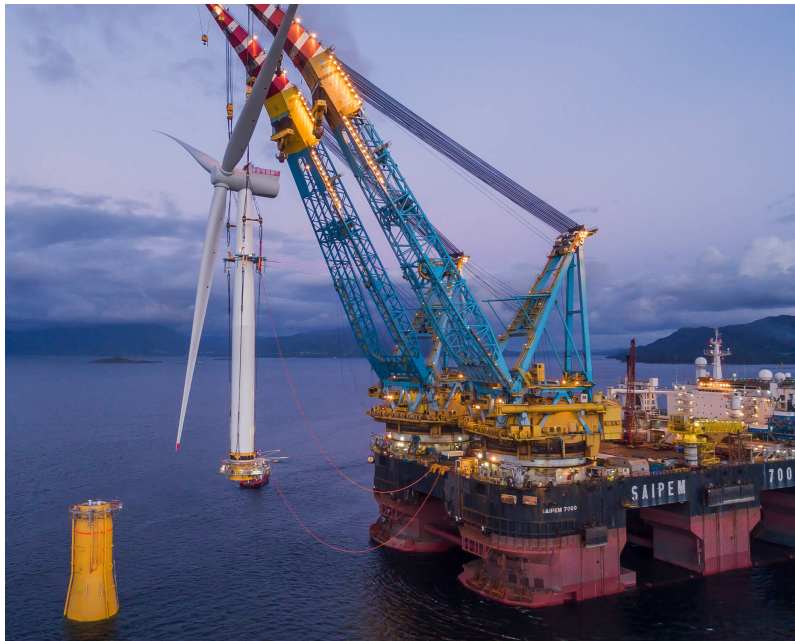


Figure 2.12. HyWind turbine installation by Saipem 7000 semi-submersible crane vessel [39]

Some projects have been already built during the last decade, such as HyWind in Scotland (5 turbines of 6 MW each), WindFloat off the Portuguese coast (3 turbines of 8.4 MW each) and Floatgen demonstrator (2 MW unit), France’s first offshore wind turbine.

2.2.2 Wave energy converters

The seas, since ancient times, have surprised humanity for the hidden strength often expressed through intense waves and strong currents. Currently, a still highly unexploited amount of renewable and non-pollutant energy is enclosed in the oceans. Wave energy converters (WEC) are intended to transform this ancient energy into electricity and the concepts developed to satisfy this goal are many. The first patent dates back to 1799, but the most research has been carried out in the last decades, starting from the late 20th century, where hundreds of patents were published as a result of the so-called oil crises. A WEC can be classified according to their positioning with respect to the shore (**shoreline**, **nearshore** and **offshore**), or to their dimension and orientation with respect to the wave: **terminators** if they physically intercept the incoming wave, **attenuators** if they extract energy as the wave passes through their length, **point absorber** if the horizontal dimension is negligible compared to the wavelength. The component responsible for the transformation of marine energy (wave) into electricity is the power take-off (PTO), a mechanic, electric or hydraulic-pneumatic mechanism.

In this project a **spar buoy**, i.e. a point absorber based on the oscillating water column principal, was chosen as a power generator. Going into more detail,

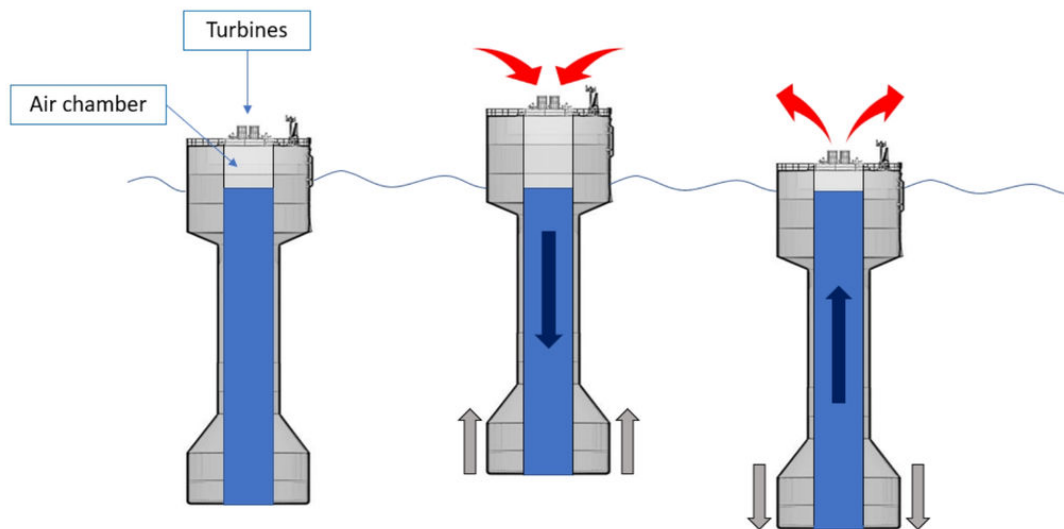


Figure 2.13. Scheme showing working principles of MARMOK-A-5 [40]

the spar buoy technology belongs to the simpler and more developed concept to harvest energy, that is floating oscillating water column. The device is a partly submerged structure (vertical tube fixed to a hollow floater that moves essentially in heave) open at both ends to water, below the water free surface, and atmosphere above, that can be anchored to the seafloor (floating) or directly bottom fixed. The trapped air, put in motion (compression and expansion alternatively) by the oscillations produced by incident waves over the floater (in case of floating device) and the water column inside the structure, drives a self-rectifying (bidirectional) air turbines connected to an electricity generator, thus converting mechanical energy into electricity [41]. A schematic is depicted in Figure 2.13 showing the working principle of MARMOK-A-5, a 30 kW nominal power spar buoy located in the Bay of Biscay, Spain (Figure 2.14). It is the first grid-connected maritime generator in Spain and one of the first in the world.

In order to simulate a floating oscillating water column device, the WEC-Sim (Wave Energy Converter Simulator) open-source software has been used. It is developed in the Matlab/Simulink® environment using the multi-body dynamic solver Simscape Multibody. A huge variety of systems can be modelled through this software, including mooring dynamics, nonlinear hydrodynamic bodies, passive yawing, batch simulations and many others. Principally, simulations in the time-domain are carried out by solving the governing wave energy converter equations of motion in 6 Cartesian degrees-of-freedom (DoF).



Figure 2.14. MARMOK-A-5 in the Bay of Biscay, Spain [42]

Chapter 3

Case study description

In this chapter, the case study will be described with a focus on the electrolysis plant (Section 3.1), where the characterising parameters will be mentioned, and on the power signals generated from a floating offshore wind turbine (Section 3.2) and a spar buoy (Section 3.3). In addition, Section 3.2 and Section 3.3 introduce some of the choices that were made to run the sensitivity analyses of Section 4.2.

3.1 Electrolysis plant

Working with large output-power systems such as wind turbines, the electrolyser needs to be scaled to properly match the power load. Typically, commercial high-power electrolysers are not a single large device, but smaller connected in parallel, so that the pressure and temperature homogeneity is ensured and the stresses are reduced. Some companies declare to have two stacks connected in parallel, such as ITM Power (two GEP Skid stack modules with 5 MW load capacity in total) [45], up to 18 as in the case of H-TEC SYSTEMS [46], with its Hydrogen Cube System (HCS) equipped with S450 PEM stacks (rated input power of ~ 125 kW, ~ 26 Nm³/h hydrogen production capacity and cell surface area of 450 cm² [47]). Each device (HCS) is able to produce 2 MW. Other examples come from Hydrogenics, like the HyLYZER[®] - 1000 (Figure 3.1) or 500, each composed of 2 stacks, operating at 30 bar (cathode side) and with a nominal input-power of 5 and 2.5 MW respectively [48]. Among the electrolysers presented by Plug, the EX-2125D could fit a wind turbine with its 5 MW input nominal load. It works with 40 bar of pressure at the electrodes and has a water consumption of 13 L/kg_{H₂} [49]. The EL600N from H2B2 could also be a nice reference. It is composed by 3 stacks with a maximum nominal hydrogen production of 600 Nm³_{H₂}/h (1,290 kg_{H₂}/day) [50]. Table 3.1 summarises some specifications of the mentioned electrolysers.

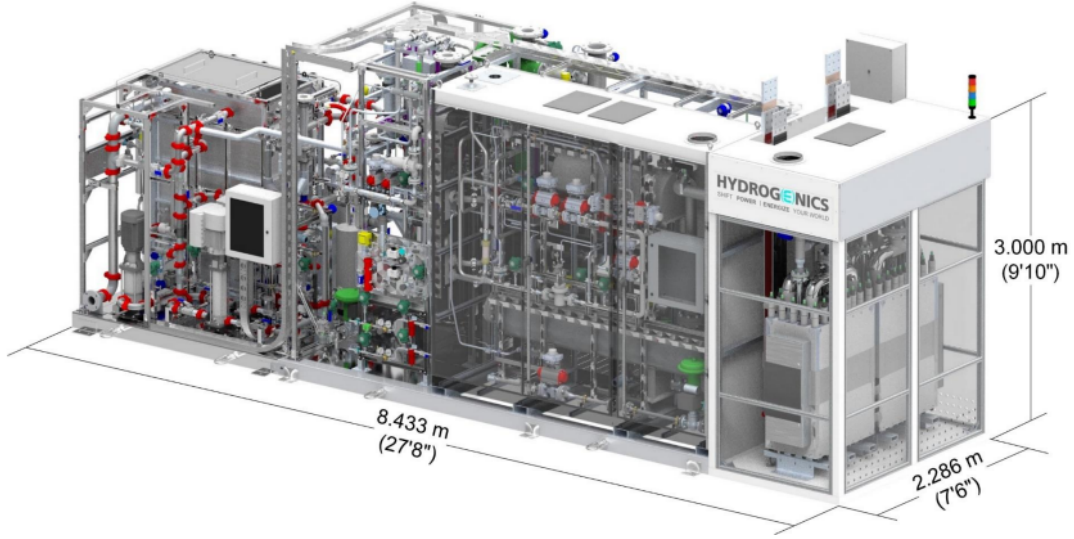


Figure 3.1. HyLYZER[®] - 1000 by Hydrogenics - 5 MW nominal input power [48]

Company	ITM	H-TEC	Hydrogenics	Plug	H2B2
Nominal input power (MW)	5	2	5	5	3.1
Nominal hydrogen flow (Nm ³ /h)	~ 1000	~ 420	1000	1000	600
H ₂ output pressure (barg)	30	15 – 30	30	40	15 – 40
Number of stacks	2	18	2	n/a	3

Table 3.1. Electrolysers' specifications

In this case study, the design parameters that characterise the single stack, like the active surface area of 290 cm², the membrane/electrodes thickness of 0.0178 and 0.0215 cm respectively, the 60 cells connected in series, are taken from the work of Espinosa-López et al. [18] based on the 46 kW PEM water electrolyser, installed on the MYRTE platform located on the Corsica Island, France. In fact, the electrolyser validation described in Section 4.1 has been conducted using the experimental results from Espinosa-López et al. [18] paper, hence the will to design the stack based on their parameters.

As regards the sensitivity analyses (Section 4.2), the number of electrolysers connected in parallel were increased, while the number of cells and the active surface area were left unchanged, preventing any alteration to the model. Generally, the most powerful electrolysers (order of MW) have big surface areas, like 1,250 cm² (future plans are to increase it to 3,000 cm²) [51] and a variable number of stacks that, as already presented in Table 3.1, ranges from 2 to 18, with typical values

in the range between 2 and 4. To limit the input current density below 3 A/cm^2 , so to comply to the assumptions (see Hypotheses in Section 2.1), a number of 60 stacks will be connected in parallel for the wind turbine case, while a number of 30 for the spar buoy case (being the input power smaller). In this way, all the power produced by the power turbine and the spar buoy will be consumed in their full operating range avoiding to exceed the 3 A/cm^2 . As will be highlighted in Section 3.2 and Section 3.3, the power signals differ for the peak/mean power ratios, leading to a better power exploitation generated from the wind turbine compared to the spar buoy. In fact, the electrolysis system connected to the offshore wind turbine (60 stacks in parallel) will work close to its nominal power load, unlike for the one connected to the spar buoy (30 stacks in parallel), which, in order to comply to the assumptions, will be oversized. In fact, a better exploitation of the electrolysis system, connected to the spar buoy, would be obtained by reducing the number of stacks in parallel, but this would require the implementation of the activation over-voltage in the electrochemical submodel, which has been neglected (see Hypotheses in Section 2.1).

3.2 Offshore wind turbine

The power production of a 5 MW floating offshore wind turbine is here analysed. Subsection 2.2.1 already mentioned how the system has been developed and how the wind resource has been computed, so the primary purpose of this section is to focus on the results coming from the wind turbine modelling.

Three cases have been considered:

1. $H_w = 0.8 \text{ m}$, $T_w = 7.0 \text{ s}$, $U_w = 8.0 \text{ mps}$

In relatively calm-wind conditions, the wind velocity is not excessive and so

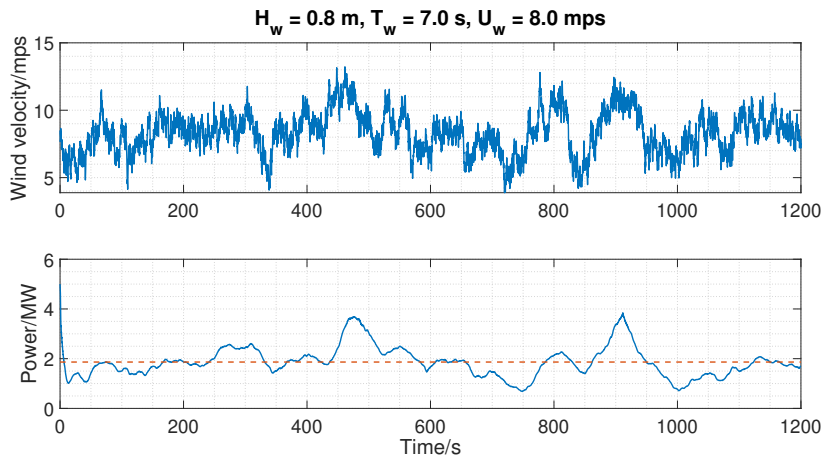


Figure 3.2. 1.865 MW average power produced in 20 minutes

is the output power. The dynamic involved is relatively smooth compared to the other two examples presented below, in which the wind velocity is larger.

2. $H_w = 2.5$ m, $T_w = 9.0$ s, $U_w = 12.0$ mps¹

The wind starts to blow with a larger force, leading to a larger power production.

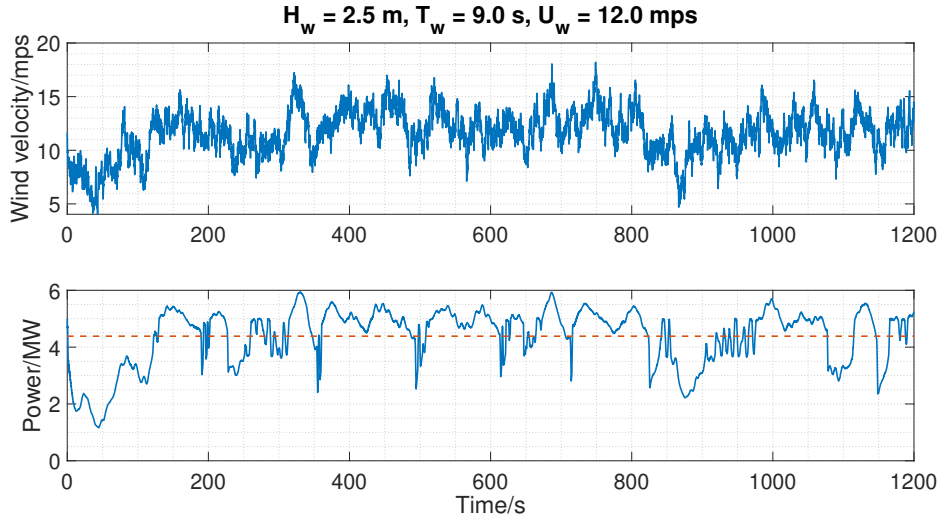


Figure 3.3. 4.385 MW average power produced in 20 minutes

As it is possible to notice the dynamic of the system is different from the first case, in fact more peaks are appreciable.

3. $H_w = 3.0$ m, $T_w = 11.0$ s, $U_w = 22.0$ mps

This is a limit condition in which the wind turbine operates at its maximum power, nearly to the shutdown for safety reasons. This is clearly the most stressing condition in terms of forces acting on the wind turbine (Figure 3.4).

The selection of the input power in the sensitivity analysis (see Section 4.2), is based on the dynamic of the signal. The second case presented above, i.e. $H_w = 2.5$ m, $T_w = 9.0$ s, $U_w = 12.0$ mps (Figure 3.3), has been selected to power the model due to its large peak/mean power ratio and the acceptable power production. A simulation time of twenty minutes provides reasonable results for the purposes of the case study (see Chapter 4).

¹ H_w = Significant Wave Height, T_w = Peak Wave Period, U_w = Average Wind Speed

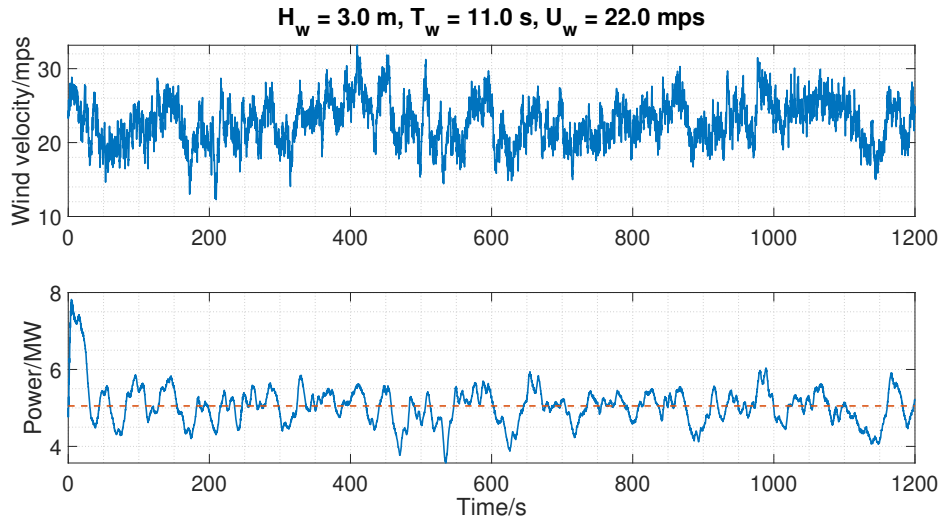


Figure 3.4. 5.052 MW average power produced in 20 minutes

3.3 Wave energy converter

The power production signals of a spar buoy are here analysed. Subsection 2.2.2 already mentioned how the system has been developed and how the wind resource has been computed, so the primary purpose of this section is to focus on the results coming from the spar buoy modelling.

Three cases have been computed:

1. Low-energetic: $H_s = 1.5 \text{ m}$, $T_p = 7 \text{ s}$ ²

This represents the calmest case, where the power production is really low, around 14.7 kW on average (Figure 3.5). However, it is already possible to note the large variability of the signal, with its evident differences with the wind turbine case (Section 3.2). In fact, the power oscillates reaching often close to zero energy production, due to the inherent oscillatory behaviour of ocean waves, which is translated to the working principle of the spar buoy oscillating water column technology.

2. Medium-energetic: $H_s = 2.5 \text{ m}$, $T_p = 8 \text{ s}$

The power starts to rise a little more compared to the first case, even if it remains still pretty low, averaging 32.9 kW in the simulation window (Figure 3.6). This case shows more evident fluctuations and larger power peaks.

² H_s = Significant Wave Height, T_p = Peak Wave Period.

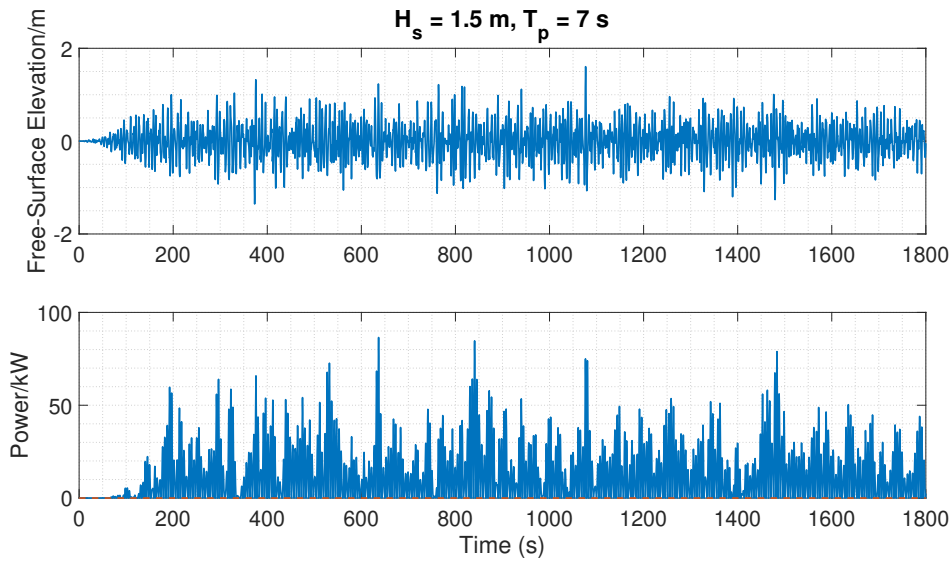


Figure 3.5. 14.7 kW average power produced in 30 minutes

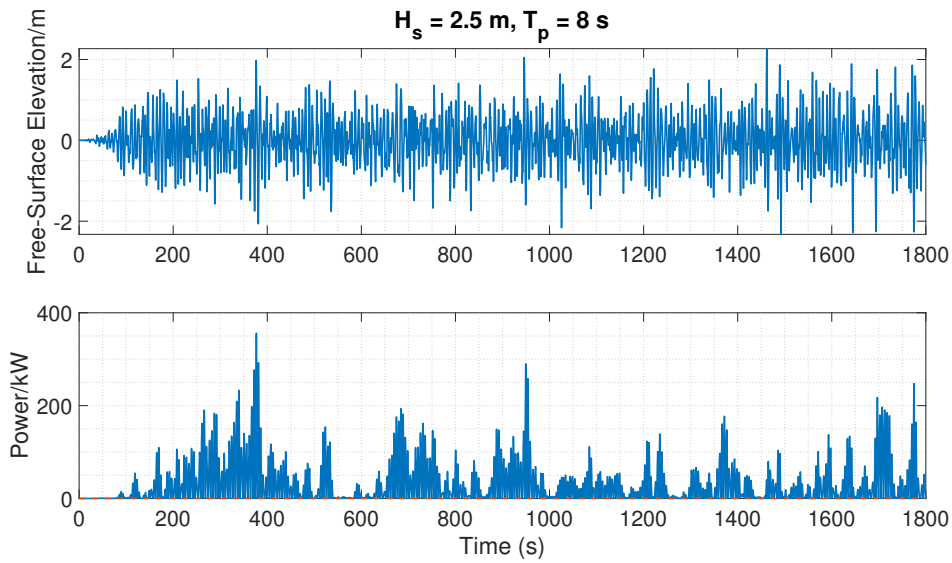


Figure 3.6. 32.9 kW average power produced in 30 minutes

3. High-energetic: $H_s = 4 \text{ m}, T_p = 12 \text{ s}$

Due to extreme environmental conditions, this results to be the most powerful case, with an average of around 246 kW and peaks up to 3 MW (Figure 3.7). The recorded fluctuations are particularly extreme, qualitatively comparable to the second case (Figure 3.6).

The last case (Figure 3.7) will be employed in the sensitivity analyses due to the

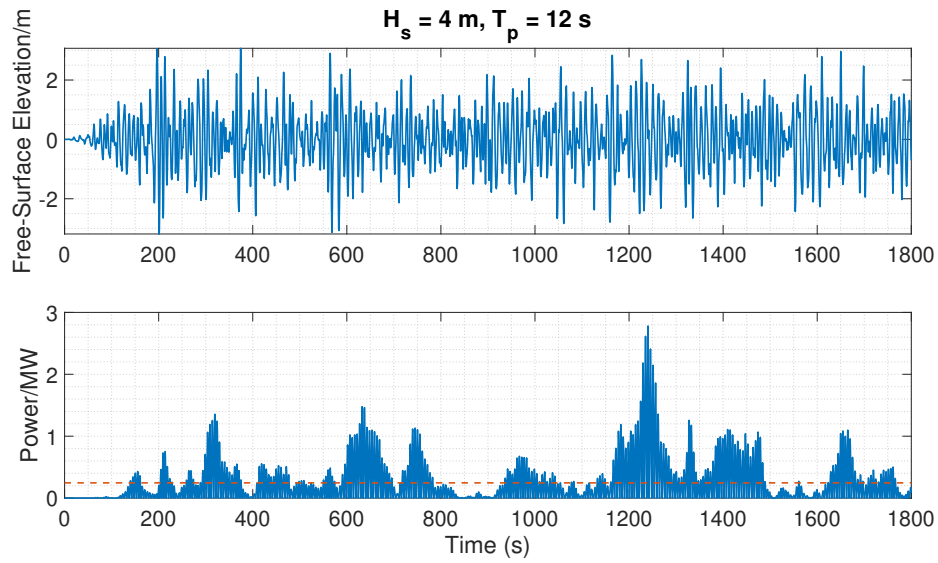


Figure 3.7. 245.9 kW average power produced in 30 minutes

high power produced and the good dynamic associated (high peak/mean power ratio). A simulation time of thirty minutes provides reasonable results for the purposes of the case study (see Chapter 4).

Chapter 4

Results

In the following chapter, the purposes to carry out are:

1. **Model validation**, i.e. the task of ensuring the compatibility between the results provided by the computational model and the experimental data.
2. **Sensitivity analysis**, being the purpose of the Thesis the evaluation of the dependence of hydrogen productivity and other aspects, such as the heat generation within the electrolysers and the energy/water consumption, from several thermodynamic variables.

In the model validation section, both the stationary and transient operations will be analysed and validated, showing at the same time the influence that the coolant has on the device operation.

In the sensitivity analysis, three input parameters, that are pressure, temperature and power, will be changed to record the associated variations.

4.1 Model validation

In this section, the model results and a comparison with experimental data will be discussed.

The model was implemented considering the parameters presented in the work of Espinosa-López et al. [18], as regards the electrochemical and the thermal submodel. The thermal submodel (Subsection 2.1.3) was developed furthermore introducing a more detailed explanation about the auxiliary cooling, i.e. the heat exchanger. In addition, a mass transport submodel was implemented, useful to investigate the water mass transfers across the stack, hence the water circulation in the first loop (see Section 2.1 for more details). In addition, heat fluxes, such as the auxiliary cooling and the pump heat, or the molar concentrations inside the stack, can be estimated starting from the results produced by the mass transport submodel.

Figure A.1 reports the model implementation in the Simulink[®] environment. Starting from the top the anode, membrane and cathode submodel interconnections are presented, followed at the bottom by the electrochemical, thermal and specifications submodels.

Firstly, the system has been tested to evaluate the polarization curve, assuming an anode and cathode pressure of 35 bar and 36 bar respectively (according to Espinosa-López et al. [18], the pressure gradient across the stack is one bar) and a fixed stack temperature of 50 °C. Figure 4.1 reports the comparison between the polarization curve and the experimental data.

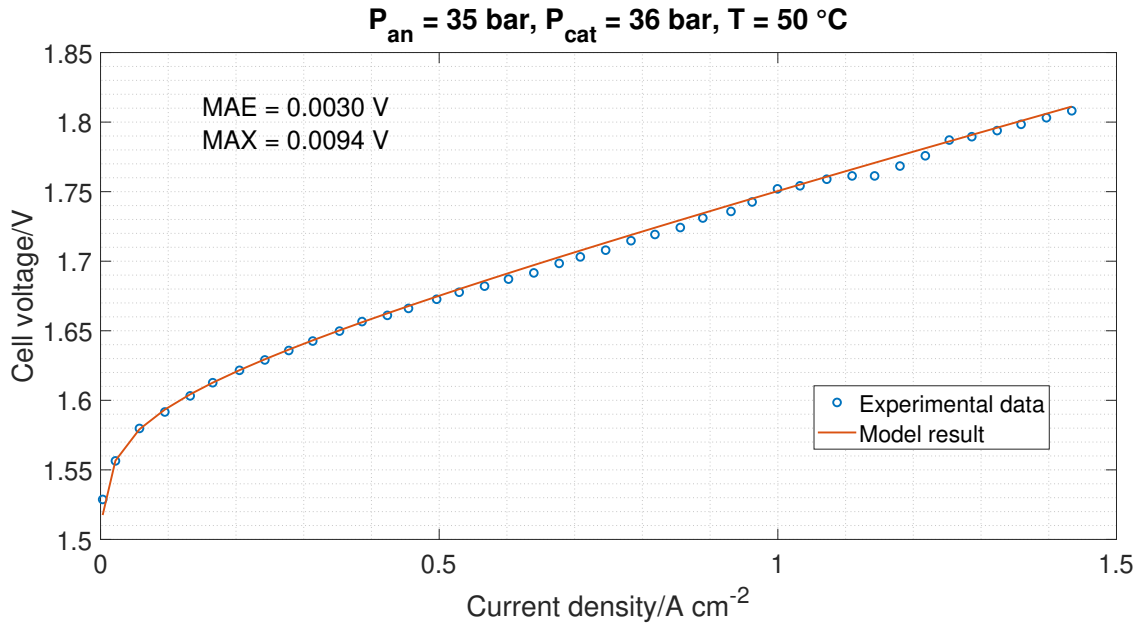


Figure 4.1. Polarization curve vs experimental evidence

The model simulates in an acceptable way the experimental trend (blue dotted line) as Figure 4.1 reports. In fact, the small appreciable fluctuations in the top right corner of the graph are presumably due to stochastic and unavoidable errors of the measuring instruments. The deviations, i.e. the **mean absolute error** MAE and the **maximum absolute error** MAX, can be calculated in the following way:

$$MAE = \frac{\sum_{i=1}^n |y_i - x_i|}{n} \quad \text{and} \quad MAX = \max(|y_i - x_i|), \quad (4.1)$$

where y_i is the the model prediction, x_i the experimental result and n the number of experimental points.

Besides the polarization curve, the dynamic behaviour of the electrolyser can be verified. As usual, the experimental measurements of Espinosa-López et al. [18] were taken as reference, in particular, the electrolyser start-up phase with photovoltaic (PV) real load was evaluated. Figure 4.2 reports the result of the dynamic simulation.

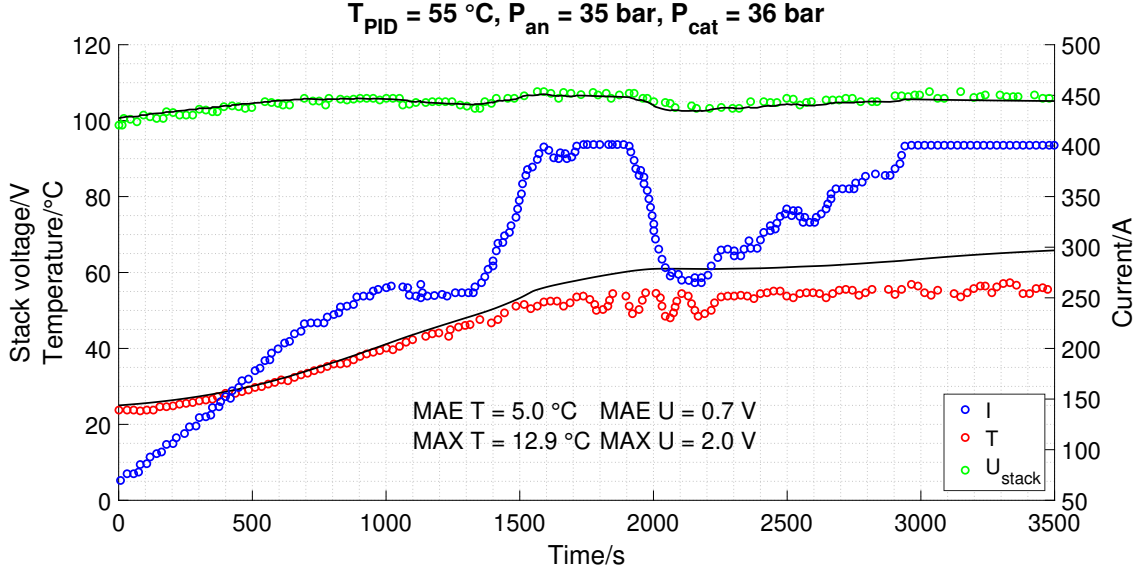


Figure 4.2. PEM water electrolyser validation with PV real load. Continuous lines represent model simulation, dotted lines represent experimental measurements

The predicted stack voltage is largely compatible with the experimental results, while a lower degree of accuracy is observed for the temperature. As previously mentioned, the auxiliary cooling system is part of the thermal submodel 2.1.3.3 developed in this document. In particular, it has been implemented through the ϵ -NTU method which identifies a maximum limit on the amount of exchangeable heat, called $\Phi_{cooling}^{max}$ (Equation 2.74), function of the difference between the water and refrigerant temperature entering the heat exchanger and on the minimum between the heat capacity rates. It follows that the maximum heat transfer can be increased only acting on the temperature gradient between the inlet temperatures. In fact, the mass flow rate in the first loop is determined by Equation 2.70, while a consistent increase of the mass flow rate in the second loop would not have effect, according to $\Phi_{cooling}^{max}$ definition. The employed refrigerant, for sake of simplicity and due to the lack of more detailed information, is water at 10 °C, which, is shown to be insufficient to assure enough cooling potential to the stack, as Figure 4.2 reports. To prove this, a different refrigerant, i.e. water with 50% glycol (in terms of volume), with an inlet temperature of 246.15 K (freezing point: 236.35 K, $c_p =$

3400 J/kg/K), has been employed in the dynamic simulation.

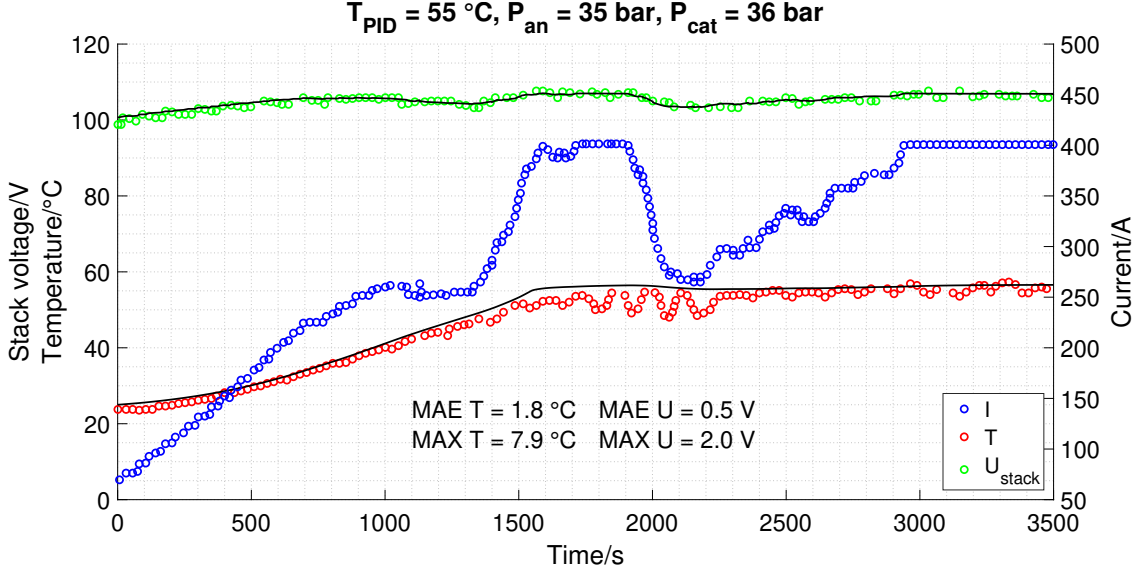


Figure 4.3. PEM water electrolyser validation with PV real load @ Refrigerant: 50/50 water + glycol

Figure 4.3 reports the results of the new configuration where the imposed temperature T_{PID} of 55 °C is respected, and, as a consequence, the stack voltage results to match even more the experimental results (both mean absolute error and maximum absolute error decrease). However, in the next analyses, for sake of simplicity, water will still be employed as refrigerant (at 10 °C), paying attention not to get close to 100 °C to avoid boiling of water.

The measured temperature fluctuations (red dotted line in Figure 4.2 and 4.3) are caused by water recovery from hydrogen separator (colder than the average first loop temperature) and the periodically injection back in the first loop (anode side), as explained by Espinosa-López et al. [18]. The model cannot simulate this type of temperature evolution being the temperature uniformity one of the assumptions.

4.2 Sensitivity analyses

The sensitivity analysis is divided into two parts, the first regards the wind turbine operation, while the second one the wave energy converter. The simulations will be carried out for each part, first with average power as input, then with the instantaneous one. The target of the analysis is the system response to the two thermodynamic variables variation, i.e. pressure and temperature, in terms

of hydrogen production (kmol), energy consumption EC (Wh/mol) and heat flux generation Φ_{heat} (kW or MW). Water consumption evaluation is explicitly omitted being equal to the amount of hydrogen produced, according to Equation 2.33 and Equation 2.37.

Regarding the sensitivity analyses with respect to pressure, the variables like the outdoor, PID and refrigerant temperature will be fixed at 298.15 K, 338.15 K and 283.15 K respectively (in the spar buoy analyses there will be some changes). Subsequently, in the sensitivity analysis with respect to temperature, the anode and cathode pressures will be fixed at 1 bar (in the spar buoy analyses there will be some changes), and one temperature at a time will be changed, while keeping the other two constant, and so on for all three temperatures.

4.2.1 Offshore wind turbine - Average power

In this subsection, the stationary operation of a 5 MW nominal power wind turbine over a time window of 1200 seconds will be analysed. In particular, the second system presented in Subsection 3.2 (Figure 3.3) is considered with its 4.385 MW produced average power.

4.2.1.1 Sensitivity analysis - Pressure

The pressure sensitivity analysis produced the results depicted in Figure 4.4. Starting from the hydrogen generation, the maximum corresponds to low anode and cathode pressures. The results are in accordance with the **Chatelier-Braun's Principle**, which states that the reaction equilibrium shifts to a new one able to counteract the effect of pressure, temperature, concentration or volume variation. Focusing at pressure, the following general law can be defined:

1. If pressure increases, the side of the equilibrium with fewer moles is more favorable.
2. If pressure decreases, the side of the equilibrium with higher moles is more favorable.

According to Equation 1.1, the number of moles of the products is greater than the reactants, hence by increasing the pressure at the anode/cathode the hydrogen production decreases as well as that of oxygen. The cathode pressure has greater influence on the voltage (which reflects on the productivity and energy consumption) probably due to the fact that it opposes the movement of the cations from the anode to the cathode, therefore making the process more difficult [23].

At the same time, by increasing the pressure, the open circuit voltage increases (Equation 2.15), and being the load (constant) applied to the electrolyser dependent on the product between current and voltage, current decreases, leading to a

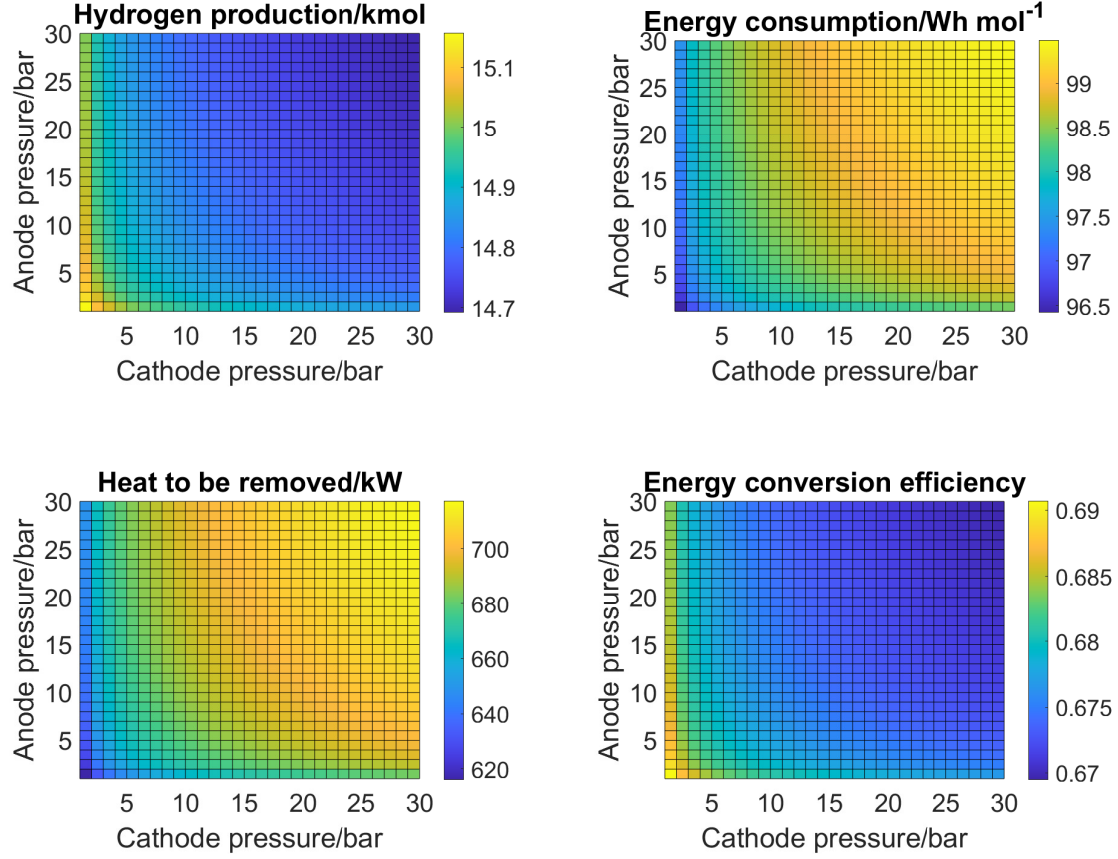


Figure 4.4. Sensitivity analysis with respect to pressure - P_{av}^{wind}

lower moles production, hence higher energy consumption (Equation 2.31 and 2.37).

The heat flux Φ_{heat} was computed as follows (see Subsection 2.1.3 for more details):

$$\Phi_{heat} = \Phi_{PEMWE} + \Phi_{pump} - \Phi_{loss} - \sum_{i=1}^N \dot{N}_i \Delta h_i. \quad (4.2)$$

To understand which contribution is more influent, each term was first computed at an anode and cathode pressure of 1 bar, than at 30 bar. The heat generation reported an increase of 16%, the mass transport heat of 10.5%, the heat losses to the environment 13.8% and the heat produced by the pump a decrease of 1.5%. Regarding the pump heat, the decrease is due to less hydrogen production which translates into less water consumption, so less amount of water flowing in the first loop. However, by simply looking at the relative increase of each term, it is not

appreciable which one has the largest influence. Figure 4.5 reports the weight of each term.

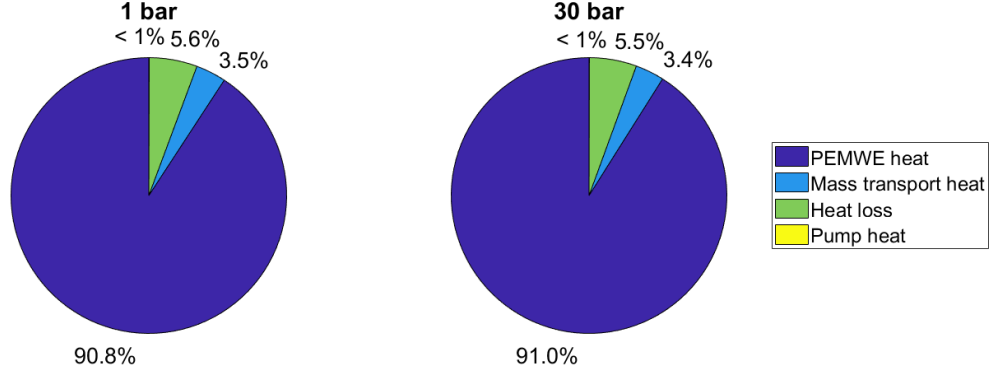


Figure 4.5. Percentage weight of each term over the heat to be removed - P_{av}^{wind}

The heat generation inside the stacks Φ_{PEMWE} has the greatest contribution over the net heat produced Φ_{heat} (Equation 4.2). It follows that an increase of Φ_{PEMWE} reflects in an overall larger heat to be removed. According to the heat generation definition (see Subsubsection 2.1.3.1 for more details), it is evident the strict dependence on voltage, in particular, when voltage increases (due to pressure), the heat produced by relative irreversibilities of transport processes rises.

In the end, by increasing the pressure at both anode and cathode, as a side effect, the hydrogen production decreases and the energy consumption increases, as well as the heat generation, that translates into more heat to remove. As a result, efficiency, computed in the following way, decreases:

$$\eta_{electr} = \frac{LHV_{H_2} \dot{N}_{H_2}}{(VI)_{stack}}. \quad (4.3)$$

But being $EC = (VI)_{stack} / \dot{N}_{H_2}$, it follows that:

$$\eta_{electr} = \frac{LHV_{H_2}}{EC}. \quad (4.4)$$

4.2.1.2 Sensitivity analysis - Temperature

Moving to the sensitivity analysis with respect with temperature, hydrogen production, energy consumption and heat to be removed variations to **outdoor temperature** were firstly analysed, increasing it from 298.15 K up to 313.15 K (25 - 40 °C) and fixing the anode and cathode pressure to 1 bar, while the PID and refrigerant temperature were set to 338.15 K and 283.15 K (65 °C and 10 °C) respectively. The analysis shows an increase in the hydrogen productivity (Figure 4.6), principally due to the higher temperature of injected water, favourable for reaction kinetics. As a consequence, energy consumption decreases, in fact, the higher the temperature, the lower the voltage (Equation 2.1), and so the lower the energy consumption. In fact, being the power at the electrolyser equal to VI (the power produced by the wind turbine here analysed is constant), if voltage V decreases, current I increases (as already seen in the pressure sensitivity analysis), which leads to higher H_2 , O_2 production and H_2O consumption (Equation 2.31, 2.33 and 2.37). This aspect will be repeated several times in subsequent analyses. There is no

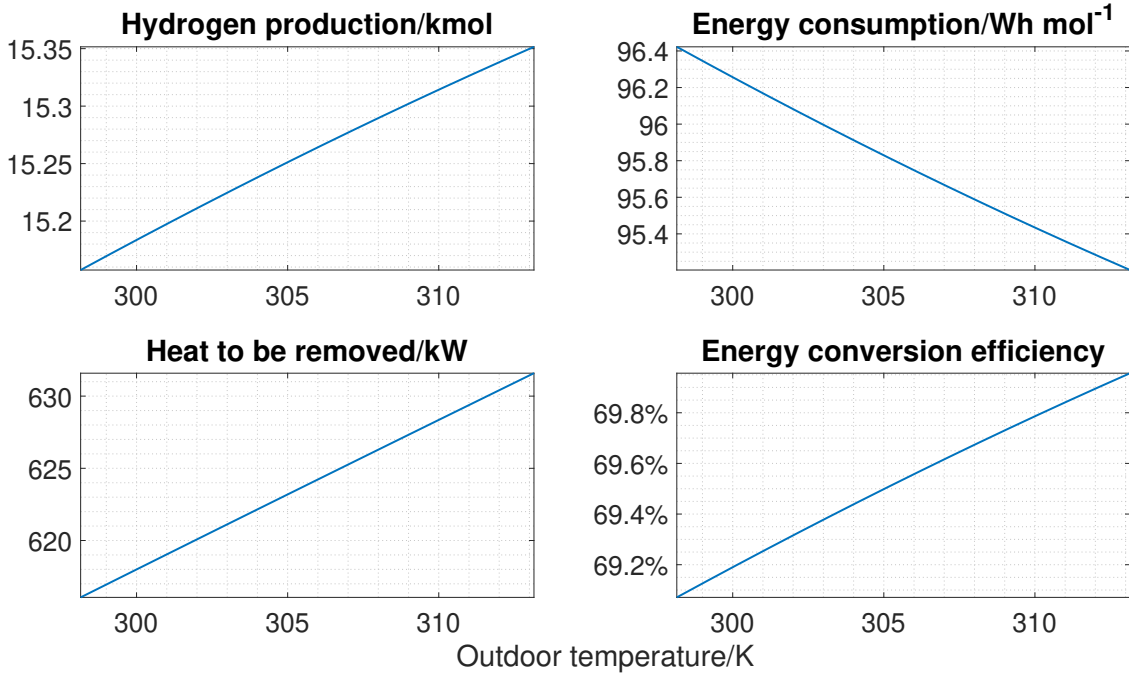


Figure 4.6. Sensitivity analysis with respect to outdoor temperature - P_{av}^{wind}

benefit considering the amount of heat to remove, that experiences an increase. The increase of the outdoor temperature leads to a lower heat exchange between the environment and the system, therefore to less heat losses (see Subsubsection 2.1.3.4), as well as less mass transport heat due to the higher injection temperature

of water. The temperature of each stack rises slightly making decrease the voltage, if compared to the base case (outdoor temperature of 25 °C), which translates into a lower heat generation due to irreversibilities. The only term of Q_{heat} (Equation 4.2) to experience an increase is the pump heat, which, however, is negligible (+39 mW). In the end, by summing all the contributes, the need to remove heat in excess increases slightly.

The temporal trend of both the heat and cooling flux (Equation 2.73) is analysed. In Figure 4.7, it is possible to note that, even if at higher outdoor temperatures the

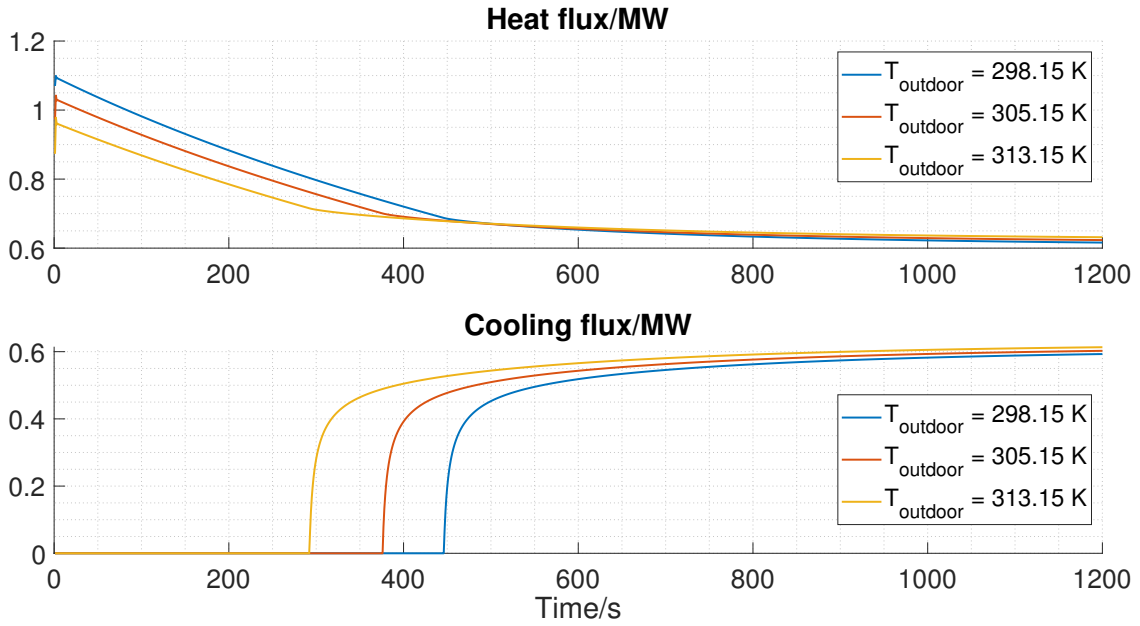


Figure 4.7. Heat and cooling flux temporal trend - P_{av}^{wind}

heat flux is initially smaller, the exchanger is activated in advance by the PID controller to limit the temperature of the stack below the PID temperature. The heat flux recorded in the activation moment, compared between three different outdoor temperatures, decreases with decreasing temperature, leading to an overall less heat to be removed in the stationary operation for decreasing outdoor temperatures. The efficiency, in accordance with Equation 4.4 and the energy consumption trend, has an increasing trend.

In the sensitivity analysis with respect to **PID temperature**, the anode and cathode pressure is set equal to 1 bar, while the outdoor and refrigerant temperature respectively to 298.15 K and 283.15 K (25 °C and 10 °C). The PID temperature ranges from 308.15 K to 358.15 K, although the temperature inside the stacks will not be exactly the one imposed by the PID controller (Figure 4.9). In fact, as it was

presented in the previous section (see Section 4.1), the cooling system effectiveness is strictly dependent on the inlet temperature of the refrigerant and, being adopted water at 10 °C as refrigerant, it may happen that the heat exchanger, as designed in this case study, fails to meet the cooling demand required. As a results, the temperature inside the stacks will be often higher than T_{PID} .

The results are pretty trivial, in fact, by increasing the PID temperature, the system is allowed to work at higher temperatures, and, as it was already highlighted several times, this translates into faster kinetics, hence higher hydrogen production. For the same reason, the higher the PID temperature, the less stringent is the cooling demand and the lower the heat generation due to irreversibilities, leading to a lower heat removal demand. The energy consumption experiences also a decrease, as shown in Figure 4.8, due to the lower voltage favoured by higher temperatures. Figure 4.9 reports a focus on stacks temperature, refrigerant mass flow rate and

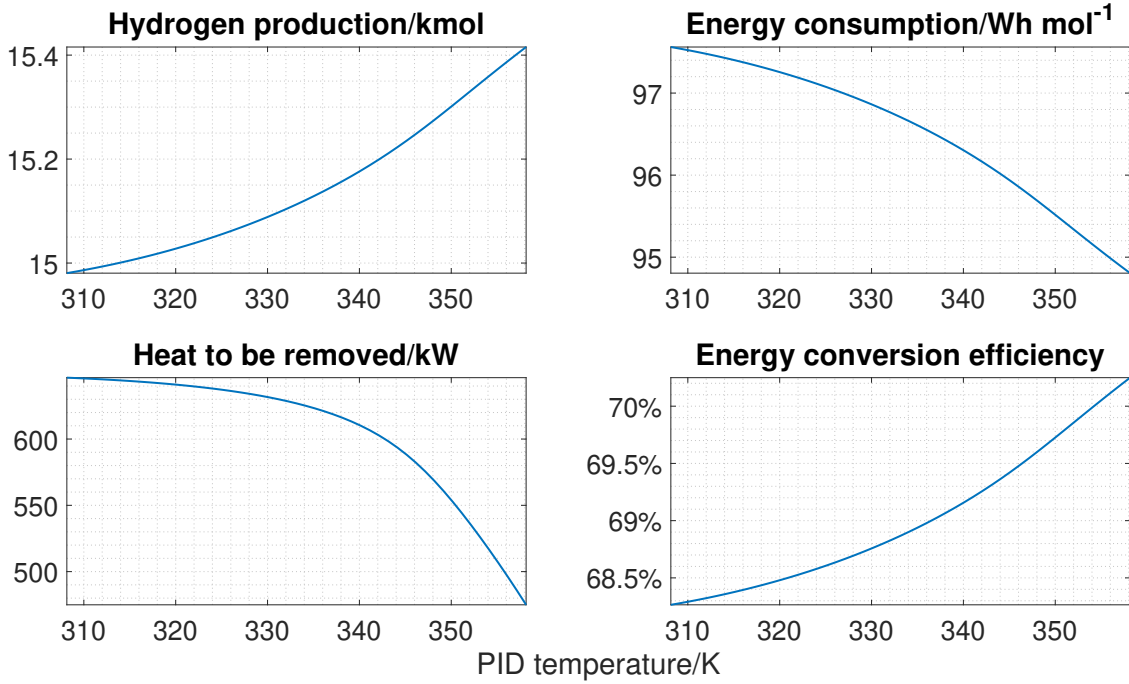


Figure 4.8. Sensitivity analysis with respect to PID temperature - P_{av}^{wind}

cooling flux. As it is possible to appreciate, even if the temperature set by the PID ranges from 308.15 K to 358.15 K, the temperature of the stacks results to be always higher until 348 K (see linear trend in Figure 4.9), besides which the cooling demand starts to be less stringent. It is also appreciable how, even for high level of mass flow rates of circulating refrigerant in the second loop, the PID controller is not able to effectively regulate the temperature of the whole electrolyser.

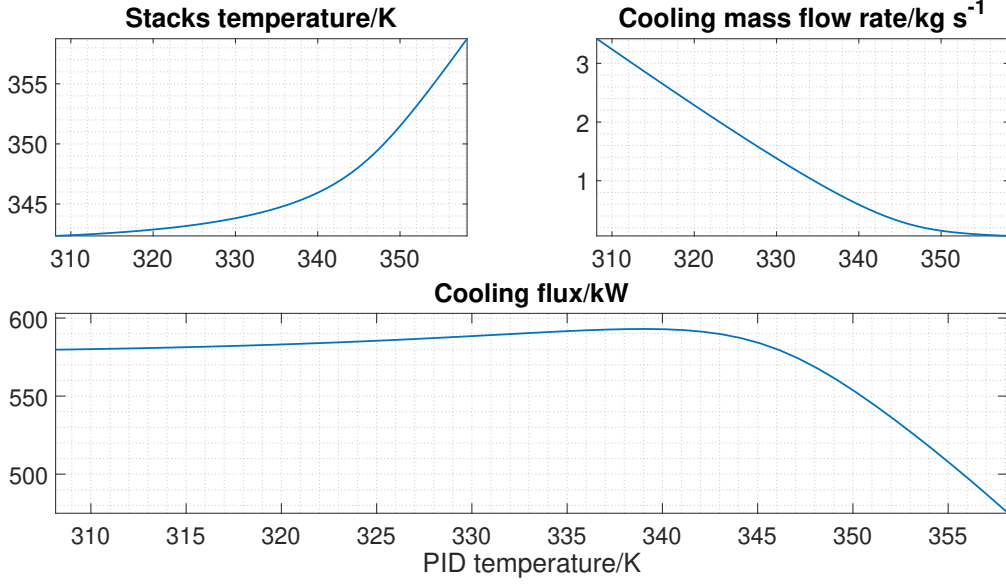


Figure 4.9. Focus on stacks temperature, cooling mass flow rate and cooling flux - P_{av}^{wind}

Finally, the discussion about the sensitivity analysis according to the **refrigerant temperature**. Anode and cathode pressure is set equal to 1 bar, while the outdoor and PID temperature, to 298.15 K and 338.15 K (25 °C and 65 °C) respectively, with the refrigerant temperature that ranges from 278.15 K to 298.15 K. The role of the refrigerant is to cool down the stack, which amount is controlled by the PID controller. By increasing the refrigerant temperature, the cooling potential decreases, as well as the maximum heat that can be removed, mainly dependent on the water and refrigerant temperature entering the heat exchanger. As a consequence, by reducing the refrigerant temperature, the stack temperature rises (Figure 4.11). Again, the higher the temperature, the higher the current (due to lower voltage), hence the higher the hydrogen production (Figure 4.10). The energy is consumed more efficiently with increasing temperature, leading to lower energy consumption per mole (Figure 4.10). As it is possible to note in Figure 4.11, the PID controller tries to compensate the loss of potential by increasing the coolant mass flow rate. The trend of the cooling flux is strictly dependent to the heat removal demand and by checking each contribution of Equation 4.2, they all remain pretty constant, except for the heat generation, that decrease from 696.9 kW ($T_{refr} = 278.15$ K) to 643.74 kW ($T_{refr} = 298.15$ K), as a consequence of the voltage reduction. The increase of the refrigerant temperature leads to a rise of stack temperature (PID controller does not succeed in keeping the stack temperature at T_{PID}), which, in turn, make decrease the voltage and so the heat generation. It follows that: the

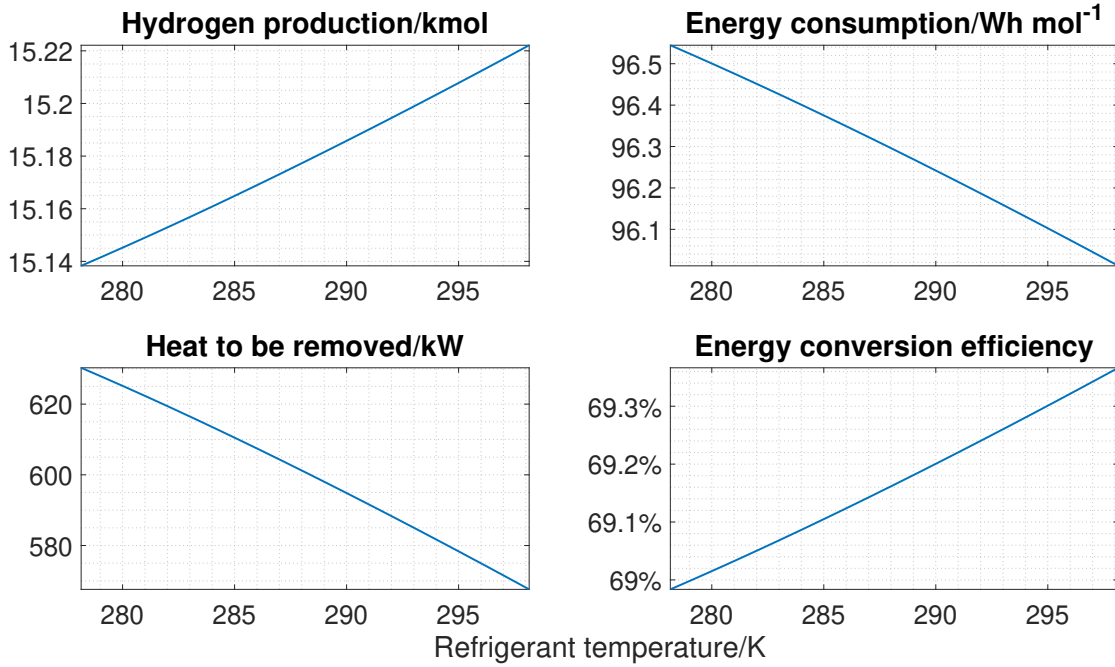


Figure 4.10. Sensitivity analysis with respect to refrigerant temperature - P_{av}^{wind}

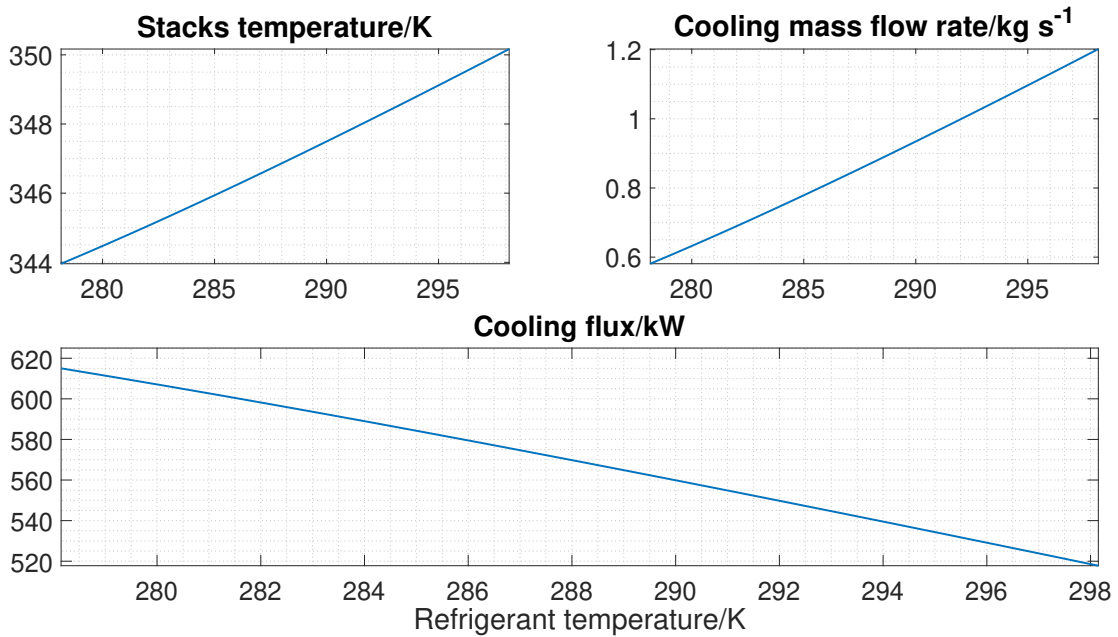


Figure 4.11. Focus on stacks temperature, cooling mass flow rate and cooling flux - T_{refr}

lower the heat generation, the lower the cooling demand.

4.2.2 Offshore wind turbine - Instantaneous power

After the sensitivity analyses with average input-power, the analysis with respect to the dynamic operation of a wind turbine was conducted. The second power signal, i.e. the one depicted in Figure 3.3, was simulated. The different trends of energy consumption and heat production were studied, and, when possible, comparison with the average power case were done. The simulations were carried out changing firstly pressure levels and then temperature ones.

4.2.2.1 Sensitivity analysis - Pressure

Starting from the sensitivity analysis with respect to pressure, the hydrogen production trend is perfectly in accordance with the average power case just studied, as depicted in Figure 4.12. In particular, a relative deviation from the average power case (see Subsubsection 4.2.1.1) of 0.38% is recorded, with a maximum of 0.41% situated at $P_{an} = 1$ bar and $P_{cat} = 1$ bar and a minimum of 0.37% at $P_{an} = 30$ bar and $P_{cat} = 30$ bar. Moving on the diagonal that connects the minimum to the maximum the relative deviation increases, as depicted below.

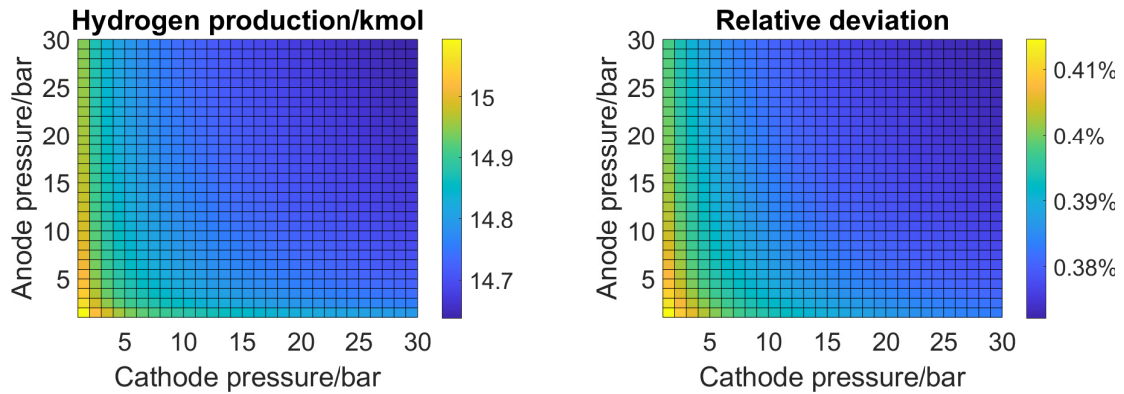


Figure 4.12. Hydrogen production trends with respect to pressure - P_{inst}^{wind}

It is possible to conclude that in this specific case, to assess ex post the hydrogen production, is not strictly necessary to know the instantaneous input power. The amount of hydrogen produced is in accordance with other electrolysers analysed (see Table 3.1), in fact, by converting kmol in kg ($1 \text{ kmol} = 2 \text{ kg}$) or Nm^3 ($1 \text{ kmol} = 22.4 \text{ Nm}^3$), it results $29.3 \text{ kg} - 30.2 \text{ kg}$ and $327.9 \text{ Nm}^3 - 338.2 \text{ Nm}^3$ of hydrogen in 20 minutes of wind turbine operation, depending on the pressure operation conditions. Carrying out an economic analysis, it might be more convenient to work at $P_{an} = 1$ bar and $P_{cat} = 30$ bar to store hydrogen already pressurised, although

production would drop slightly (0.3 kmol, or 0.6 kg/6.8 Nm³). In this way, the use of a compressor downstream of the plant could be avoided (some systems already work according to this concept).

Moving on with the analysis, some energy consumption trends with different input pressure have been studied, as reported in Figure 4.13. It is appreciable the energy

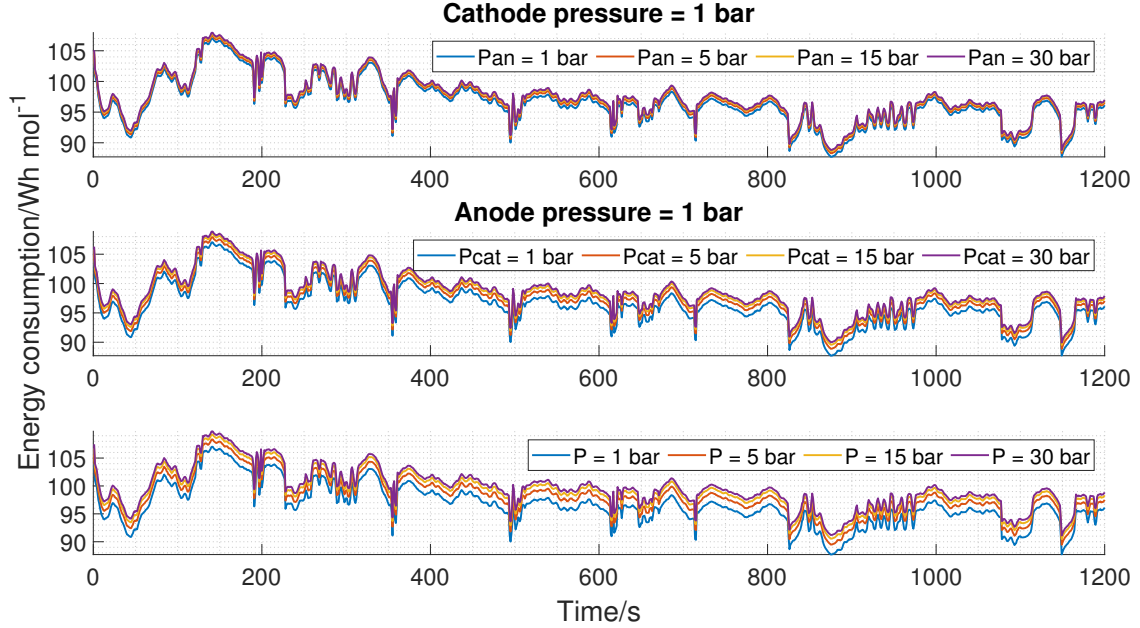


Figure 4.13. Energy consumption trends with respect to pressure - P_{inst}^{wind}

consumption trend similarity with the input power (Figure 3.3) and, in particular, how sudden peaks translate into an increase of the energy consumptions. Generally, it can be deduced that, a sudden request in the hydrogen generation produced by a quick increase of the input power, reflects on the energy consumption, leading to higher operational expenditure (OPEX). On the contrary, by applying a stationary load, as analysed in Subsubsection 4.2.1.1, the energy consumption naturally decreases due to the increase of temperature inside the stacks. This aspect is appreciable also in this case, in fact, after have reached a peak at around 150 seconds, the system begins to benefit of temperature rise influence, which stabilises after 600 s in a 345 K - 355 K range (Figure 4.14).

As already reported in Figure 4.4, the larger differences are noticeable moving along the diagonal, passing from 1 to 30 bar.

Figure 4.15 reports the heat flux trends with respect to pressure. For the sake of clarity, only the cases where anode and cathode pressures are equal have been represented, noting that the other two cases (P_{an} fixed/ P_{cat} variable and vice versa)

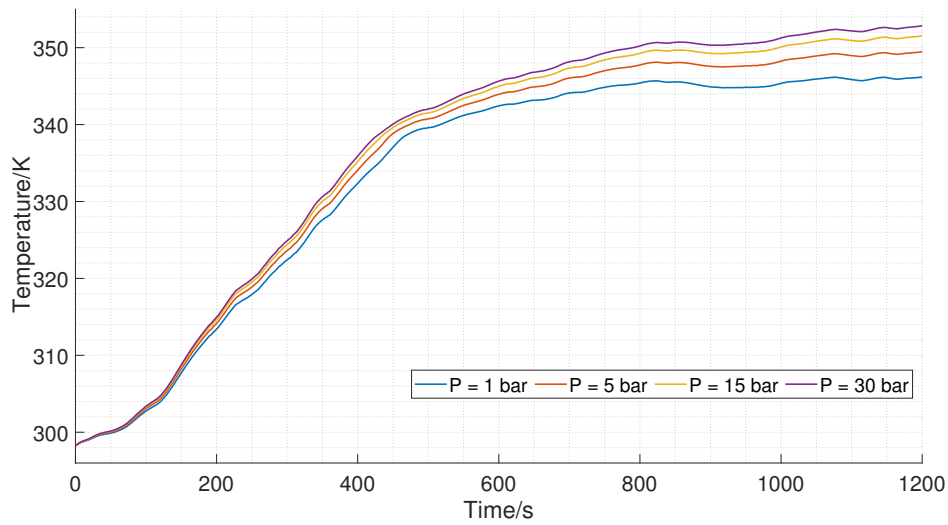


Figure 4.14. Temperature trends with respect to pressure - P_{inst}^{wind}

follows what already seen for the energy consumption, i.e. the curves come closer similarly. The fluctuations are larger with an intensity remarkable, in fact they ranges from a minimum of 147.4 kW - 182.9 kW to a maximum of 1.4 MW - 1.5 MW. Again, the choice to pressurise an electrode should be taken carefully due to the heat that must be disposed of not negligible. The trend is very variable and a large part comes from the contribution of the heat flux produced by irreversibilities inside the stacks, as Figure 4.16 reports.

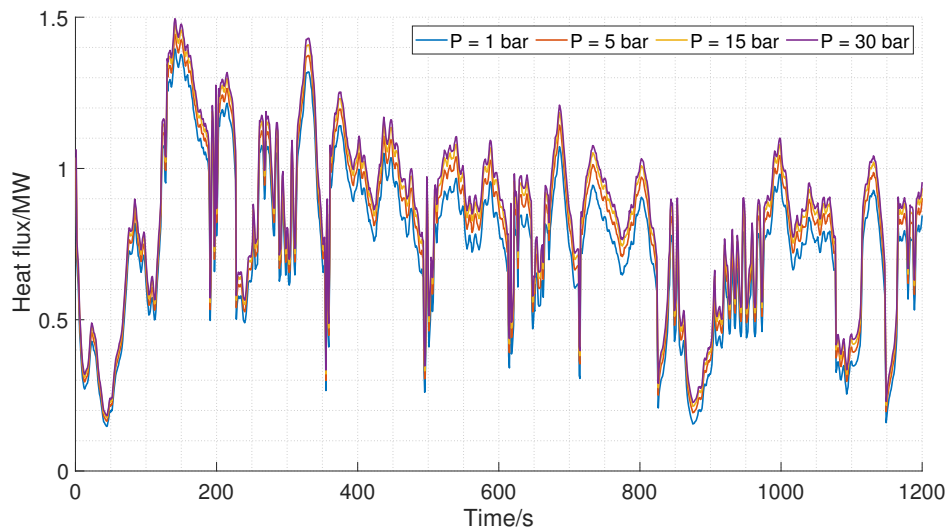


Figure 4.15. Heat flux trends with respect to pressure - P_{inst}^{wind}

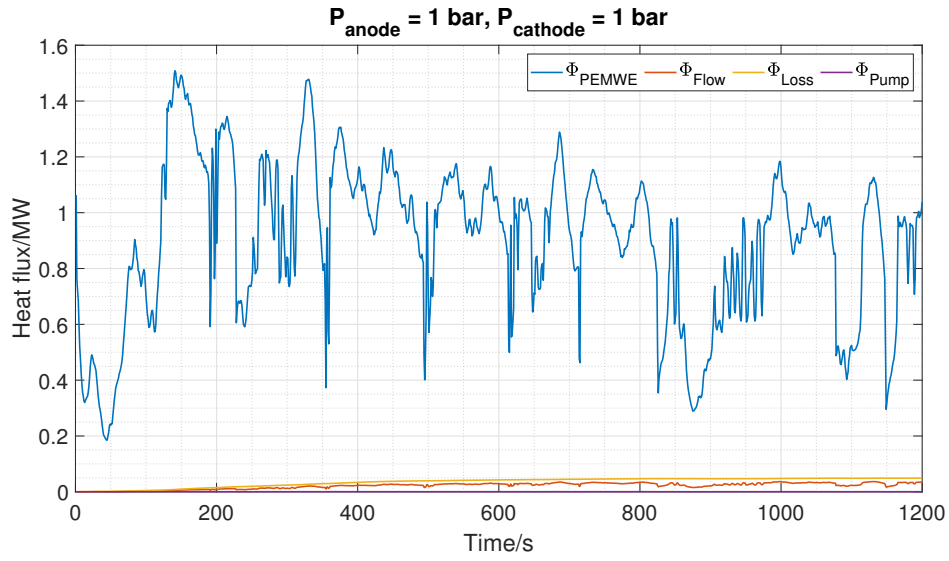


Figure 4.16. Contribute of heat fluxes - P_{inst}^{wind}

The heat flow in the legend stands for:

$$\Phi_{Flow} = \sum_{i=1}^N \dot{N}_i \Delta h_i. \quad (4.5)$$

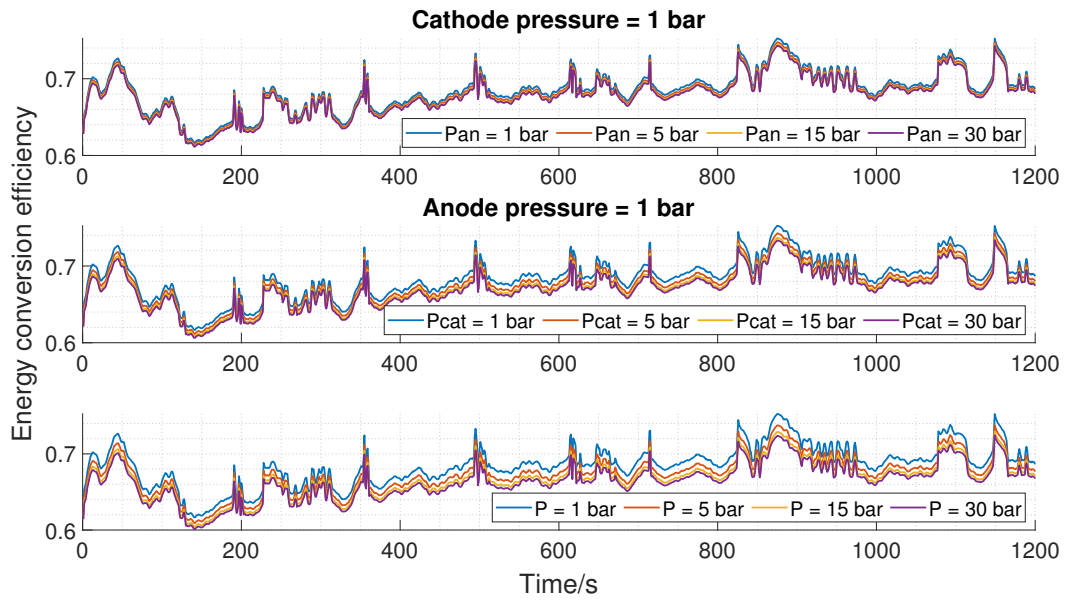


Figure 4.17. Efficiency trends with respect to pressure P_{inst}^{wind}

Figure 4.17 reports the energy conversion efficiency trends with respect to pressure. As already seen in Subsubsection 4.2.1.1 and 4.2.1.2, the efficiency is strictly dependent by the energy consumption, in particular it has an opposite behaviour: when energy consumption increases, efficiency decreases and vice versa, according to Equation 4.4. For this reason, in the following analyses, it will be omitted.

4.2.2.2 Sensitivity analysis - Temperature

Regarding the sensitivity analysis with respect to temperature, hydrogen production, energy consumption and heat flux trends with respect to **outdoor temperature** have been firstly analysed, increasing the outdoor temperature from 298.15 K up to 313.15 K (25 °C - 40 °C) and fixing the anode and cathode pressure to 1 bar, while the PID and refrigerant temperature to 338.15K and 283.15 K (65 °C and 10 °C) respectively. In the energy consumption and the heat flux analysis, for sake of clarity it has been omitted to report each curve.

Starting from the hydrogen production, the differences between the average input-power case (see Subsubsection 4.2.1.2) and the instantaneous here analysed have been studied and compared. As already noticed in the Subsubsection 4.2.2.1, the relative deviation is so small (Figure 4.18) that to assess ex post the hydrogen production it might be enough the average input-power produced. The growing

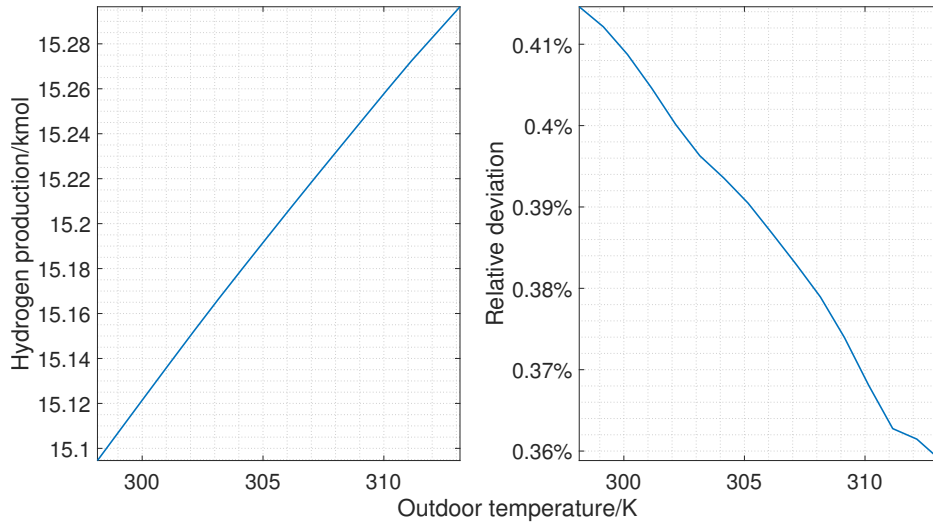


Figure 4.18. Hydrogen production trends with respect to outdoor temperature - P_{inst}^{wind}

trend reflects what previously seen regarding the parametric analysis with average input-power (see Subsubsection 4.2.1.2).

The energy consumption trends (Figure 4.19) show a greater sensitivity in the first phase in which outdoor temperature has a higher influence, while the general

decreasing trend is due to the rise of temperature inside the stack, that foster kinetics. Towards the end of the simulation, the differences between the curves are so small to be almost completely negligible, as previously highlighted in Subsubsection 4.2.1.2 with Figure 4.6. The heat flux behaviour is particular as well, in fact

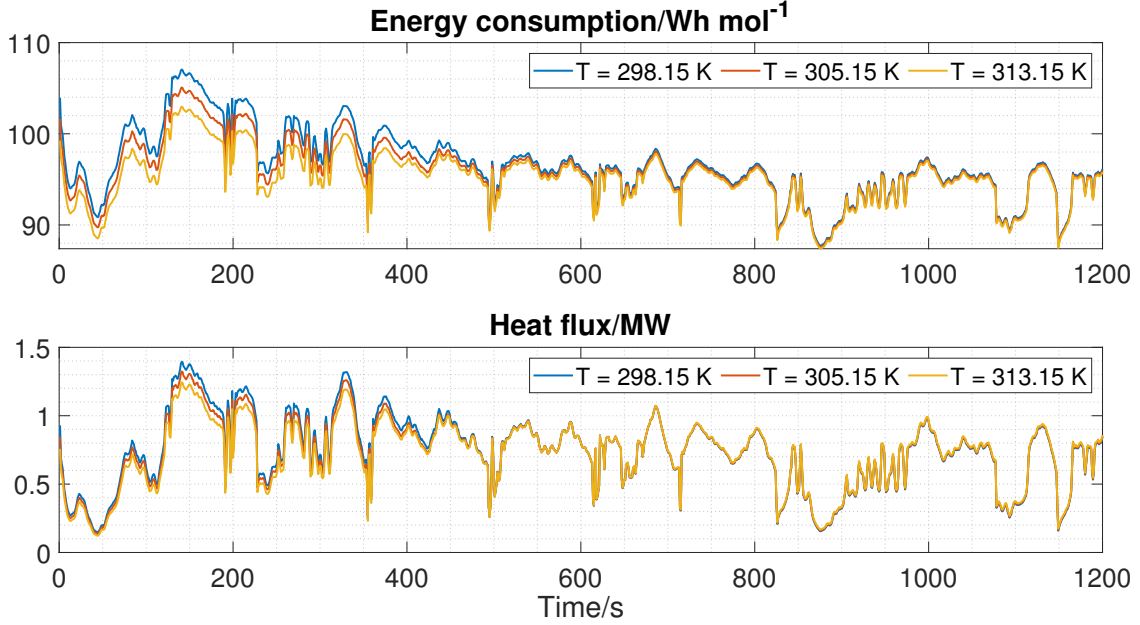


Figure 4.19. Energy consumption & heat flux trends with respect to outdoor temperature - P_{inst}^{wind}

it is initially smaller for increasing outdoor temperature, but then the relationship reverses (though it is not clearly appreciable without zooming), therefore becoming larger for higher outdoor temperature, as experienced in the average input-power case (see Subsubsection 4.2.1.2). In fact, this environmental boundary condition has a positive and negative effect. The heat flux (Equation 4.2) is initially lower for higher outdoor temperatures due to the temperature of injected water (equal to outdoor temperature) that foster kinetics (low voltage, low heat generation due to irreversibilities). However, due to the lower heat exchange between the environment and the system (see Subsubsection 2.1.3.4 for more details) and the lower mass transport heat (see Subsubsection 2.1.3.5 for more details), the temperature inside the stacks rises quickly, leading to an earlier activation of the heat exchanger. Comparing the amount of heat flux at the time of activation, it results larger for higher outdoor temperatures, which reflects on the amount of heat to remove, although slightly. Figure 4.7, which represents the case analysed with average input-power, may clarify the concept.

Moving to the sensitivity analysis with respect to temperature regulated by the PID controller (**PID temperature**), the anode and cathode pressures were set equal to 1 bar, while the outdoor and refrigerant temperature to 298.15 K and 283.15 K (25 °C and 10 °C) respectively. The PID temperature ranges from 308.15 K to 358.15 K. The hydrogen production follows what already seen previ-

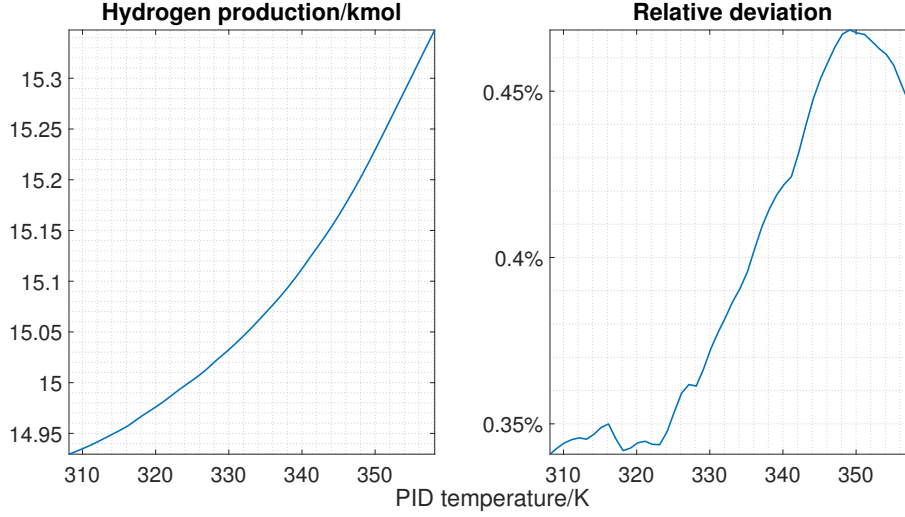


Figure 4.20. Hydrogen production trends with respect to PID temperature - P_{inst}^{wind}

ously regarding the deviation from the average input-power case: small enough to be negligible. The growing trend is the result of the rising temperature inside the stacks, in fact, by increasing the PID temperature, the system is allowed to work at higher temperature (that foster reaction kinetics), which does not reflect only on the hydrogen production but also on the energy consumption, which experiences a decrease (Figure 4.21). It is noteworthy that, although three equally spaced temperature trends have been depicted, the 308.15 K and 332.15 K curves are very close to one another. In fact, the PID controller is not able to effectively control the temperature due to the low performance of the heat exchanger (constraint on the adopted refrigerant fluid). The increase of the heat flux with decreasing PID temperature is a direct consequence of two effects: cooling demand less stringent, because the system is allowed to work at higher temperatures, and less heat generation due to lower voltage (favoured by high temperature). From this sensitivity analysis results that the higher the temperature at which the stacks operate, the higher the hydrogen production and the smaller the energy consumption and heat to remove.

Finally, the sensitivity analysis with respect to the **refrigerant temperature** can be discussed. Anode and cathode pressures have been set equal to 1 bar, while the outdoor and PID temperature equal to 298.15 K and 338.15 K (25 °C and 65 °C)

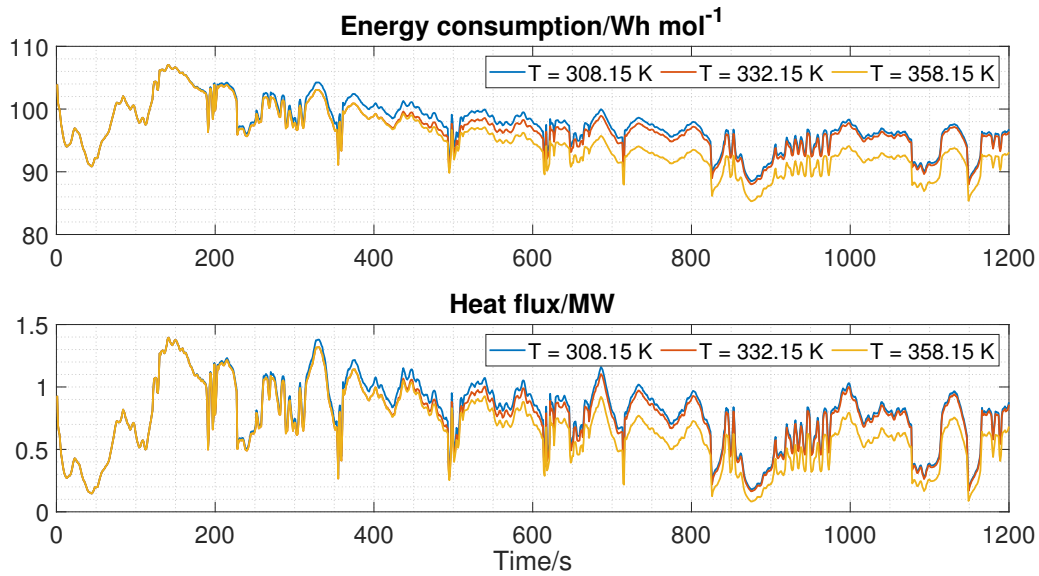


Figure 4.21. Energy consumption & heat flux trends with respect to PID temperature - P_{inst}^{wind}

respectively. The refrigerant temperature ranges from 278.15 K to 298.15 K (5 °C and 25 °C). Figure 4.22 reports the hydrogen production trend with respect to refrigerant temperature.

The approximation between the hydrogen production with constant input-power and instantaneous input-power case is acceptable. The relative deviation is in the range of 0.395% - 0.424%, therefore the hydrogen production can be evaluated with good precision starting from the average input-power, even if, it should be corroborated with other wind dynamic input-power analyses, such as the signals depicted in Figure 3.2 and 3.4. The hydrogen generation trends follow what already recorded for the constant input-power one (see Subsubsection 4.2.1.2), where it is appreciable how both the energy consumption and the heat to be removed decrease with increasing refrigerant temperature. By using a refrigerant at higher temperature, the cooling potential decreases, making the heat removal less effective, which leads to a rise of stacks temperature.

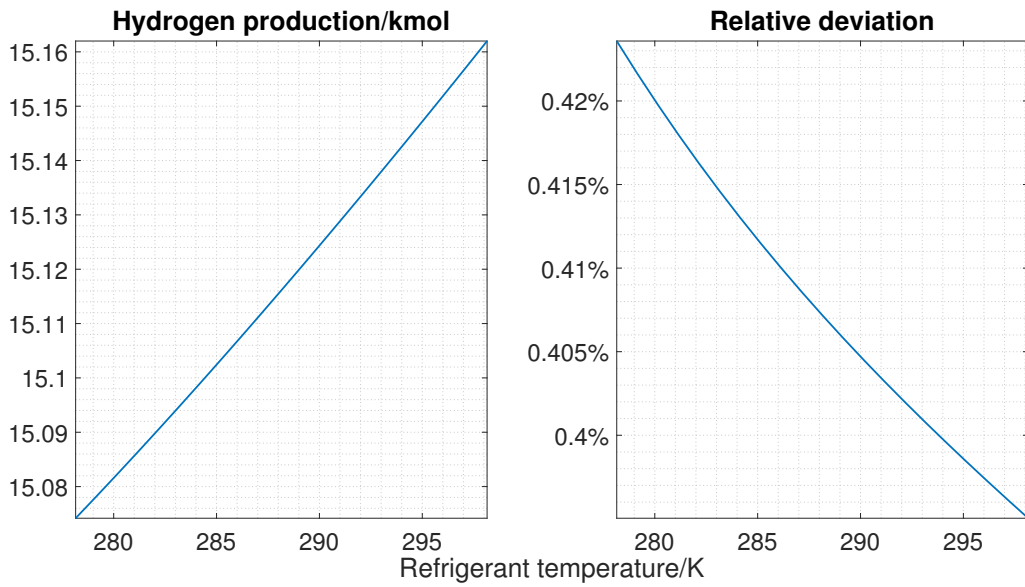


Figure 4.22. Hydrogen production trends with respect to refrigerant temperature - P_{inst}^{wind}

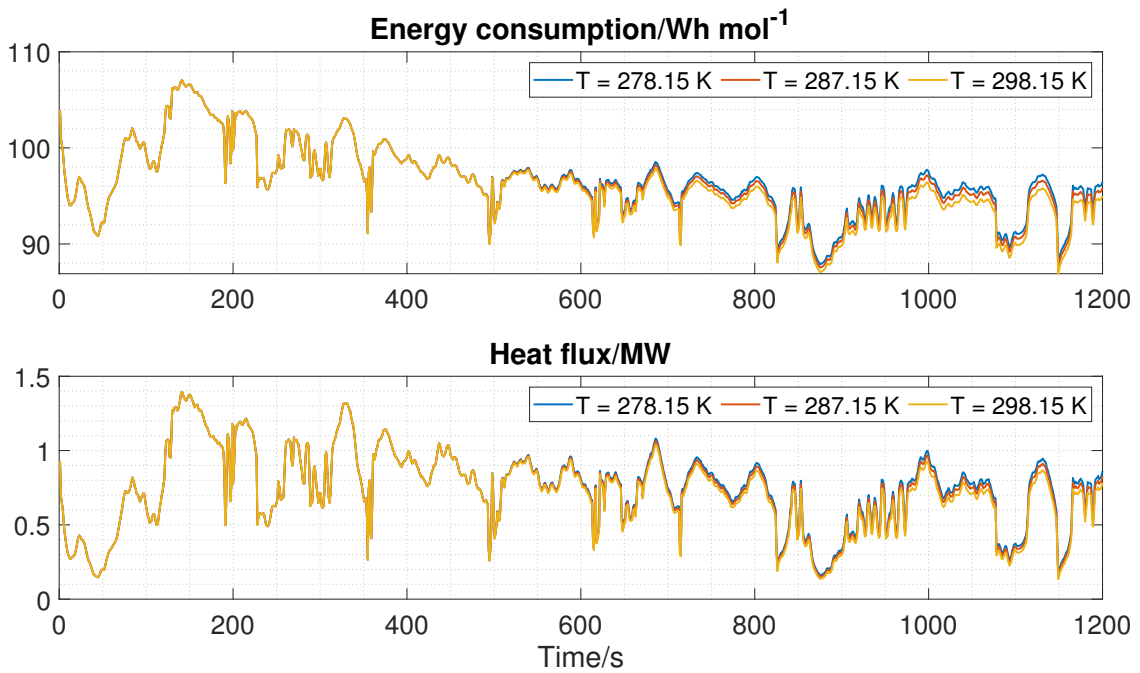


Figure 4.23. Energy consumption & heat flux trends with respect to refrigerant temperature - P_{inst}^{wind}

4.2.3 Spar buoy - Instantaneous power

In this subsection, the dynamic operation of a spar buoy will be analysed, particularly the third system depicted in Figure 3.7. The different trends of energy consumption and heat production will be studied as well, and, since the comparison with the average power case has already been made for the wind turbine case, that part will be omitted. In fact, the principle differences related to the different power source supplied to the electrolysers will be sufficiently highlighted already with the instantaneous input-power analyses.

The simulations are carried out changing firstly pressure levels and then temperature ones.

4.2.3.1 Sensitivity analysis - Pressure

The hydrogen production is the first parameter that was studied in the spar buoy sensitivity analysis with respect to pressure and, as Figure 4.24 reports, the H_2 mole production is lower compared to the wind turbine case (see Figure 4.12).

Even if the average power case will not be shown explicitly, as it has been done for the wind turbine (see Subsection 4.2.1), it was simulated and compared with the instantaneous input-power case. The hydrogen produced shows a larger difference, in particular an increase of around 35%. Therefore, on the contrary of what already seen so far, signals with huge peaks result to produce an amount of hydrogen which is not predictable, without introducing an error, starting from the information of average power, in apparent contrast with the wind power case (see Subsubsection 4.2.2.1).

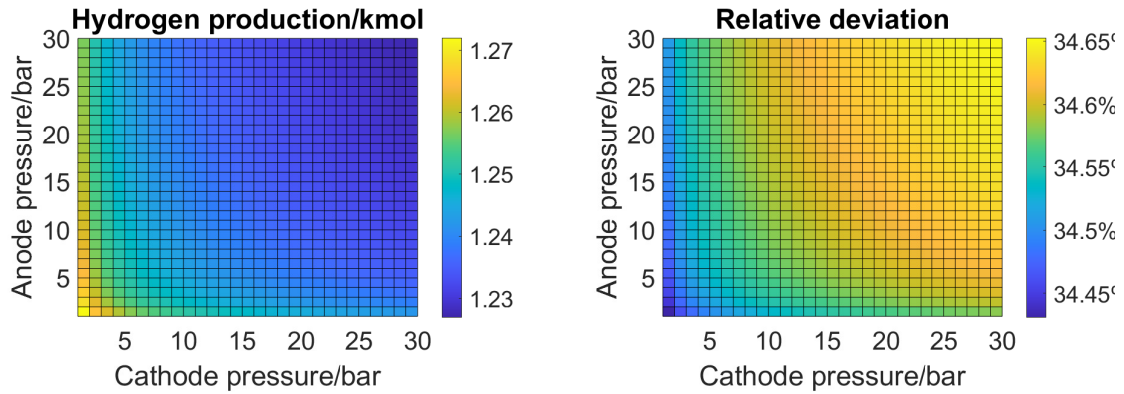


Figure 4.24. Hydrogen production trends with respect to pressure - P_{inst}^{wave}

Carrying out an economic analysis, it might be more convenient to work at $P_{an} = 1$ bar and $P_{cat} = 30$ bar to store hydrogen already pressurised, although production would drop really slightly (30 mol, or 60 g/0.672 Nm³), so as to store hydrogen

already pressurised, thus avoiding the use of a compressor downstream of the plant (some systems already work according with this concept).

Moving on with the analysis, some energy consumption trends with different input pressures ($P_{anode} = P_{cathode}$), as shown in Figure 4.25, have been studied, avoiding to report other cases for the sake of clarity. The behaviour with respect to other pressure levels are similar to the trends depicted in Figure 4.13. The same applies to efficiency trends in Figure 4.28.

The energy consumption relation to pressure has been already explained in the last subsections, especially in 4.2.1.1. Of interest is the influence that power

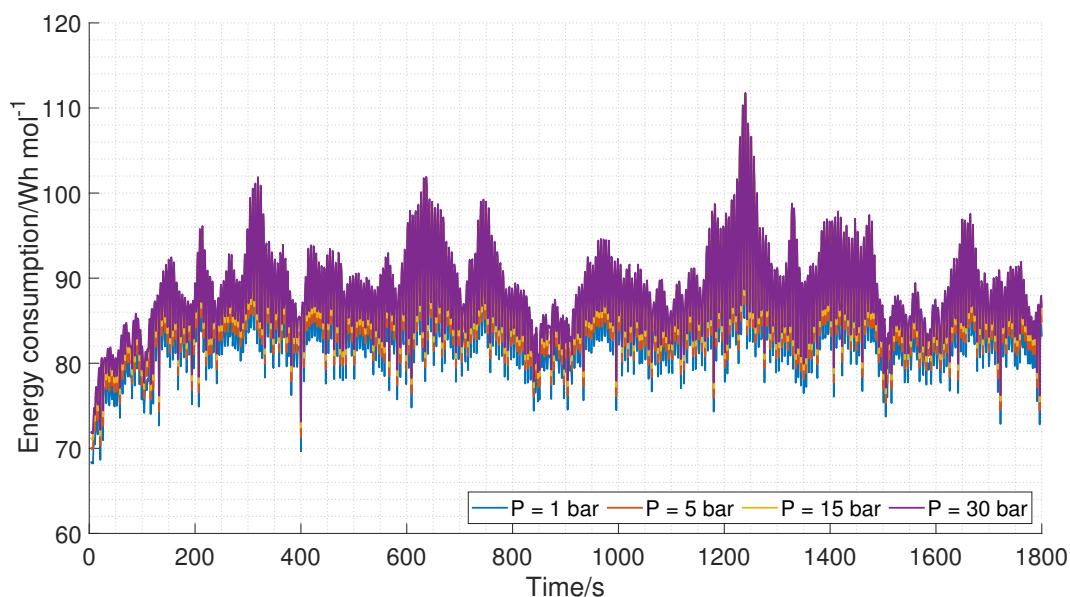


Figure 4.25. Energy consumption trends with respect to pressure - P_{inst}^{wave}

has on the energy consumption, such that an increase of energy consumption is strictly dependent on huge power peaks (see Figure 3.7). This aspect has already been recorded in the case of instantaneous power produced by the wind turbine (see Subsubsection 4.2.2.1), where, however, the peaks were more contained. This behaviour is common in renewable energy systems and, especially, in wave energy, where power fluctuations (the peak/mean power ratio) is so large. The price to pay for a sudden increase in the hydrogen production is the increase in energy consumptions.

The energy consumption increasing trend is probably influenced by temperature that, as Figure 4.26 reports, remains pretty low for all the simulation time. High temperature translates in higher efficiency, being temperature favourable for reaction kinetics, reason why in the wind turbine input-power case a decrease of energy consumption (see Figure 4.13) has been recorded, aspect that does not apply to

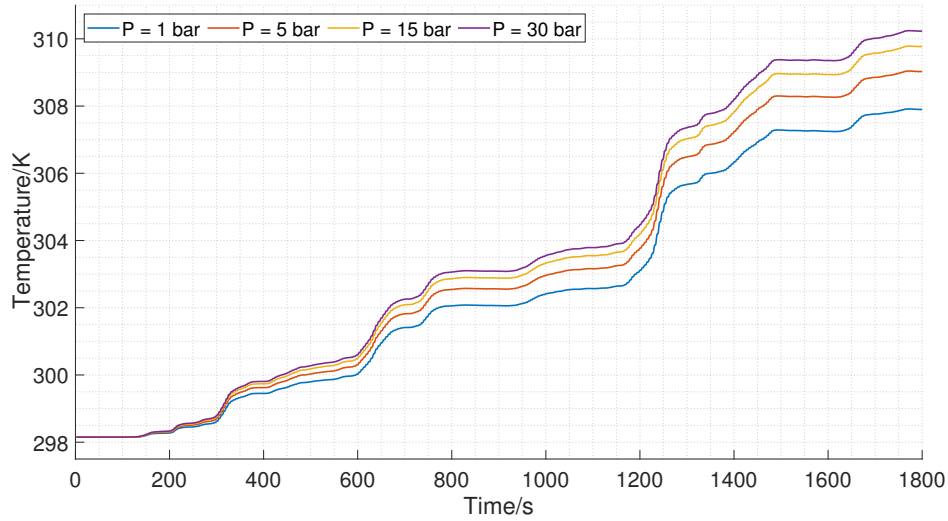


Figure 4.26. Temperature trends with respect to pressure - P_{inst}^{wave}

this case. Every time a power peak appears, an increase of temperature is suddenly recorded (Figure 4.26). Analysing the heat flux, the trend is the one depicted in

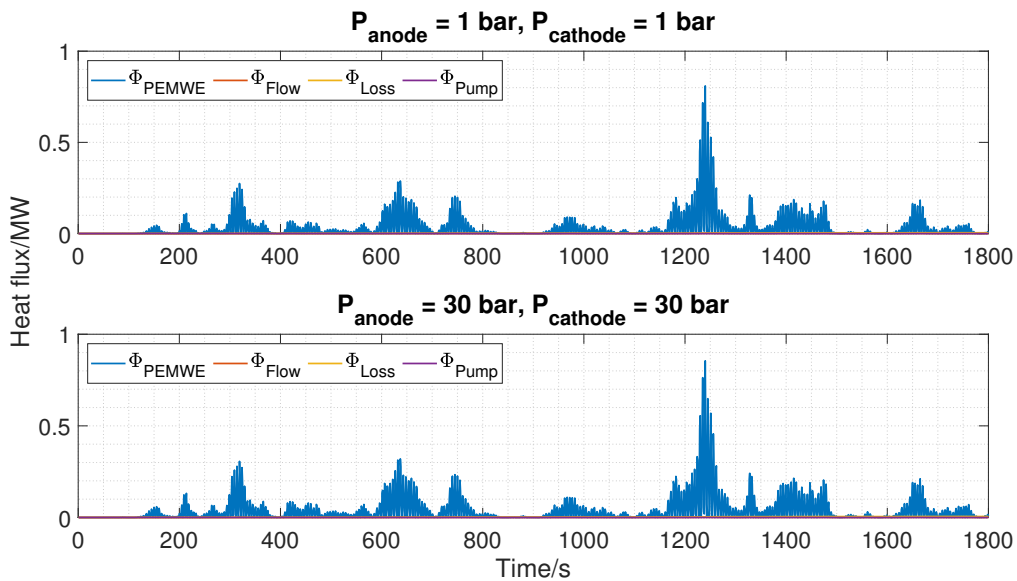


Figure 4.27. Contribute of heat fluxes - P_{inst}^{wave}

Figure 4.27. For the sake of clarity, only the contributes of each term of Equation 4.2 have been represented, for the most extreme cases, i.e. anode and cathode pressure equal to, firstly 1 bar, and then 30 bar.

Even if the differences are not so evident, an increase of heat flux as pressure

increase is appreciable. The heat flux range is really wide, reaching in some cases values close to the MW, and variable. The almost totality comes from the contribution of the heat flux produced by irreversibilities inside the stacks, as Figure 4.27 reports.

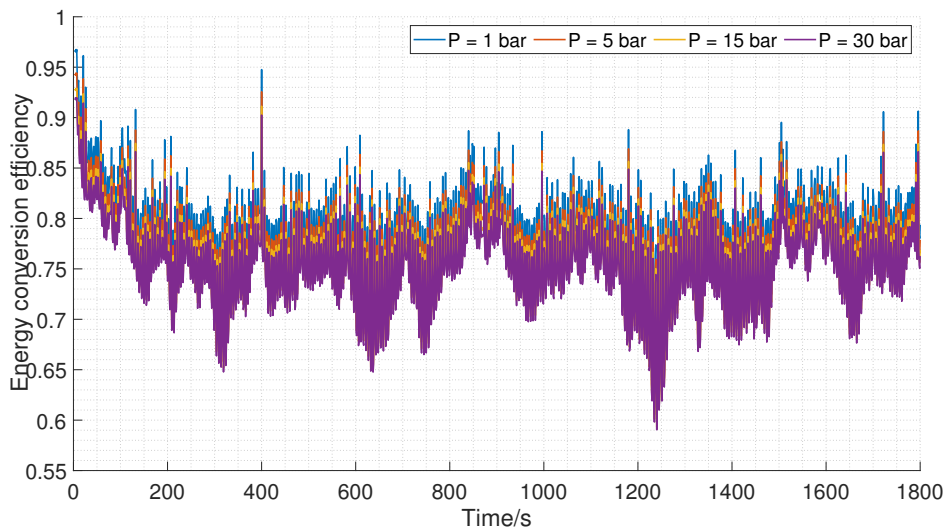


Figure 4.28. Efficiency trends with respect to pressure - P_{inst}^{wave}

Lastly, the efficiency trends are depicted in Figure 4.28. As already seen in Sub-section 4.2.1.1, but also in 4.2.2.1, the efficiency reflects the energy consumption, in particular it has an opposite behaviour: when the energy consumption increases, efficiency decreases and vice versa. For this reason, in subsequent analyses, it will be omitted.

4.2.3.2 Sensitivity analysis - Temperature

Regarding the sensitivity analysis with respect with temperature, the hydrogen production, energy consumption and heat flux changes according to **outdoor temperature** were firstly analysed, increasing it from 298.15 K up to 313.15 K (25 °C - 40 °C) and fixing the anode and cathode pressure to 1 bar, while the PID and refrigerant temperature to 338.15 and 283.15 K (65 °C and 10 °C) respectively. However, in the energy consumption and the heat flux analysis, for sake of clarity it was omitted to report each curve.

Starting from the hydrogen production, the differences between the average power case and the instantaneous here analysed were studied and compared. Similarly to the pressure analyses, the differences are evident with a higher hydrogen generation, in the average input-power case, of around 10%. In conclusion, it is not possible, without introducing an error, evaluate ex post the hydrogen productivity starting

from the average input-power. The growing trend reflects what previously seen

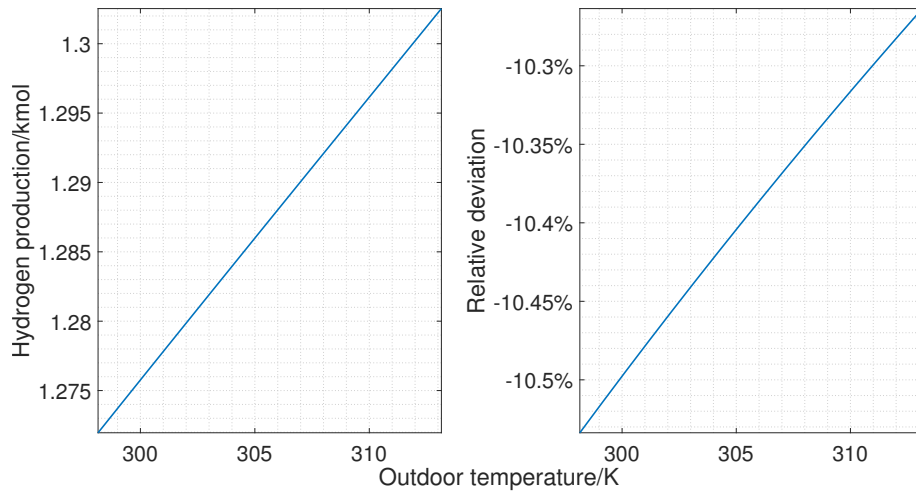


Figure 4.29. Hydrogen production trends with respect to outdoor temperature - P_{inst}^{wave}

regarding the parametric analysis with respect to outdoor temperature in the wind turbine case (see Subsubsection 4.2.1.2). By increasing the outdoor temperature,

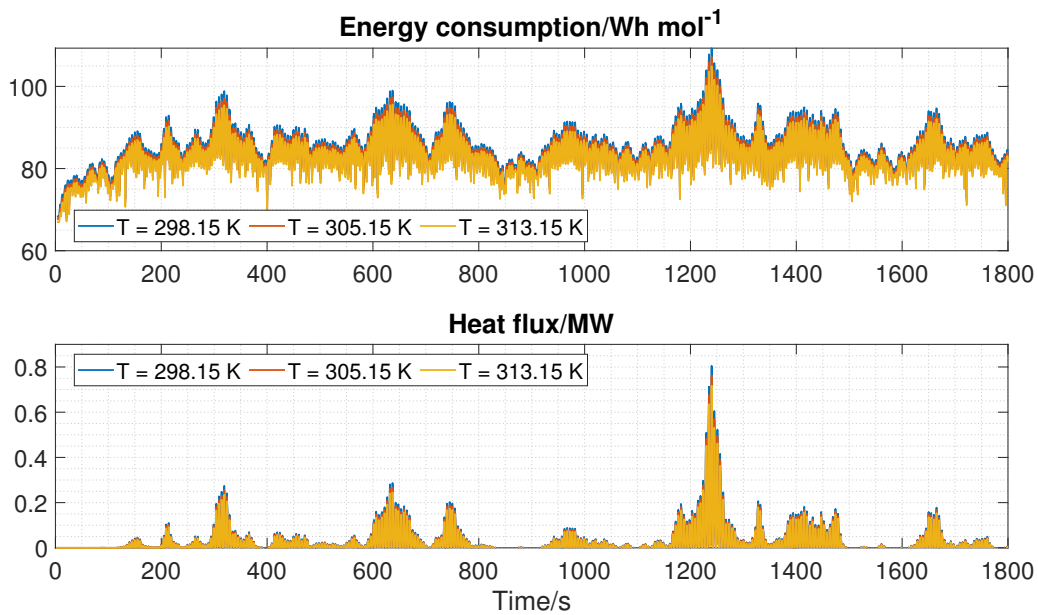


Figure 4.30. Energy consumption & heat flux trends with respect to outdoor temperature - P_{inst}^{wave}

the energy consumption experiences a decrease due to kinetics, fostered by temperature increase of injected water (equal to outdoor temperature). The heat flux

is not so sensible to outdoor temperature, even if it is still possible to notice small differences, i.e. the decrease of the heat flux with increasing outdoor temperature. The inversion of the curves as depicted in Figure 4.7 and 4.19, it is not appreciable due to the low stack temperature (308 K - 322 K range).

In the sensitivity analysis regarding temperature regulated by PID controller (**PID temperature**), the anode and cathode pressure have been set equal to 30 bar with the aim to increase the temperature inside the stacks (so to record a more pronounced response) , while the outdoor and refrigerant temperature to 298.15 K and 283.15 K (25 °C and 10 °C) respectively. PID temperature has been changed in a 298.15 K - 311.15 K range because, as already mentioned before, the temperature remains pretty low in the spar buoy case study. It follows that the reference operating temperature needs to be reduced to record some more pronounced variation. The deviation in the hydrogen generation from the average input-power is in the order of 10%, with a reduction of the production in the instantaneous case, while the growing trend is the result of the temperature rise inside the stacks, which foster reaction kinetics (Figure 4.31).

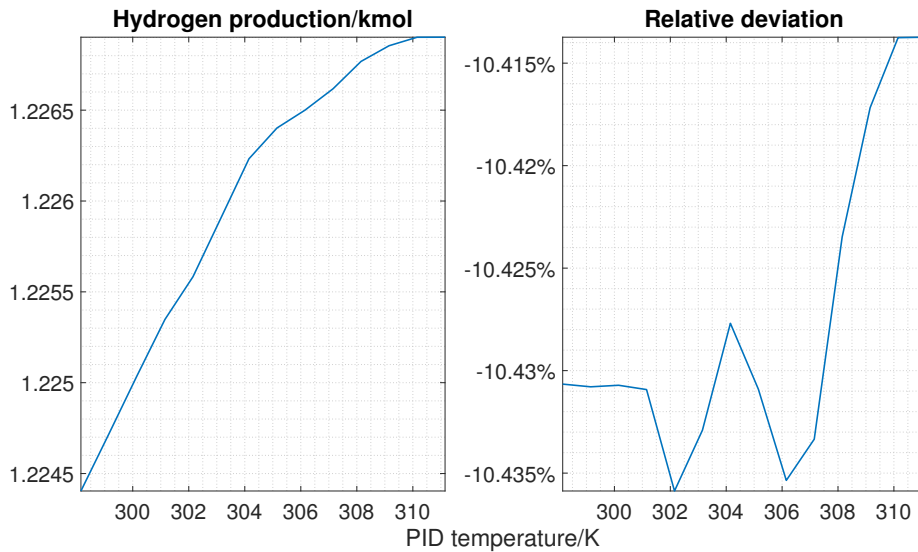


Figure 4.31. Hydrogen production trends with respect to PID temperature - P_{inst}^{wave}

Figure 4.32 reports the energy consumption and the heat flux trends with respect to PID temperature. The differences between the trends are so small to be completely negligible.

Finally, the sensitivity analysis according to the **refrigerant temperature** can be analysed. Anode and cathode were set equal to 30 bar, so as to increase the

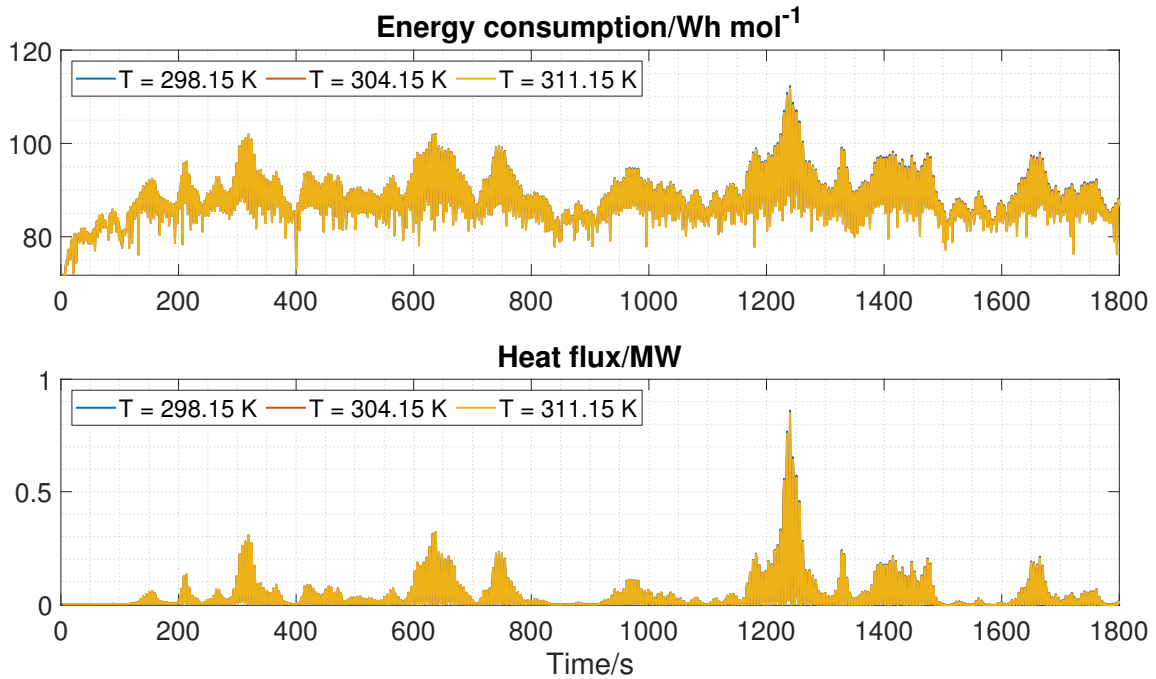


Figure 4.32. Energy consumption & heat flux trends with respect to PID temperature - P_{inst}^{wave}

temperature inside the stacks and emphasize the role of coolant temperature. In this perspective, the outdoor and PID temperatures were set equal to 298.15 K and 308.15 K (25 °C and 35 °C) respectively, while the refrigerant temperature ranges from 278.15 K to 298.15 K. Figure 4.33 reports the hydrogen production trend with respect to refrigerant temperature.

A quantitative deviation was recorded from the instantaneous input-power case with respect to average one, showing a decrease of production of around 10%. Although slightly, hydrogen production increases, while both the energy consumption and the heat flux, decrease with increasing refrigerant temperature. Unfortunately, the last two are not appreciable from Figure 4.34 without zooming.

In conclusion, regarding the spar buoy case study (Figure 3.7), the refrigerant temperature has a completely negligible influence on the system.

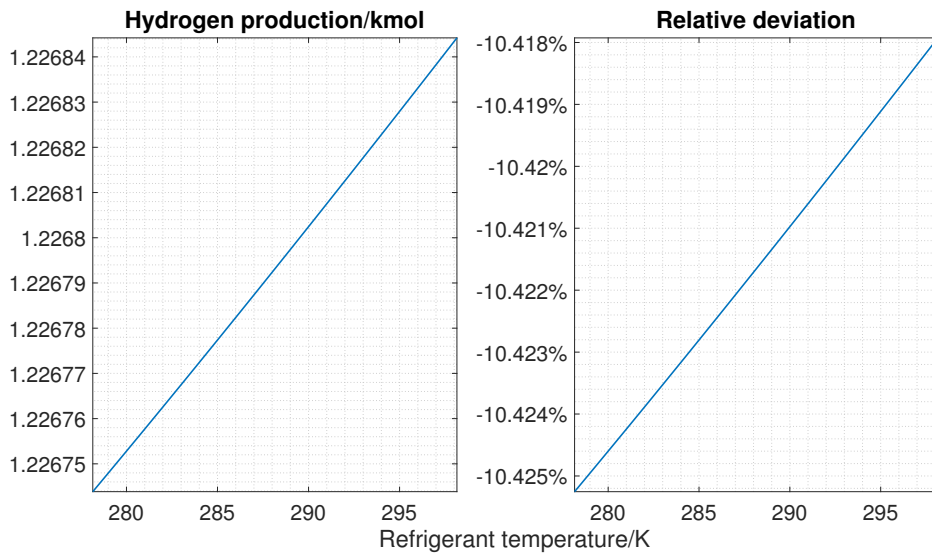


Figure 4.33. Hydrogen production trends with respect to refrigerant temperature - P_{inst}^{wave}

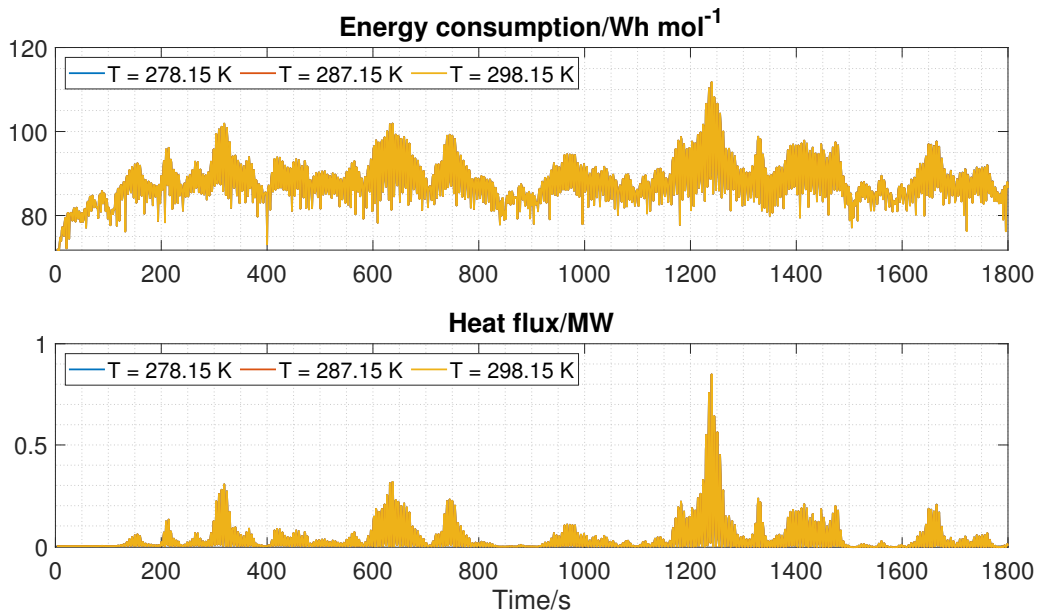


Figure 4.34. Energy consumption & heat flux trends with respect to refrigerant temperature - P_{inst}^{wave}

Chapter 5

Conclusion

The goal of the present Thesis was to investigate the scientific literature regarding PEM electrolyzers and create a one-dimensional (1D) model, quick to run but sufficiently reliable, able to simulate the production of hydrogen, heat generation and energy consumption, under dynamic load conditions, and sufficiently malleable for future studies. The scientific literature is rich in examples and researches related to the modeling of PEM fuel cells, but still meager as regards thorough electrolyser models, which include all the submodels characterising the system, that are the electrochemical, thermal and mass transport ones. The model here reported, implemented in the Simulink[®] environment, showed excellent agreement with experimental data, where voltage and temperature calculations in the time-domain proved to be adherent to reality, as well as the polarization curve. Thanks to the excellent results, a study on green hydrogen production from dynamic sources, such as wind and wave, was conducted. Several parametric analyses were carried out applying different temperature and pressure conditions, thus managing to highlight the weight that these parameters have on hydrogen generation, heat and energy consumption.

More specifically, the qualitative dependence on parameters is summarized in the following table.

		H ₂ production	Energy consumption	Heat flux	Efficiency
P	↗	↘↘↘	↗↗↗	↗↗	↘↘↘
T _{outdoor}	↗	↗↗	↘↘	↗	↗↗
T _{PID}	↗	↗↗↗	↘↘↘	↘↘↘	↗↗↗
T _{refrigerant}	↗	↗	↘	↘↘	↗

Table 5.1. Qualitative summary of the results from the sensitivity analyses

Pressure and temperature regulated by the PID controller are clearly the most

influencing variables, therefore having the highest impact on the hydrogen production, besides energy consumption and heat flux generation. If the aim is to optimize the electrolyser operation, a research on the trade-off between the increase of pressure and temperature must be carried out, therefore trying to minimize the costs and maximize the production of hydrogen.

Focusing on the quantitative aspects, hydrogen generation by floating offshore wind turbine resulted to be higher compared to spar buoy case. In fact, being the power production from wind subjected to less oscillations, it is possible to scale the electrolyser more easily, avoiding the oversizing, and generate more hydrogen. Instead, if the system is matched with the spar buoy, having a much more variable power load, it must be oversized. The great variability of the last power system is evident looking also at the deviation in the production of hydrogen between the simulated real operation case (Figure 3.7) and the fictitious one having as input power the average. For this reason, the electrolysers connected to a spar buoy would be more interesting from the point of view of hydrogen generation from surplus power production, thus helping to address the problem of intermittent energy generation by making wave energy converters more flexible and providing strength to electricity networks.

Another interesting aspect that emerged during the analysis is related to the heat exchanger. In fact, in the scientific articles, mentioned also in this document, the temperature control system is rarely sufficiently detailed, moving often really quick on the implementation of the heat exchanger and the PID controller. What emerged from the simulations is that the employment of water as a coolant has often been insufficient to manage the heat flow and to maintain the temperature at the level imposed by the PID controller. In fact, the limit imposed by the refrigerant temperature is too binding and does not allow the heat exchanger to be fast enough to regulate the peak heat flux generated by dynamic power signals.

Further implementation could be developed, starting from increasing the dimension from 1D to 2D, up to 3D. Gas diffusion through the membrane, gas solubility in liquid water, water transport due to pressure gradients and temperature gradients along the electrolyser are all phenomena that could be implemented in the model to evaluate, in a more precise way, the variables of interest. However, the designed model has already proven its effectiveness in numerous reported simulations and could play an key role in future studies. In fact, thanks to its versatility and speed of execution, it could be employed in future researches by those who, like me, work on solutions to tackle climate change.

Appendix A

Simulink[®] figures

A.1 Simulink® model

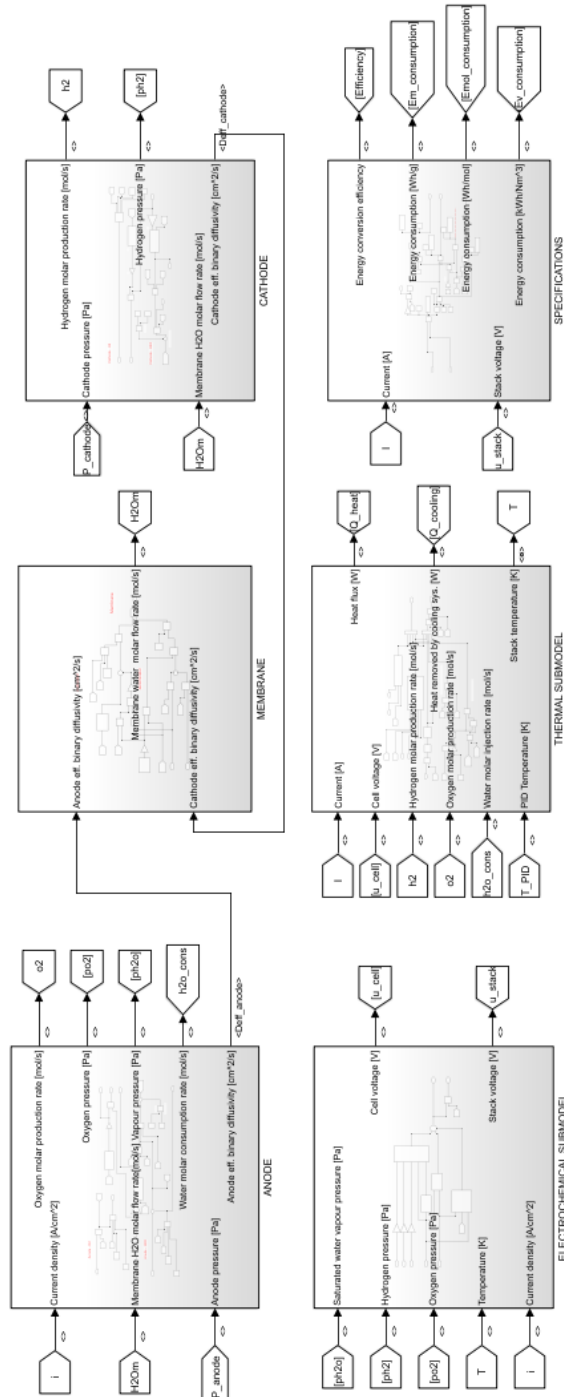


Figure A.1. Simulink® model

A.2 Simulink® electrochemical submodel

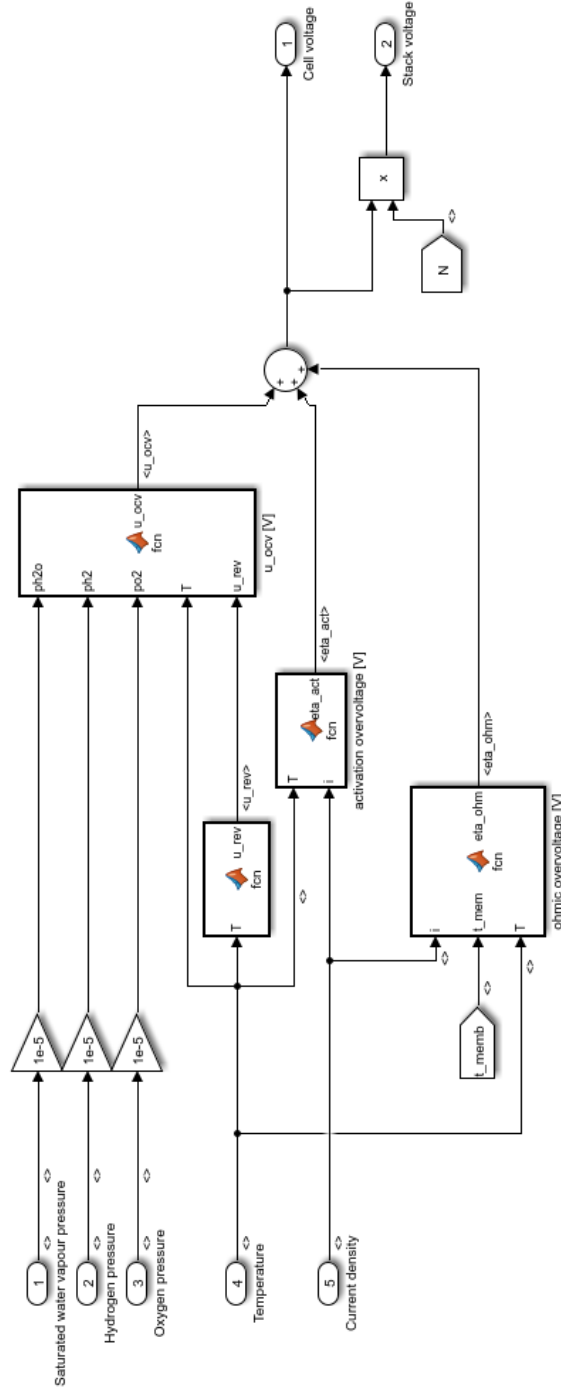


Figure A.2. Simulink® electrochemical submodel

A.3 Simulink® anode submodel

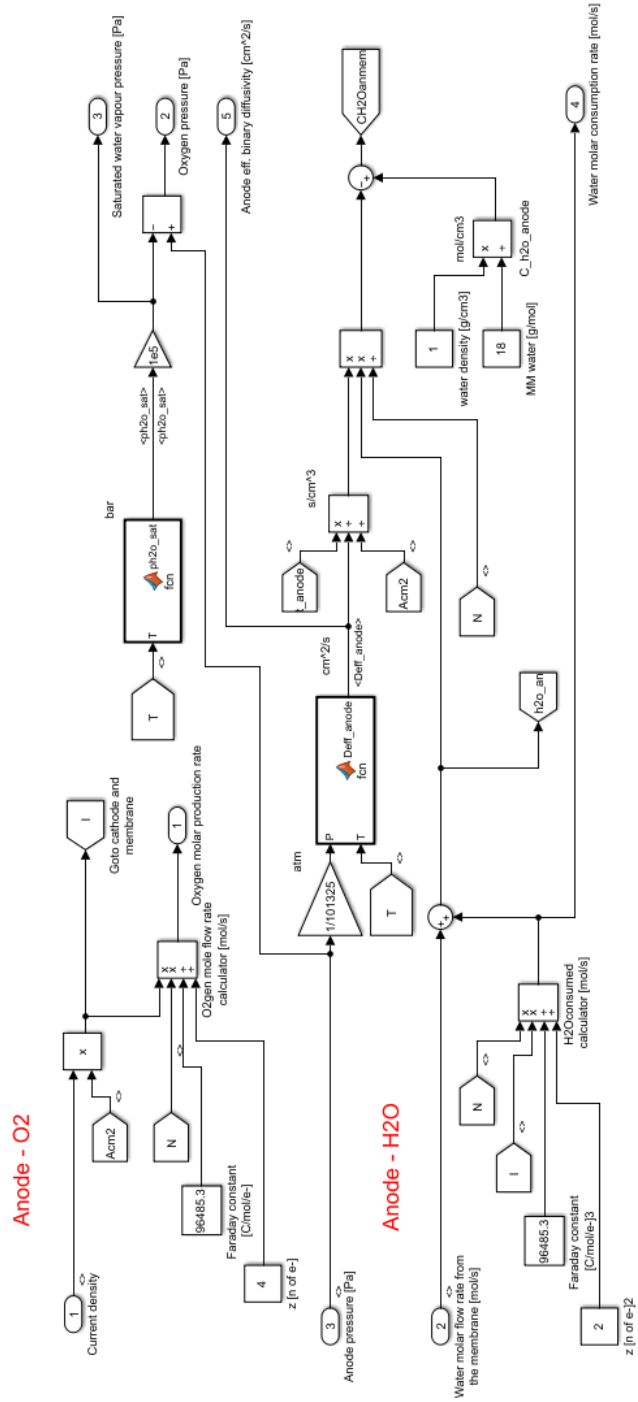


Figure A.3. Simulink® anode submodel

A.4 Simulink® cathode submodel

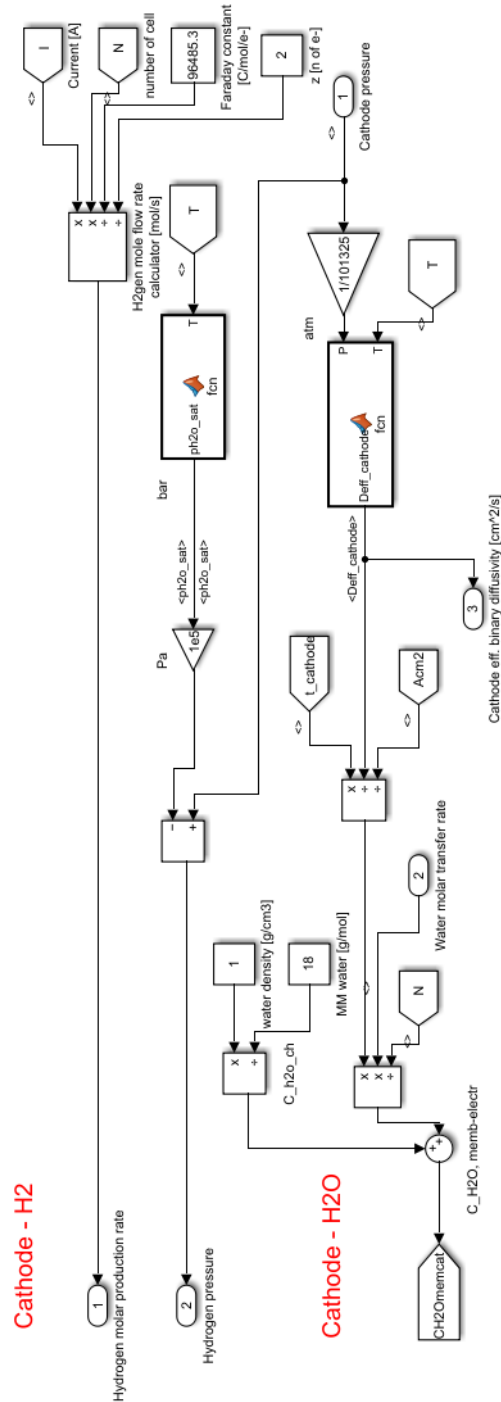


Figure A.4. Simulink® cathode submodel

A.5 Simulink® membrane submodel

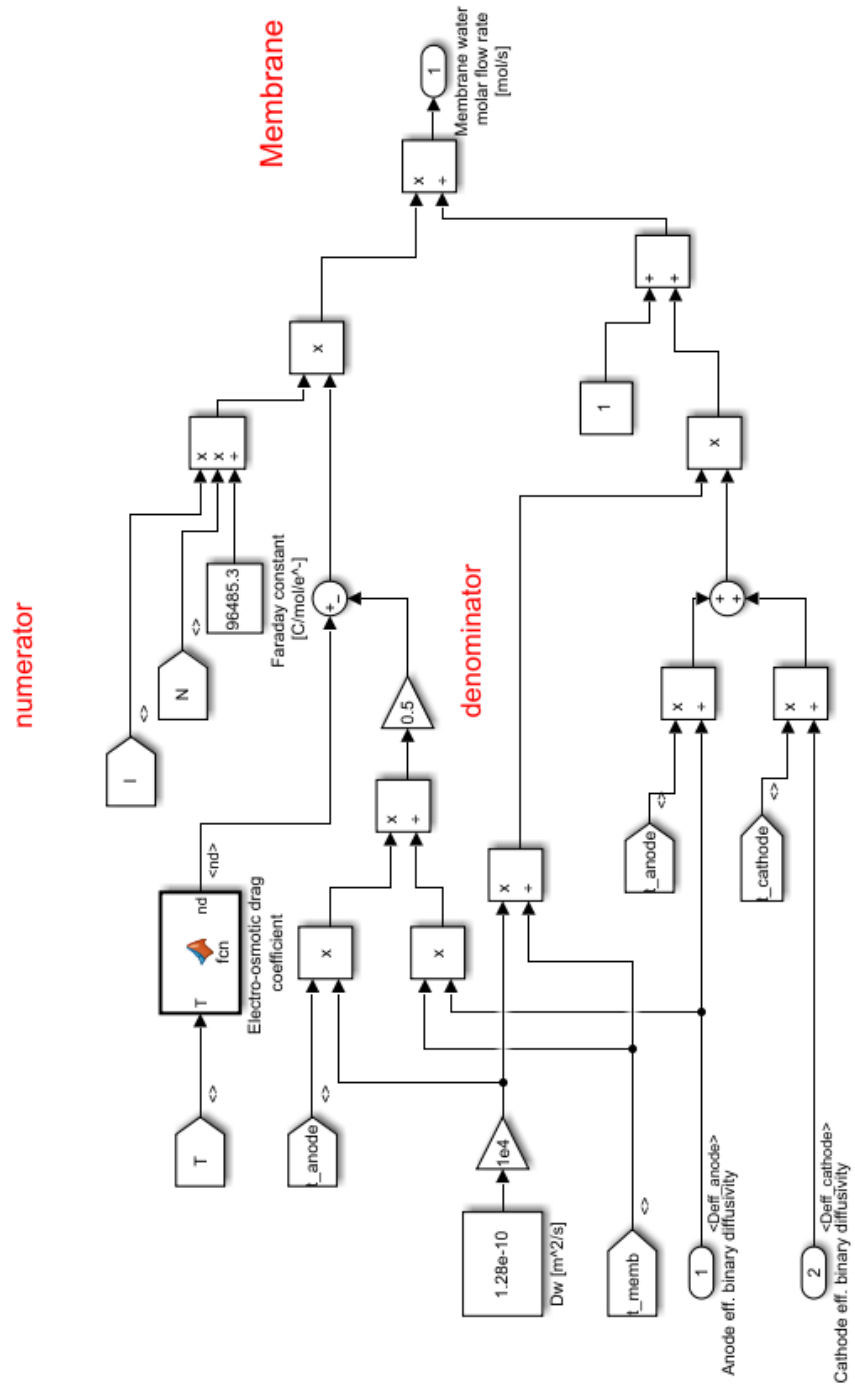


Figure A.5. Simulink® membrane submodel

A.6 Simulink[®] heat exchanger submodel

A Matlab[®] function corrects the mass flow rate, by imposing it to zero, when the output signal from the PID controller is negative.

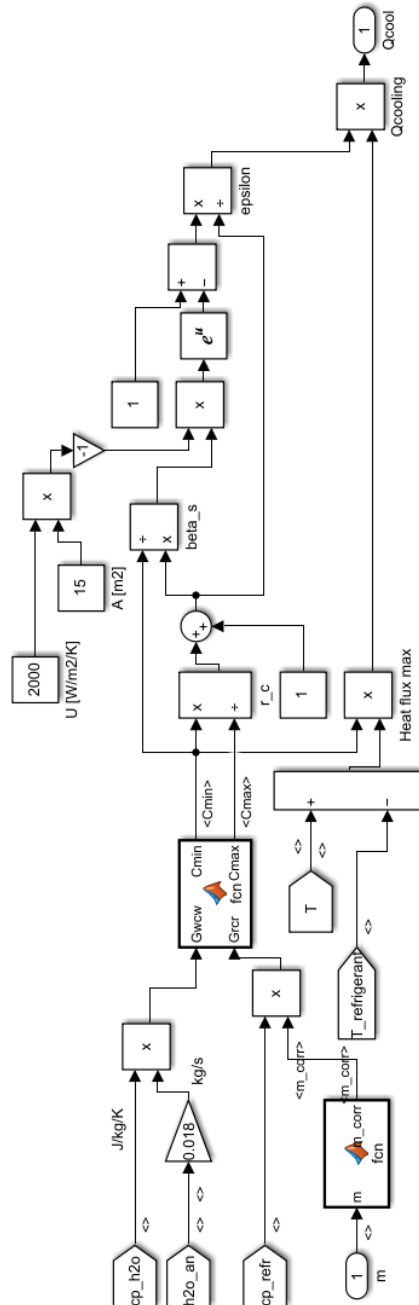


Figure A.6. Simulink[®] heat exchanger submodel

A.7 Simulink® thermal submodel

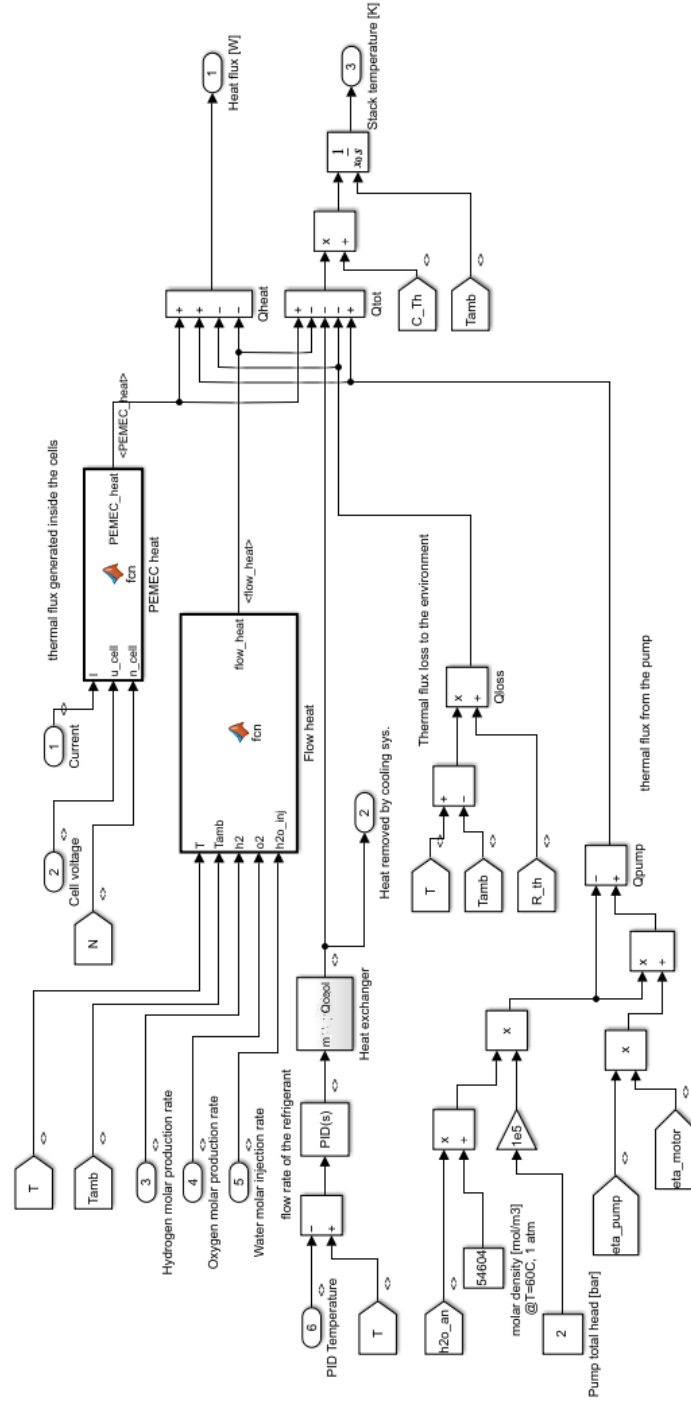


Figure A.7. Simulink® thermal submodel

Bibliography

- [1] [World Energy Outlook 2021](#) by International Energy Agency website accessed the 04/10/2022.
- [2] [IPCC Sixth Assessment Report](#) website accessed the 05/10/2022.
- [3] [United Nations Economic Commission for Europe](#) website accessed the 04/10/2022.
- [4] ["Our World In Data: Energy"](#) website accessed the 05/10/2022.
- [5] Chowdhury, A., Corendea, C. (2022, July 22) Russia-Ukraine war could derail a renewable energy future. Hindustan Times.
- [6] Steffen, B., Patt, A. (2022). A historical turning point? Early evidence on how the Russia-Ukraine war changes public support for clean energy policies. *Energy Research & Social Science*, 91, 102758.
- [7] European Commission. Communication from the Commission to the European Parliament, the Council, the European Economic and Social Committee and the Committee of the regions. A hydrogen strategy for a climate-neutral Europe. Brussels, 8.7.2020.
- [8] European Commission. Communication from the Commission to the European Parliament, the Council, the European Economic and Social Committee and the Committee of the regions: The European Green Deal. Brussels, 11.12.2019.
- [9] Ömer Faruk Selamet, Fatih Becerikli, Mahmut D. Mat, Yüksel Kaplan, Development and testing of a highly efficient proton exchange membrane (PEM) electrolyser stack, *International Journal of Hydrogen Energy*, Volume 36, Issue 17, 2011, Pages 11480-11487, ISSN 0360-3199, <https://doi.org/10.1016/j.ijhydene.2011.01.129>.
- [10] [Siemens Press](#) website accessed the 12/11/2022.
- [11] [Air Liquide](#) website accessed the 26/10/2022.
- [12] Grigoriev SA et al., Current status, research trends, and challenges in water electrolysis science and technology, *International Journal of Hydrogen Energy*, <https://doi.org/10.1016/j.ijhydene.2020.03.109>
- [13] D. Bessarabov, P. Millet, B.G. Pollet (Ed.), *PEM Water Electrolysis*, Elsevier, 2018.

- [14] Olivier, Pierre; Bourasseau, Cyril; Bouamama, Pr. Belkacem (2017). Low-temperature electrolysis system modelling: A review. *Renewable and Sustainable Energy Reviews*, 78(), 280–300
- [15] C.Y. Biaku, N.V. Dale, M.D. Mann, H. Salehfar, a. J. Peters, T. Han, A semiempirical study of the temperature dependence of the anode charge transfer coefficient of a 6 kW PEM electrolyser, *Int. J. Hydrogen Energy* 33 (16) (2008) 4247e4254.
- [16] N.V. Dale, M.D. Mann, H. Salehfar, Semiempirical model based on thermodynamic principles for determining 6 kW proton exchange membrane electrolyser stack characteristics, *J. Power Sources* 185 (2008) 1348e1353
- [17] Buck, A.L., 1981. New equations for computing vapor pressure and enhancement factor. *J. Appl. Met.* 20, 1527–1532.
- [18] Espinoza-Lopez M, Darras C, Poggi P, Glises R, Baucour P, Rakotondrainibe A, Besse S, Serre-Combe P. Modelling and experimental validation of a 46 kW PEM high pressure water electrolyzer. *Renew Energy* 2018;119:160e73.
- [19] Li X. Principles of fuel cells. Taylor & Francis Group; 2006
- [20] R. García-Valverde, N. Espinosa, a. Urbina, Simple PEM water electrolyser model and experimental validation, *Int. J. Hydrogen Energy* 37 (2012) 1927e1938.
- [21] I.N.C. Giner, PEM Electrolyzer Incorporating an Advanced Low Cost Membrane, 2013.
- [22] Z. Abdin, C.J. Webb, E.M. Gray, Modelling and simulation of a proton exchange membrane (PEM) electrolyser cell, *Int. J. Hydrogen Energy* 40 (39) (2015) 13243e13257.
- [23] Marangio F, Santarelli M, Calì M. Theoretical model and experimental analysis of a high pressure PEM water electrolyser for hydrogen production. *Int J Hydrogen Energy* 2009;34:1143e58.
- [24] Qiang Y, Hossein T, Junxiao W, Investigation of water transport through membrane in a PEM fuel cell by water balance experiments. *Journal of Power Sources* 158 (2006) 316–325.
- [25] Bird RB, Stewart WE, Lightfoot EN. *Transport phenomena*. 2nd ed. John Wiley & Sons Inc.; 2002.
- [26] M.M. Tomadakis, S.V. Sotirchos, Ordinary and transition regime diffusion in random fiber structures, *AIChE J.* 39 (1993) 397–412.
- [27] Onda K, Murakami T, Hikosaka T, Kobayashi M, Notu R, Ito K. Performance analysis of polymer-electrolyte water electrolysis cell at a small-unit test cell and performance prediction of large stacked cell. *J Electrochem Soc* 2002;149(8):A1069e78. <https://doi.org/10.1149/1.1492287>.
- [28] Ge S, Yi B, Ming P. Experimental determination of electroosmotic drag coefficient in Nafion membrane for fuel cells. *J Electrochem Soc* 2006;153(8):A1443e50. <https://doi.org/10.1149/1.2203934>.

- [29] Xie G, Okada T. Water transport behavior in Nation 117 membranes. *J Electrochem Soc* 1995;142(9):3057e62. <https://doi.org/10.1149/1.2048686>.
- [30] T. Yigit, O.F. Selamet, Mathematical modeling and dynamic Simulink simulation of high-pressure PEM electrolyzer system, *Int. J. Hydrogen Energy* 41 (32) (2016) 13901e13914.
- [31] Gorgun H. Dynamic modelling of a proton exchange membrane (PEM) electrolyzer. *Int J Hydrogen Energy* Jan. 2006;31(1):29e38.
- [32] J.C. Amphlett, R.M. Baumert, R.F. Mann, B.A. Peppley, P.R. Roberge, Performance modelling of the Ballard Mark IV solid polymer electrolyte fuel cell, *J. Electrochem. Soc.* 142 (1995) 1–15.
- [33] Nam JH, Kaviany M. Effective diffusivity and watersaturation distribution in single- and two-layer PEMFC diffusion medium. *International Journal of Heat and Mass Transfer* 2003;46:4595–611.
- [34] Springer TE, Zawodzinski TA, Gottsfeld S. Polymer electrolyte fuel cell model. *Journal of Electrochemical Society* 1991;138:2334–41.
- [35] [NIST Chemistry WebBook](#) accessed the 15/06/2022.
Hydrogen: <https://webbook.nist.gov/cgi/cbook.cgi?ID=C1333740&Mask=4>.
Oxygen: <https://webbook.nist.gov/cgi/cbook.cgi?ID=C7782447&Mask=4>.
Water: <https://webbook.nist.gov/cgi/inchi?ID=C7732185&Mask=4>.
- [36] Manwell, James F., Jon G. McGowan, and Anthony L. Rogers. *Wind energy explained: theory, design and application*. John Wiley & Sons, 2010.
- [37] Ki-Yong Oh, Woochul Nam, Moo Sung Ryu, Ji-Young Kim, Bogdan I. Epureanu, A review of foundations of offshore wind energy converters: Current status and future perspectives, *Renewable and Sustainable Energy Reviews*, Volume 88, 2018, Pages 16-36, ISSN 1364-0321, <https://doi.org/10.1016/j.rser.2018.02.005>.
- [38] Jiang, Zhiyu. (2021). Installation of offshore wind turbines: A technical review. *Renewable and Sustainable Energy Reviews*. 139. 110576. [10.1016/j.rser.2020.110576](https://doi.org/10.1016/j.rser.2020.110576).
- [39] [HyWind - Saipem](#) website accessed the 03/11/2022.
- [40] Amir Garanovic, "IDOM's wave energy device takes VALID project spotlight", *OFFSHORE ENERGY*, January 6, 2022
- [41] António F.O. Falcão, João C.C. Henriques, José J. Cândido, Dynamics and optimization of the OWC spar buoy wave energy converter, *Renewable Energy*, Volume 48, 2012, Pages 369-381, ISSN 0960-1481, <https://doi.org/10.1016/j.renene.2012.05.009>.
- [42] [OceanSET](#) website accessed the 13/11/2022.
- [43] P. Dieguez, A. Ursua, P. Sanchis, C. Sopena, E. Guelbenzu, L. Gandia, Thermal performance of a commercial alkaline water electrolyzer: experimental study and mathematical modeling, *Int. J. Hydrogen Energy* 33 (24) (2008) 7338e7354.

- [44] Introduction to Heat Transfer 6th edition by Bergman, Theodore L., Lavine, Adrienne S., Incropera, Frank
- [45] [2 GEP Skid by ITM POWER](#) website accessed the 11/10/2022.
- [46] [H-TEC SYSTEMS Hydrogen Cube System \(HCS\)](#) website accessed the 11/10/2022.
- [47] [Cost forecast for low temperature electrolysis – technology driven bottom-up prognosis for PEM and Alkaline water electrolysis systems](#) by Fraunhofer Institute for Solar Energy Systems.
- [48] [HyLYZER® - 1000/500 datasheet](#) accessed the 11/10/2022.
- [49] [Plug EX-2125D datasheet](#) accessed the 11/10/2022.
- [50] [EL600N electrolyser by H2B2](#) website accessed the 11/10/2022.
- [51] ["MW-Scale PEM-Based Electrolyzers for RES Applications"](#), DOE Hydrogen and Fuel Cells Program.
Poster Session - April 30, 2019.
Authors: Monjid Hamdan (Giner ELX (PI)), Kevin Harrison (NREL).